UNIVERSIDAD AUTONÓMA DE MADRID
Facultad de Ciencias
Departamento de Física Teórica

Measurement of D mesons Production in Deep Inelastic Scattering at HERA

Submitted in partial fullfilment of the requirements
for the degree "Doctor en Ciencias Físicas" by

Manuel Zambrana Ramírez
Supervisor : Luis Labarga Echeverría

01/09/2007

This work has been carried out in the frame of the ZEUS Collaboration through the High Energy Physics Group of the Universidad Autónoma de Madrid.

The author was financially supported by the “Ministerio de Educación y Ciencia”.

UNIVERSIDAD AUTONÓMA DE MADRID
Facultad de Ciencias
Departamento de Física Teórica

Medida de Producción de Mesones D en Dispersión Profundamente Inelástica en HERA

Memoria presentada para la la obtención
del título de "Doctor en Ciencias Físicas" por

Manuel Zambrana Ramírez
Supervisor : Luis Labarga Echeverría

01/09/2007

Este trabajo ha sido desarrollado en la Colaboración ZEUS a través del grupo de Altas Energías de la Universidad Autónoma de Madrid.

El autor ha sido financiado por el “Ministerio de Educación y Ciencia”.

Este trabajo está dedicado a mi familia

Preface

Heavy-quark production in ep interactions in the deep inelastic scattering (DIS) regime is dominated by the interaction between the exchanged virtual photon and a gluon within the proton, the so-called Boson Gluon Fusion (BGF) mechanism. Heavy-quark production provides a twofold test of quantum chromodynamics (QCD): a thorough study of the Born process and higher-order corrections to the BGF reaction, and an independent check of the gluon density in the proton extracted from the inclusive DIS data. Of the two heavy quarks whose production is accessible by HERA, c and b, the latter is strongly suppressed due to its smaller electric charge and larger mass. This analysis reports a study of c-quark production.

A charm quark in the final state is identified by the presence of a corresponding charmed hadron. This analysis studies the production of the pseudo-scalar mesons D^0, D^+, D_s^+ and the vector meson D^{*+} from the decays $D^0 \to K^-\pi^+$, $D^+ \to K^-\pi^+\pi^+$, $D_s^+ \to \phi\pi^+ \to K^+K^-\pi^+$ and $D^{*+} \to D^0\pi^+ \to K^-\pi^+\pi^+$ (the charge conjugated modes are implied throughout this document). Since a D hadron is measured and not the c quark itself, any comparison with perturbative QCD (pQCD) requires a modelling of the $c \to D$ fragmentation. A consequence of the QCD factorisation theorem [1] is that the "hard" (pQCD governed) c-production mechanism is independent of the "soft" fragmentation process. Measurements of D-hadron cross sections provide therefore information abou t both c-quark production and its fragmentation.

This analysis presents a complete study of D-meson production in DIS at HERA: measurements of c-quark fragmentation ratios and fractions with unprecedent precision, D-meson differential cross sections and the charm contribution, $F_2^{c\bar{c}}$, to the proton structure function F_2. It addresses the universality of fragmentation and tests the predictions of pQCD for charm production. The data sample used was taken by the ZEUS detector during the years 1998 – 2000. The fragmentation measurements follow closely those reported recently by ZEUS in the photoproduction regime [2]. Using a variety of D mesons, the pQCD analysis complements the study done with D^{*+} in the same data sample [3]. Measurements of D^* cross sections are only used in this analysis for the extraction of the fragmentation parameters.

Similar measurements of the properties of c-quark fragmentation in DIS have also been performed by the H1 collaboration [4]. Other previous measurements of charm production in DIS with pQCD analyses used the D^{*+} meson [3, 5–9] or inclusive lifetime tags [10]. There are also several measurements of charm photoproduction [9, 11–15].

The results of this analysis have been published by the ZEUS Collaboration [16]. Furthermore, they have been presented by the author in the ICHEP06 conference [17]. They have also been presented in the EPS07 conference [18].

Prefacio

La producción de quarks pesados en régimen de dispersión profundamente inelástica (DIS) está dominada por la interacción entre el fotón virtual itercambiado y el gluón en el protón, el denominado mecanismo de fusión bosón-gluón (BFG). La producción de quarks pesados proporciona un doble test de cromodinámica cuántica: un estudio detallado del proceso Born y correciones de orden mas alto a la reacción BGF, y una comprobación independiente de la densidad gluónica en el protón extraida de datos inclusivos en DIS. De los dos quarks pesados cuya producción es accesible en HERA, c and b, el último está fuertemente suprimido debido a su menor carga eléctrica y a su mayor masa. Este análisis presenta un estudio de la producción de quark c.

Un quark charm en el estado final se identifica por la presencia de un hadron correspondiente. Este análisis estudia la producción de los mesones psudo-escalares D^0, D^+, D_s^+ y del mesón vectorial D^{*+} reconstruidos en los canales desintegración $D^0 \to K^-\pi^+$, $D^+ \to K^-\pi^+\pi^+$, $D_s^+ \to \phi\pi^+ \to K^+K^-\pi^+$ y $D^{*+} \to D^0\pi^+ \to K^-\pi^+\pi^+$ (los modos de carga conjugadas se suponen implícitos a lo largo de todo este documento). Puesto que lo que se mide es un hadrón D y no el propio quark c, cualquier comparación con QCD perturbativa (pQCD) requiere modelar la fragmentación $c \to D$. Una consecuencia del teorema de factorización en QCD [1] es que el mecanismo "duro" de producción de quark c (gobernado por pQCD) es independiente del proceso "blando" de fragmentación.

Este análisis presenta un estudio completo de la producción de mesones D en DIS en HERA: medidas de razones y fracciones de fragmentación de quark c con precisión sin precedente, secciones eficaces diferenciales de producción de mesones D y la contribucion charm, $F_2^{c\bar{c}}$, a la función de estructura del protón F_2. Considera la universalidad de la fragmentación y comprueba las predicciones de pQCD para producción de charm. La muestra de datos usada fue tomada con el detector ZEUS durante los años 1998 – 2000. Las medidas de fragmentación siguen de cerca las presentadas recientemente por ZEUS en régimen de fotoproducción [2]. Usando una variedad de mesones D, el análisis de pQCD complementa el estudio hecho con D^{*+} en la misma muestra de datos [3]. Las medidas de secciones eficaces de producción de D^{*+} se usan solo en este análisis para la extracción de los parámetros de fragmentación.

Medidas similares de las propiedades de fragmentación del quark c han sido igualmente realizadas por la colaboración H1 [4]. Otras medidas previas de producción de charm en DIS con análisis de pQCD usan el mesón D^{*+} [3, 5–9] o identificación inclusiva basada en tiempos de desintegración [10]. Hay también varias medidas de

charm en régimen de fotoproducción [9, 11–15].

Los resultados de este análisis han sido publidados por la Colaboración ZEUS [16]. Además, han sido presentados por el autor en la conferencia ICHEP06 [17]. También han sido presentados en la conferencia EPS07 [18].

Contents

List of Figures

List of Tables

Chapter 1

Theoretical Introduction

In this chapter we give a brief introduction to QCD, $e^{\pm}p$ interactions and Heavy Flavour production, revising the main concepts that will play a significant role in our measurement.

1.1 Quantum Chromodynamics

Quantum Chromodynamics(QCD) is a quantum field theory based on the colour group $SU(3)_c$, as a global symmetry. Imposing local symmetry over the free quark lagrangian, a non-abelian interacting theory of quarks and gluons emerges. The lagrangian of the theory is

$$\mathcal{L} = -\frac{1}{4} F^A_{\alpha\beta} F^{\alpha\beta}_A + \sum_{flavours} \bar{q}_a \left[\gamma^\mu D_\mu - m\right]_{ab} q_b \ ,$$

where $F^A_{\alpha\beta}$ is the field strength tensor defined in terms of the gluon field A^A_α by

$$F^A_{\alpha\beta} = \partial_\alpha A^A_\beta - \partial_\beta A^A_\alpha - g f^{ABC} A^B_\alpha A^C_\beta \ ,$$

where indexes A, B, C run over the eight colour degrees of freedom of the gluon field. The term $-g f^{ABC} A^B_\alpha A^C_\beta$ gives rise to the gluon self-interactions; g is the coupling that determines the strength of the interaction, and f^{ABC} are the structure constants of the $SU(3)$ group.

The sum in the lagrangian runs over the different flavours of quarks. The quark fields q_a $(a = 1, 2, 3)$ are a basis of the triplet representation of $SU(3)$. The covariant derivative D_μ is

$$(D_\mu)_{ab} = \delta_{ab}\partial_\alpha + ig \left(t^c A^c_\alpha\right)_{ab} \ ,$$

where δ_{ab} is the Kronecker's delta and $\{t\}$ are matrices in the fundamental representation of $SU(3)$. By convention, the nomalisation of the $SU(N)$ matrices is chosen

to be

$$Tr\left(t^A t^B\right) = \frac{1}{2}\delta^{AB} \ .$$

With this choice, the colour matrices obey the following relations

$$\sum_A t^A_{ab} t^A_{ba} = C_F \delta_{ab} \ , \qquad C_F = \frac{N^2-1}{2N} \ ,$$
$$Tr\left(T^C T^D\right) = \sum_{A,B} f^{ABC} f^{ABD} = C_A \delta_{CD} \ , \qquad C_A = N \ ,$$

where T are matrices in the adjoint representation of $SU(N)$. In the case of the group $SU(3)$, they are the eight Gell-Mann matrices.

Within this scheme, the theory becomes predictive in the perturbative regime, when the strong coupling constant $\alpha_s = g^2/4\pi$ is small. At leading order, it is given by

$$\alpha_s(\mu^2) = \frac{4\pi}{\beta_0 \ln(\mu^2/\Lambda^2_{QCD})} \ ,$$

where μ defines the energy scale at which α_s is measured, Λ_{QCD} is a QCD cutoff parameter (experimentally determined to be around 200 MeV), and β_0 is defined as

$$\beta_0 = 11 - 2/3 N_f \ .$$

Here, $N_f = 6$ is the number of quark flavours, so β_0 is positive definite. Therefore, the coupling constant α_s is a decreasing function of the energy, so at short distances (i.e., large energy) particles interacting through QCD behaves as quasi-free. This is what we mean by "asymptotic freedom". On the other hand, at large distances (i.e., low energy), the strenght of the interaction becomes large, so that is why partons (quarks and gluons) can not be observed in isolation (color confinement). Instead, a "jet" of particles (hadrons) emerging from the direction of the parton is what we observe experimentally.

In QCD calculations, physical quantities can be expressed in terms of a series in powers of α_s, if $\mu^2 \gg \Lambda^2_{QCD}$. In that case we say that the calculation has a hard scale. The momentum transfer in the interaction provides one hard scale for perturbative calculations, but other scales are also possible, like the mass of heavy quarks or the transverse energy of jets. HERA is a testing ground of QCD. Large center of mass energy allow a test of perturbative QCD predictions. Soft processes (i.e., hadronization), described by phenomenological models, are also tested, as they occur in the same experiment.

1.2 Deep Inelastic Processes

One of the most useful experiments to study the internal structure of hadrons is the scattering of leptons on hadrons. When the momentum transfers are very large, the process is call deep inelastic scattering (DIS). In this case the target looses its identity completely and the resulting final states consist of multiparticle states. The study of those states allows to gain insight into the internal structure of the hadron in the initial state. At HERA, the hadron is a proton, and the lepton is an electron or a positron.

The reaction between the lepton and the proton is mediated by the electromagnetic force via the exchange of a photon, or by the weak force via the exchange of a Z^0 or $W^{\pm}$. If the exchanged boson is a γ or a Z^0, the process is called *neutral current* (NC) DIS. If the exchanged boson is a $W^{\pm}$, the process is called *charged current* (CC) DIS. To distinguish between the two processes, the only information that we need is the type of the final state lepton. If it is the same that the initial one, a neutral current interaction has happened. If not, the electric charge of the incoming lepton has been taken by the exhanged particle and the final state particle can not be the same that the initial one; the electron (positron) has transformed into a neutrino (anti-neutrino) via the exchange of a $W^{\pm}$ boson.

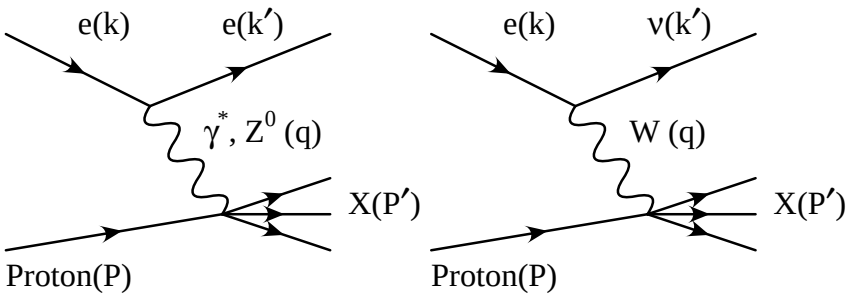

Figure 1.1: Feynman diagrams for DIS; neutral current interaction on the left, and charged current interaction on the right.

These reactions are shown in Figure 1.1 and can be expressed as:

$$e^{\pm}P \to e^{\pm}X \quad (NC)$$
$$e^{+}(e^{-})P \to \bar{\nu}(\nu)X \quad (CC)\ .$$

In general, the proton breaks into a hadronic system, X, which gives rise to the inelastic part of DIS. It is usual to describe the DIS process in terms of Lorentz-invariant variables Q^2, x, y and W. If the incoming and outgoing lepton four-momenta are labelled by k and k', and the four-momentum of the proton by P, then the DIS

variables are defined by

$$\begin{aligned} Q^2 &= -q^2 = -(k - k') > 0 \\ x &= \frac{Q^2}{2P \cdot q} \\ y &= \frac{q \cdot P}{k \cdot P} \\ W^2 &= (P + q)^2 \end{aligned}$$

where Q^2 is the invariant mass, or virtuality, of the exchanged boson, x is the scaling variable introduced by Bjorken [19]. In the quark parton model it is interpreted as the fraction of the proton momentum carried by the struck quark. The variable y corresponds to the fractional energy transfer from the lepton to the proton, in the proton rest frame. Finally, W is the center of mass energy of the system proton-γ. Neglecting the masses of the particles, the squared invariant mass (squared center of mass energy) of the initial state is given by

$$s = (P + k)^2 \approx 2P \cdot k = \frac{Q^2}{xy}$$

Therefore, at a given value of s, the kinematic of a DIS process is fully specified by *two* independent variables from the set Q^2, x, y. Q^2 can take values in the range $0 < Q^2 < s$. Events with $Q^2 \approx 0$ (i.e., exchanged boson quasi-real) define the *photoproduction* (γp) regime. On the other hand, high values of Q^2 define the DIS regime. The transverse distance that can be probed within the proton is inversely proportional to Q^2, so, as Q^2 increases, finer structure can be seen.

1.3 Proton Structure Functions

$e^{\pm}p$ interactions can be viewed as the emission of a photon from the lepton, followed by a photon-proton interaction. This is known by factorisation; the cross section is then represented by convolution [20]

$$\sigma = \sum_i f_i \otimes \sigma_i \ ,$$

where the sum is over all partons, i, within the hadron. The quantity σ_i contains the dynamics of the hard scattering, whereas the f_i are known as the parton distribution functions (PDFs), and contain the unknown non-perturbative physics at the hadronic vertex. The NC and CC cross sections can be described in terms of the "structure functions", F_i, which further parametrise the structure of the proton target as seen by the probing photon. The double differential cross section for $e^{\pm}p$

NC scattering [21] is

$$\frac{d^2\sigma^{ep}}{dxdQ^2} = \frac{4\pi\alpha^2}{xQ^4}\left[\frac{y^2}{2}2xF_1 + (1-y)F_2 \mp (y - \frac{y^2}{2})xF_3\right] \ .$$

Using the relation $F_L = F_2 - 2xF_1$, where F_L is the longitudinal structure function, this reduces to

$$\frac{d^2\sigma^{ep}}{dxdQ^2} = \frac{2\pi\alpha^2}{xQ^4}\left[Y_+F_2 - y^2F_L \mp Y_-xF_3\right] \ ,$$

where

$$Y_\pm = 1 \pm (1-y)^2 \ .$$

The term xF_3 arises from the parity-violating part of Z_0 exchange. It is small for $Q^2 \ll M_Z^2$, so it can be neglected here.

1.4 The Quark Parton Model

In the Quark Parton Model [22, 23], the proton is composed of point-like, non-interacting, spin-1/2 partons. The inelastic scattering of the lepton off the proton is viewed as the elastic scattering of the lepton off a parton within the proton. The $e^\pm p$ cross section is the given by the incoherent sum of the $e^\pm$-parton scattering processes. In the infinite proton momentum frame, the partons have no transverse momentum, and the masses can be neglected. In this limit, the Bjorken scaling variable

$$x = \frac{Q^2}{2P \cdot q}$$

has a simple interpretation as the fraction of the proton momentum carried by the struck quark. Bjorken suggested that at high Q^2 and high ν, where ν is the fraction of the lepton energy carried by the photon in the proton rest frame, the structure functions would be functions of x only, and not of both Q^2 and x (Bjorken scaling [19]). This can be seen in the quark parton model as the partons appearing always point-like, regardless of the scale at which they are probed. The structure functions F_i correspond to the sum of the parton momentum distributions weighted with the square of the electric charge of each parton

$$F_1(x) = \frac{1}{2}\sum_i e_i^2 f_i(x)$$
$$F_2(x) = \sum_i e_i^2 x f_i(x) \ ,$$

where $f_i(x)$ are the pdfs, which can be interpreted as the probability of finding a parton with the momentum fraction x in the proton. The structure functions are

related by the Callan-Gross relation

$$2xF_1(x) = F_2(x)$$

which holds exactly only for spin-1/2 partons which cannot couple to longitudinally polarised photons. The experimental confirmation of this relation allowed the identification of Feynman's partons with Gell-Mann's quarks.

The quark parton model was very successful in explaining many results obtained in DIS experiments but soon some of its problems became apparent. One of them is the prediction that all the parton momentum is carried by quarks. The experimental data proved this prediction to be wrong. In fact, from experimental measurements it was obtained that less than 50% of the proton's momentum is carried by the charged valence quarks:

$$\sum_i \int_0^1 dx\ xf_i(x) \approx 0.5\ .$$

That is, half of the moementum of the proton is carried by neutral particles. In addition, the fact that no free quarks were observed experimentally could not be explained by the qurk parton model. Both these problems were solved by QCD. In the limit $Q^2 \to \infty$, QCD reproduces the quark parton model. In the improved parton model, the proton no longer consists merely on quasi-free quarks, but also a sea of gluons and virtual quark-antiquark pairs.

1.5 QCD evolution equations

The Q^2 dependence of the parton distribution fuctions can be calculated within the pQCD. The main origin of this dependence is that a quark seen at a certain scale Q_0^2 as carrying a certain fractional momentum of the hadron x_0 can be resolved into more quarks and gluons if it is probed at a higher scale Q^2. The resolved quarks and gluons carry a smaller fractional momentum of the hadron ($x < x_0$). Thus, when all QCD effects are included, the structure function F_2 is expected to rise at low x. This is because the low x region is populated by gluons and sea quarks and the quark density is large. The resulting logarithmic dependence of F_2 on Q^2 at fixed x is known as *scaling violation*.

At HERA, the structure function F_2 has been measured in a very wide range of Q^2 and x and the scaling violation at low x has been demonstrated. This is shown in Figure 1.3.

The DGLAP (Dokshitzer-Gribov-Lipatov-Altarelli-Parisi) equations are a set of $(2n_f + 1)$ coupled integro-differentail equations. They can be used to determine the quarks and gluon distributions functions for any value of Q^2 provided they are

known at a particular value of Q_0^2 within the range of applicability of perturbative QCD. These equations are derived by requiring the structure fuctions F_1 and F_2 be independent of the choice of the factorisation scale μ_F, that is:

$$\mu_F^2 \left(\frac{dF_i(x,Q^2)}{d\mu_F^2} \right) = 0 \qquad i = 1,2 \; .$$

In a first step, the DGLAP equations were derived in the *leading logarithm approximation*-LLA. The terms which give the dominant contributions at large x and Q^2 were summed to all orders. All other terms were neglected.

In compact form, the DGLAP equations can be written as:

$$\frac{\partial}{\partial \ln Q^2} \begin{pmatrix} q \\ p \end{pmatrix} = \frac{\alpha_s(Q^2)}{2\pi} \begin{bmatrix} P_{qq} & P_{qg} \\ P_{gq} & P_{gg} \end{bmatrix} \otimes \begin{pmatrix} q \\ p \end{pmatrix} \; ,$$

where $q(x,Q^2)$, $(g(x,Q^2))$ are the quark (gluon) distributions, and $P_{ij}(x)$ are the splitting functions. The latter describe the probability to find a parton of type i with given fractional momentum originating from the parton type j, where i,j can be a quark or a gluon.

Given a specific factorisation and normalisation schemes, the splitting functions are obtained in pQCD as expansion series in α_s:

$$\frac{\alpha_s}{2\pi} P_{ij}(x,Q^2) = \frac{\alpha_s}{2\pi} P_{ij}^{(1)}(x) + (\frac{\alpha_s}{2\pi})^2 P_{ij}^{(2)}(x) + \ldots$$

The truncation after the first two terms in the series defines the next-to-leading order (NLO) DGLAP evolution equations.

The DGLAP equations are valid as long as the impact of the neglected terms is small. At very low x this is not true anymore. In this region another approach is used and the calculations lead to the BFKL (Balitsky-Fadin-Kuraev-Lipatov) equations. DGLAP deals with Q^2 evolution and is inadequate at very low x. BFKL deals with the $\frac{1}{x}$ evolution and it is inadequate at large Q^2.

The inclusive measurement of F_2 at HERA has shown that the evolution of structure functions through the DGLAP equations is in good agreement with the experimental results, as shown in Figure 1.3. In this figure we see the ZEUS NLO QCD global fit [24], which will be used as the parametrisation of the proton PDFs in our theoretical predictions of charm production. Until now, no experimental evidence for the BFKL effects has been observed.

Attemps have been made to achieve a unified description embodying both DGLAP and BFKL-type evolution. Evolution equations which allow an evolution in Q^2 as well as in x are include in the CCFM (Ciafaloni-Catani-Fiorani-Marchesini) evolution equations.

1.6 Heavy Flavour Production

Heavy quark production provides an oportunity to study perturbative QCD, using the mass of the qurk as a hard scale for the calculation. The study of charm quark production in DIS in particular provides insight into the proton structure, as charm contributes up to 30% of the total DIS cross section at medium Q^2. Therefore understanding charm production is essential in order to have a complete understanding of F_2. The lifetime of many charmed mesons are comparatively long since they decay weakly to strange mesons, which means their decay vertex is displaced slightly from the primary vertex, typically by $100 - 300\ \mu m$. Unfortunately the ZEUS detector did not have the capability to resolve such a small distances in the running period 1998-2000. Therefore, in order to understand the charm quark production, it is necessary to study the formation of bound charm states, since they are detector-level observables at HERA. Many hadronic final states have been used to tag charm at HERA, such as semileptonic decays to electrons or muons [25–27], $D^0(1864)$ [8, 28], $D_s^+(1969)$ [11] and $D^{*+}(2010)$ [3, 5–9] mesons, and the J/ψ [29–31], a bound state $c\bar{c}$. Charm fragmentation studies have been done in ZEUS in γp regime, tagging almost the whole charm spectrum, including D^0, D^+, D_s^+, D^{*+} and, for the first time at HERA, the Λ_c^+ [2] baryon. Our analysis considers the same set of final states (except Λ_c^+), but in DIS regime.

1.6.1 Production Mechanisms

Early results fram HERA showed that charm production in NC DIS is dominated by the Boson-Gluon-Fusion (BGF) mechanism [32] : at leading order, pairs $c\bar{c}$ are produced through the coupling of the virtual photon emitted by the electron and a gluon in the proton, as shown in Figure 1.2.

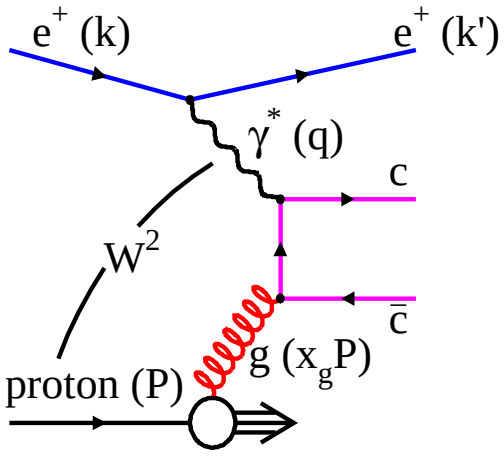

Figure 1.2: Feynman diagram for boson-gluon fusion in $e^{\pm}p$ interactions.

This conclusion was made after comparison of the measured cross sections with the HVQDIS [33] program, which calculates $c\bar{c}$ production exclusively through the BGF mechanism with NLO corrections [34]. The H1 data favour production via the BGF mechanism [8]. ZEUS results [3, 5, 6] also show good agreement with BGF production. With BGF as the dominant production mechanism, the reactions $e^{\pm}p \rightarrow e^{\pm}DX$, with D a charmed hadron, are sensitive to the gluon distribution in the proton.

It is also possible to produce charm in beauty decays during fragmentation, but these contributions are small. The production of beauty is suppresed relative to charm production by both ites greater mass and its weaker coupling to the photon due to its charge.

1.6.2 Charm Evolution

There are two basic ways of trating charm in the evolution equations, based on the factorisation equation : it can be included in the initial state and evolved with the other parton densities (Variable Flavour Number Scheme(VFNS)), or excluded from the initial state and treated separately (Fixed Flavour Number Scheme (FFNS)). These two schemes are in fact different ways to organise the same perturbation series in pQCD. However, as the series is usually terminated after only one or two terms, the two approaches can provide different results depending on the kinematic region involved.

Fixed Flavour Number Scheme (FFNS)

In this scheme the number of active flavours is fixed, independent of Q^2. Only the light quarks u, d, s and the gluon are included in the proton. These active flavours are considered massless, and evolve according to the DGLAP equations. Charm is not considered as an active flavour, so it does not contribute to the evolution of the running coupling constant or the structure functions in the proton. Rather it has zero density in the proton sea, and can only be produce dynamically by the BGF process. HVQDIS treats charm production within this scheme. The presence of two large scales Q^2 and m_c^2, can spoil the convergence of the perturbative series because the neglected terms of orders higher than α_s^2 contain $\log(Q^2/m_c^2)$ factors which can become large. Therefore, the results of HVQDIS are expected to be more accurate at $Q^2 \sim m_c^2$ and become less reliable when $Q^2 \gg m_c^2$.

Variable Flavour Number Scheme (VFNS)

This scheme tends to the FFNS at low Q^2, and trats charm as an active massless flavour in the proton sea above some threshold, thus providing a model that works over the entire range in Q^2. Therefore, at low Q^2, charm is produced dynamically through the BGF process as in the FFNS, whereas, at higher Q^2, heavy-quark parton

densities are introduced. The transition between the two extremes are treated in different ways by different authors [20, 35]. The description relies on the assumption that a probe of virtuality $Q^2 > m_c^2$ can resolve a charm anti-charm pair in the proton sea, and that at sufficiently high Q^2 the charm mass can be neglected.

1.6.3 Charm Structure Function

The charm structure function is a subset of the inclusive structure function of the proton. The double differential cross section can be related to the charm structure function, $F_2^{c\bar{c}}$ by

$$\frac{d^2\sigma^{c\bar{c}}(x,Q^2)}{dxdQ^2} = \frac{2\pi\alpha^2}{xQ^4}\left(1+(1-y)^2F_2^{c\bar{c}}(x,Q^2)\right)$$

As $F_L^{c\bar{c}}$ is predicted to be very small, it is neglected in this equation [36–38]. Although the rates of charm production are significantly higher on photoproduction, in DIS the hadronic component of the photon is eliminated, and more reliable theoretical and experimental results can be obtained.

1.6.4 Charm Fragmentation

The fragmentation of the charm quark into the hadrons that can be reconstructed in the final state is a non-perturbative process described only by phenomenological models. The c quark production process involves the charm mass, which is large enough to allow reliable perturbative QCD calculations, but the fragmentation of the c quark into a charmed hadron involves the long range, non perturbative effects of light quarks and soft gluons.

Peterson Fragmentation

The most common fragmentation model is that of Peterson [39], which uses quantum-mechanical methods to calculate the amplitude for fragmentation of a heavy quark Q into a hadron $Q\bar{q}$ containing also the light quark q. The momentum fraction z taken from the c quark to create the charmed hadron distributes according to

$$D_{c\to D}(z;\epsilon) = \frac{Nz(1-z)^2}{((1-z)^2+\epsilon z)^2} \ ,$$

where N is a normalisation constant and ϵ is a free parameter.

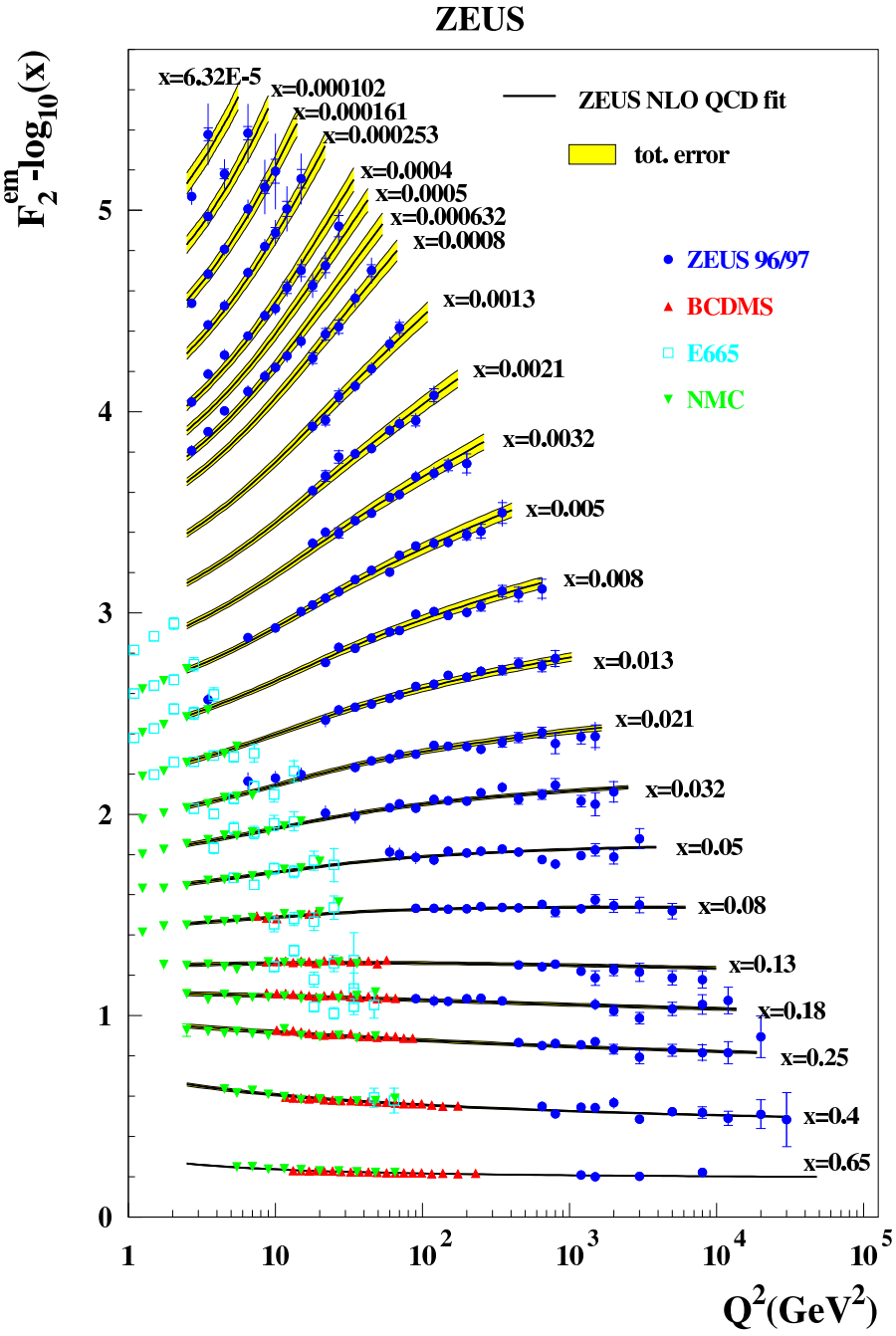

Figure 1.3: Measurement of the structure function F_2 as a function of Q^2 for different values of x.

Chapter 2

The HERA collider and the ZEUS detector

2.1 The Hadron Electron Ring Accelerator

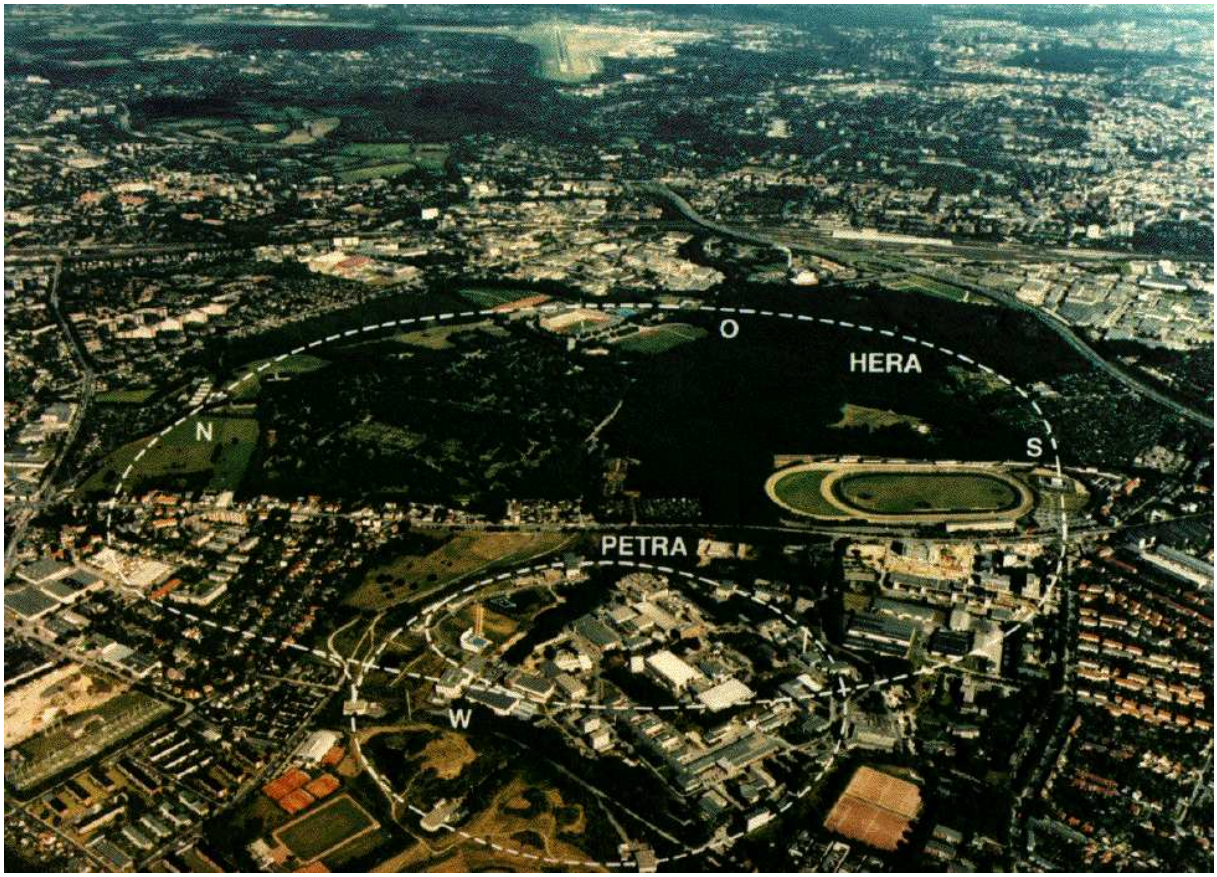

Figure 2.1: View of DESY.

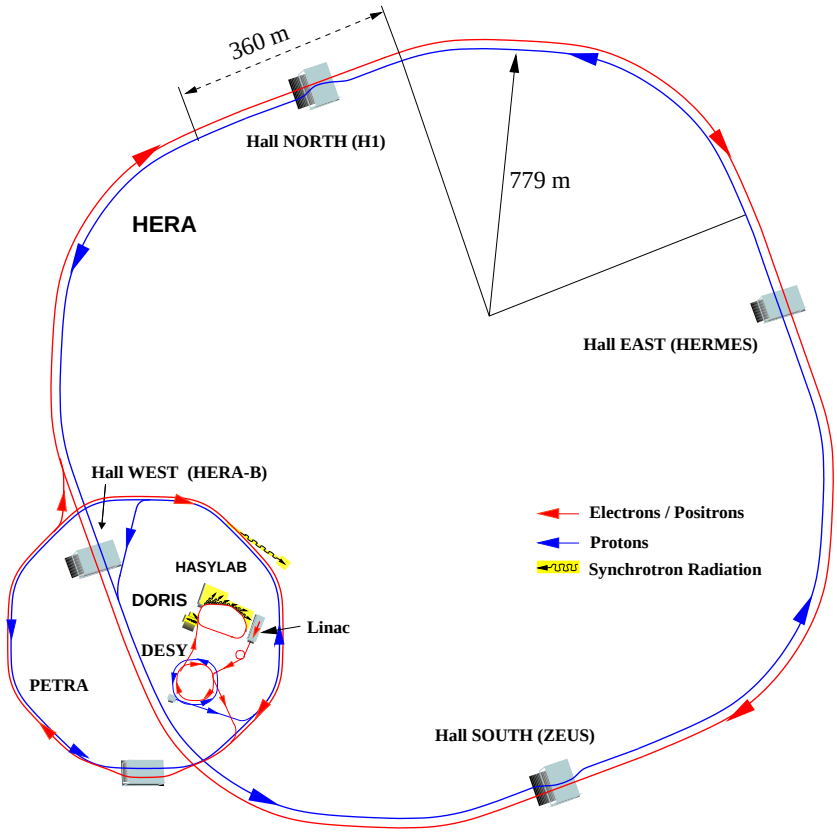

Figure 2.2: The HERA accelerator complex. Four experiments are located in the experimental halls : South (ZEUS), West (HERA-B), North (H1), and East (HERMES).

The HERA (Hadron Elektron Ring Anlage) collider is located at DESY in Hamburg, Germany. It offers unique opportunities to explore the structure of the proton as it is the first *ep* collider in the world. Figure 2.1 shows an aerial view of DESY and the surrounding area including the location of the two largest accelerators HERA and PETRA.

HERA was approved in 1984 and first collisions were observed in 1991. Operations for physics started in 1992. HERA consists of one storage ring for protons and one for electrons.The design energy is 30 GeV for electrons and 820 GeV for protons. Each storage ring consists of four 90° arcs connected by 360 m long straight sections and is located (10–25) m below ground. Superconducting magnets are used for the proton storage ring. Four experimental halls (North, South, East, West) are situated in the middle of the straight sections. The two collider experiments, H1 and ZEUS, are located in the northern and southern experimental halls, respectively. In both interaction regions electrons and protons collide head-on at zero crossing angle. Two fixed-target experiments, HERMES and HERA-B, have been installed in the eastern and western experimental halls, respectively. They make use of only

the HERA electron (HERMES) and proton (HERA-B) beams, respectively. HERMES [40] is investigating the spin structure of the nucleon and HERA-B [41] aims to study the $\mathcal{CP}$-violation in the $B^0\overline{B^0}$-system. Figure 2.2 shows the layout of the HERA collider, the four experimental halls and the system of pre-accelerators used at DESY. In a first step electrons and protons are accelerated using linear accelerators. A small storage ring PIA (Positron-Intensity-Accumulator) is used in between the linear accelerator and DESY II to accumulate electrons until sufficient intensity is reached. In a next step the particles are injected into DESY II (electrons) and DESY III (protons). After injection into PETRA and further acceleration, electrons and protons are injected into HERA. From 1995 to 1997 positrons were used instead of electrons because severe lifetime problems of the electron beam were observed. The reason is most likely the capturing of positively-charged dust which originates from ion getter pumps from the HERA electron vacuum system by the electron beam [42]. With the installation of new pumps in the winter shutdown 1997/1998 the problem has been significantly reduced and HERA switched back to electrons in 1998. Several HERA parameters from the 1997 runing period and the corresponding design values are given in table 2.1.

HERA parameters	Design Values		Values of 1997	
	$e^{\pm}$	p	e^{+}	p
Circumference (m)	6336			
Energy (GeV)	30	820	27.6	821.2
Center-of-mass energy (GeV)	314		301	
Injection energy (GeV)	14	40	12	40
Energy loss per turn (MeV)	127	$1.4 \cdot 10^{-10}$	127	$1.4 \cdot 10^{-10}$
Current (mA)	58	160	36	78
Magnetic field (T)	0.165	4.65	0.165	4.65
Number of bunches	210	210	174+15	174+6
Bunch crossing time (ns)	96			
Horizontal beam size (mm)	0.301	0.276	0.200	0.200
Vertical beam size (mm)	0.067	0.087	0.054	0.054
Longitudinal beam size (mm)	0.8	11	0.8	11
Specific luminosity ($cm^{-2}s^{-1}mA^{-2}$)	$3.6 \cdot 10^{29}$		$5.0 \cdot 10^{29}$	
Instantaneous luminosity ($cm^{-2}s^{-1}$)	$1.6 \cdot 10^{31}$		$1.45 \cdot 10^{31}$	
Integrated luminosity per year (pb^{-1}/a)	35		36.5	

Table 2.1: HERA parameters. In 1997 HERA operated with 174 colliding bunches, 15 positron-pilot bunches and 6 proton-pilot bunches.

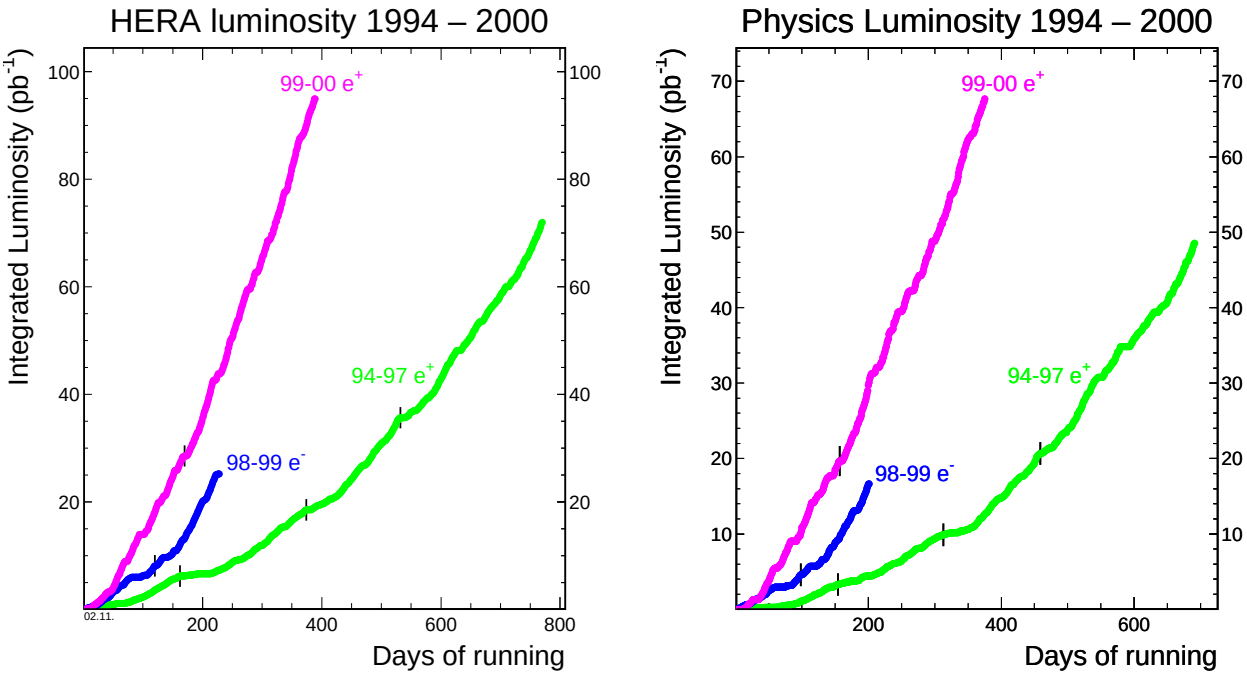

Figure 2.3: Integrated luminosity delivered by HERA in the different running periods (left plot) and the one taken with the ZEUS detector (right plot). The latter is used for physics analysis.

2.2 The ZEUS Detector

The ZEUS detector is a general purpose magnetic detector designed to study various aspects of electron-proton scattering. It has been in operation since 1992 [43] and consists of various sub-components to measure the hadrons and leptons in the final-state and, therefore, to characterize the final-state in terms of energy, direction, and type of the produced particles.

The coordinate system of the ZEUS detector is a Cartesian right-handed coordinate system. The origin ($(X, Y, Z) = (0, 0, 0)$) is located at the nominal interaction point. The Z-axis points in the proton beam direction, the Y-axis upwards, and the X-axis horizontally towards the center of HERA. The polar (azimuthal) angle θ (ϕ) is determined relative to the positive Z-axis (X-axis). With this definition the polar angle of the incoming electron beam is 180° and that of the incoming proton beam is 0°. The +Z-direction is referred as the *forward*, and the –Z-direction as the *backward* direction.

The ZEUS detector consists of the main detector located around the nominal interaction point and several small detectors positioned along the beam line in both positive and negative Z-directions. The main detector is shown in Figures 2.4 and 2.5

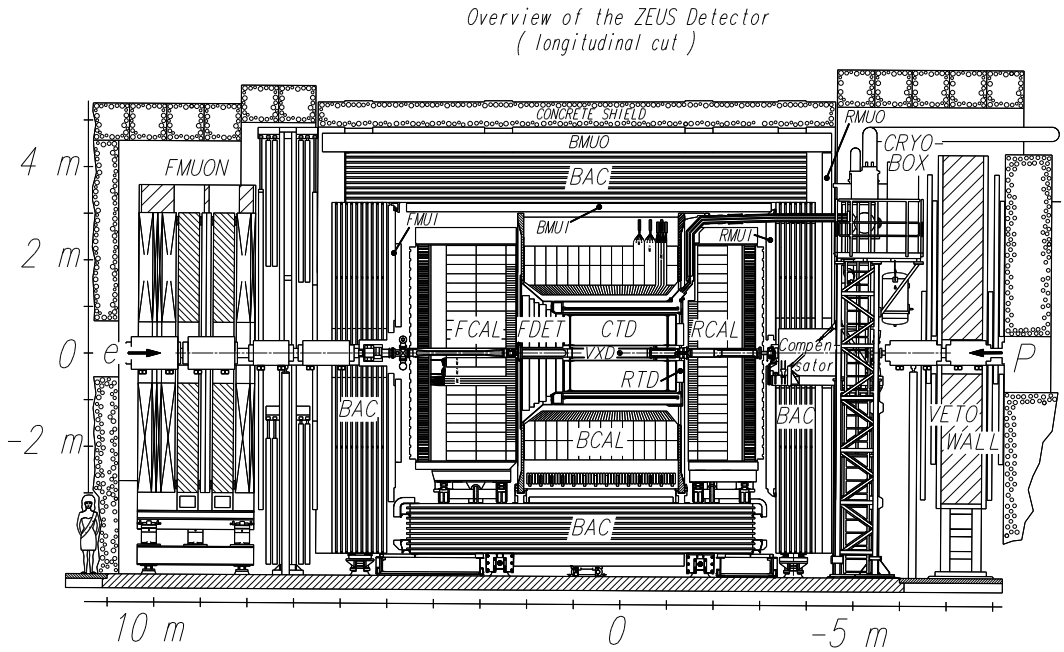

Figure 2.4: View of the ZEUS detector along the beam direction.

along and perpendicular to the beam direction, respectively. The design is asymmetric with respect to the Z-axis because of the large forward-backward asymmetry of the final-state system. The difference in the energy of the electron beam (27.5 GeV) and proton beam (820 GeV) results in a center-of-mass system which is moving in the direction of the proton beam relative to the laboratory frame. The inner part of the main detector consists of the tracking system enclosed by a superconducting solenoid which produces an axial magnetic field of 1.43 T. The CTD, a cylindrical drift chamber, surrounds the beam pipe at the interaction point. In order to provide additional means of track reconstruction in the forward (backward) direction, the CTD was supplemented by the FTD (RTD). The FTD consists of three sets of planar drift chambers with transition radiation detectors (TRD) in between. The RTD is one planar drift chamber with three layers. The vertex detector VXD measures the event vertex and possibly secondary vertices and improves the momentum and angular resolution of charged particles as determined with the CTD alone. In 1994 high voltage problems and damage due to synchrotron radiation caused part of the VXD to be off and it was removed.

The high resolution uranium calorimeter (UCAL) encloses the tracking detectors. It is subdivided into the forward (FCAL), barrel (BCAL), and rear (RCAL) parts.

The UCAL in turn is surrounded by an iron yoke made of 7.3 cm thick iron

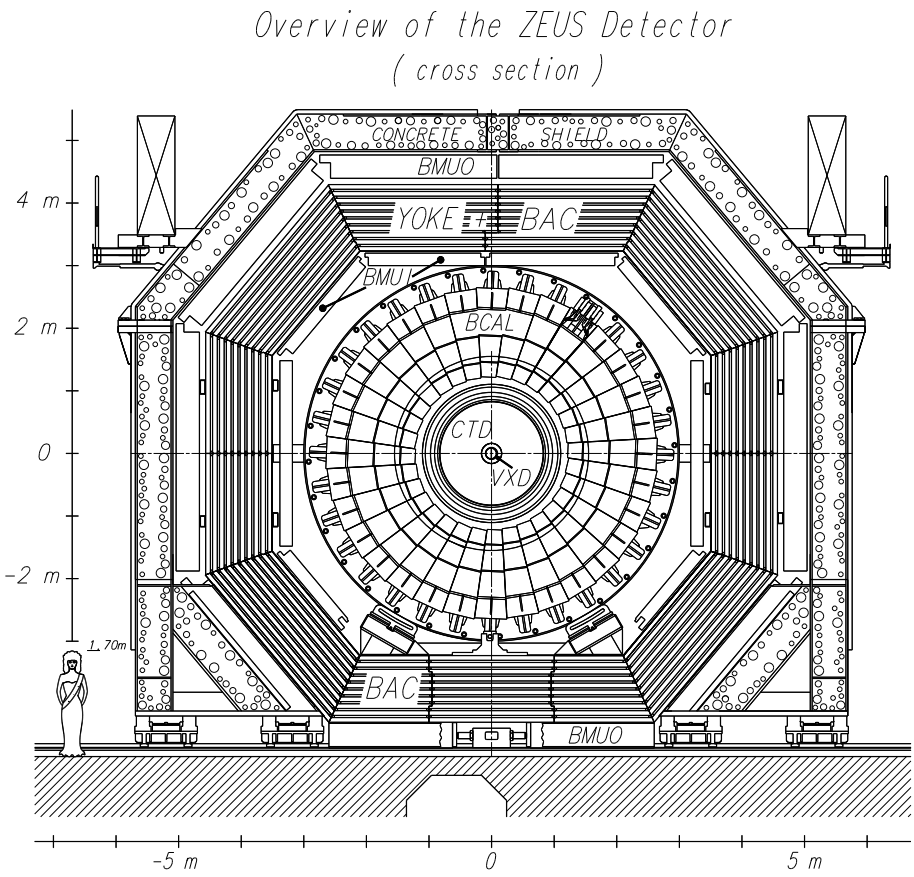

Figure 2.5: View of the ZEUS detector perpendicular to the beam direction. See text for a description of the components.

plates. The yoke serves two purposes: it provides a return path for the solenoid magnetic field flux and, in addition, is instrumented with proportional chambers. The latter design feature makes it possible to measure energy leakage out of the UCAL. The yoke is therefore referred to as the backing calorimeter (BAC). As the yoke is magnetized to 1.6 T by copper coils it is used to deflect muons. In order to detect and measure the momentum of muons, limited streamer tubes are mounted surrounding the iron yoke in the barrel (BMUI, BMUO) and the rear (RMUI, RMUO) regions. As the particle density and the muon momentum in the forward direction is higher than in the barrel and rear directions due to the energy difference of the electron and proton beam, the muon chambers in the forward direction are designed differently. Limited streamer tubes mounted on the inside of the iron yoke (FMUI) and drift chambers and limited streamer tubes mounted outside the iron yoke (FMUO) are used for this purpose. Two iron toroids provide a toroidal magnetic field of 1.7 T. In the backward direction at $Z = -7.3\,\mathrm{m}$, a veto wall outside the detector composed of iron and scintillation counters is used to reject background events dominated by proton-beam-gas reactions.

2.2.1 The Central Tracking Detector

The tracking system of the ZEUS detector consists of the forward, central and rear tracking devices, which operate under a high magnetic field of 1.43 T to achieve a high resolution for high momentum tracks. All the tracking quantities used in this analysis are provided by the Central-Tracking Detector (CTD) [44]. The CTD is a cylindrical drift chamber which provides a high precision measurement of the direction and transverse momentum of charged particles and of the event vertex. The position resolution in $r - \phi$ is about $230\,\mu$m and the transverse momentum resolution is

$$\frac{\sigma(p_t)}{p_t} = 0.0058 \cdot p_t(\text{GeV}) \oplus 0.0065 \oplus \frac{0.0014}{p_t} ,$$

where the first term corresponds to the resolution of the hit positions, the second term to smearing from multiple scattering within the CTD and the last term to multiple scattering before the CTD. The position of the interaction point in X and Y is measured with a resolution of 0.1 cm and in Z with a resolution of 0.4 cm.

The CTD is filled with a mixture of argon, CO_2, and ethane. Particle identification is possible by measurements of the mean energy loss dE/dx of charged particles within the tracking detector. The CTD covers a polar angle of $15° < \theta < 164°$ and the full range of the azimuthal angle ϕ. Its active volume has a length of 205 cm, an inner radius of 18.2 cm, and an outer radius of 79.4 cm.

The CTD is designed as a multi-cell superlayer chamber and subdivided into eight sections and nine superlayers. One octant is shown in Figure 2.6. The CTD consists of 576 cells with each cell being equipped with eight sense wires. The number of cells increases from 32 in the innermost superlayer to 96 cells for the outermost superlayer. Every other superlayer has its sense wires rotated by a certain angle with respect to the beam axis. The angles for each superlayer are given in Figure 2.6. With this configuration the Z position of a track can be reconstructed with an accuracy of aproximately 2 mm.

2.2.2 The Uranium-Scintillator Calorimeter (UCAL)

Calorimeters in particle physics measure the energy of particles by their absorption in a medium that becomes ionised or excited through shower processes. The ZEUS calorimeter (UCAL) has been designed as a sampling calorimeter, where absorber layers alternate with scintillator layers, which are the optical readout. The calorimeter is required to be hermetic with a nearly full solid-angle coverage and to have a good hadronic energy resolution by achieving an equal response to electromagnetic and hadronic particles.

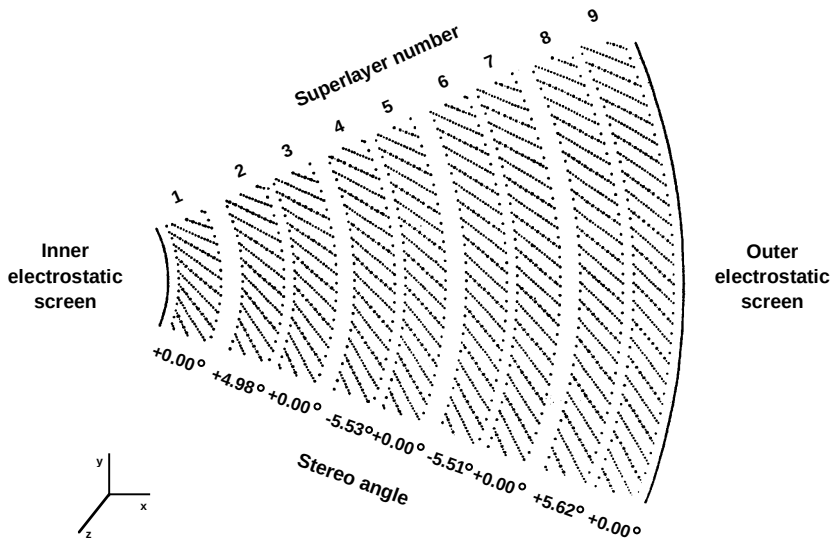

Figure 2.6: Layout of a CTD octant. Each octant has nine superlayers with the even numbered ones declined with respect to the beam axis ('Stereo angle').

The UCAL is divided into three parts, which cover different polar angles [45–47]. All parts of the calorimeter, FCAL ($2.2° < \theta < 39.9°$), BCAL ($36.7° < \theta < 128.1°$), and RCAL ($128.1° < \theta < 176.5°$) are built of alternating layers of 3.3 mm thick depleted uranium and 2.6 mm thick plastic scintillator plates (SCSN38). The natural radioactivity of ^{238}U is used as a reference signal to calibrate the readout channels to a precision of $< 0.2\%$.

Uranium is an advantageous absorber for hadron calorimetry, since it provides a high yield of spallation neutrons which impart the energy to the hydrogen nuclei of the scintillator. Together with an additional contribution of photons from neutron capture of the uranium, this helps to compensate the signal loss of hadrons arising from the loss of binding energy, nuclear fission fragments and from undetected decay products. Electrons and photons do not suffer such losses as they interact predominantly with the atomic electrons and not with the nuclei. The ratio between the pulse heights of electrons and hadrons, e/h, which has been achieved is

$$e/h \;=\; 1.00 \;\pm 0.03$$

The three calorimeter parts are subdivided into modules. The modules are transversally separated into towers and the towers in turn longitudinally into electromagnetic (EMC) and hadronic sections (HAC). The design of an FCAL module is shown in figure 2.7. The FCAL and RCAL modules are planar and perpendicular with respect to the beam axis (see figure 2.4), while the BCAL modules are wedge-shaped and projective in the polar angle. The calorimeter modules are further segmented

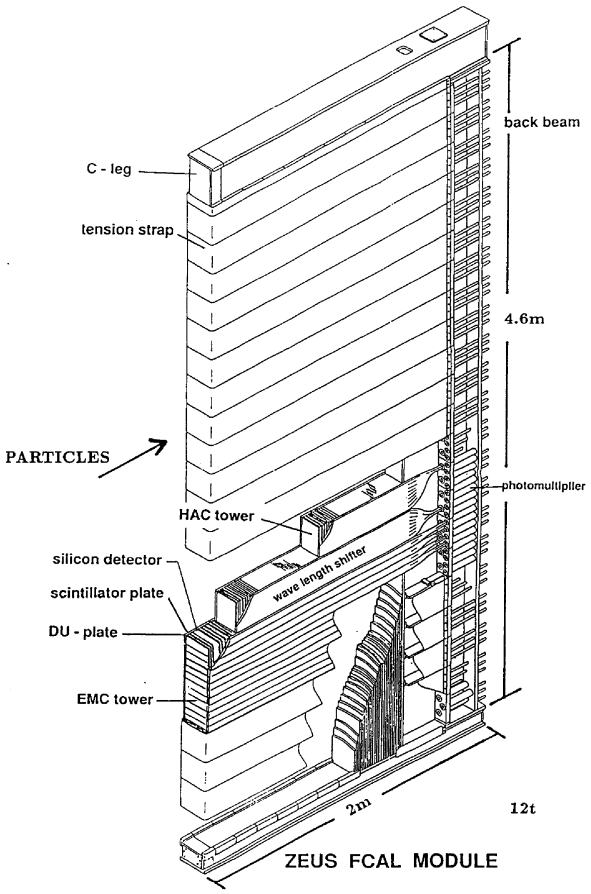

Figure 2.7: Layout of a FCAL module. The UCAL modules are subdivided into one electromagnetic (EMC) and two hadronic (HAC1,HAC2) sections, which in turn are divided into cells. A cell is read out on two opposite sides by one wavelength shifter each.

into cells. The design of the three calorimeter parts takes into account the different particle densities and energies due to the asymmetric electron and proton beam energies. Each EMC section is segmented transversally into four cells (two in RCAL), while a HAC tower is not divided transversally. They are instead longitudinally subdivided into two (one in RCAL) hadronic cells (HAC1, HAC2). Each cell is read out on two opposite sides. This is done on each side by a wavelength shifter coupled to one photomultiplier tube. The information of both photomultiplier tubes is used to provide a limited reconstruction of the position of the measured particle and to check the uniformity of the readout.

The single particle energy resolution for electrons and hadrons was determined in test-beam experiments to be $\sigma_E/E = 0.18/\sqrt{E}$ and $\sigma_E/E = 0.35/\sqrt{E}$ respectively, where E is mesured in GeV.

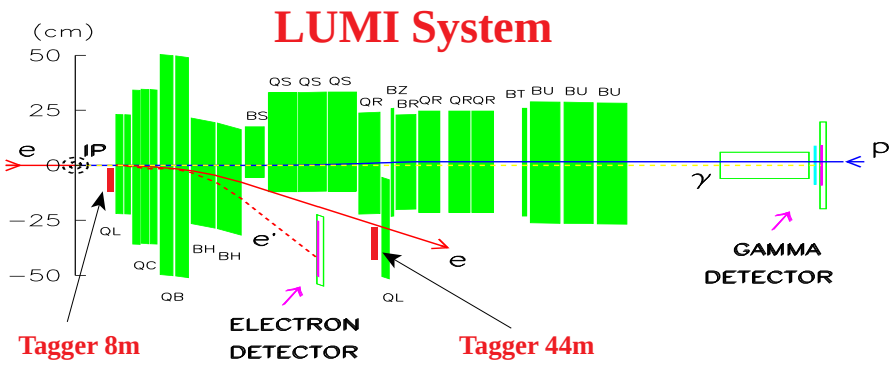

Figure 2.8: Location of ZEUS detectors in negative Z-direction. Shown are the gamma (LUMIG) and electron detectors (LUMIE) used for the luminosity measurement.

2.3 The Luminosity measurement

The luminosity, $\mathcal{L} \equiv N/\sigma$, relates the number of events N with the cross section σ. A precise determination of the luminosity is essential for any cross section measurement in a high energy physics experiment. The luminosity of ep-collisions at HERA is measured by observing the rate of hard bremsstrahlung photons from the Bethe-Heitler process $ep \to e\gamma p$ [48]. As the theoretical cross section is known to an accuracy of 0.5% from QED calculations, a precise measurement of the photon rate permits a precise determination of the ep-luminosity at HERA.

Figure 2.8 shows the layout of the HERA magnet system and the ZEUS luminosity detectors in the backward (–Z)-direction. In the case of ZEUS this is done by two lead/scintillator electromagnetic calorimeters at Z = −34 m (LUMIE) and Z = −107 m (LUMIG). Photons with $\theta_\gamma < 0.5$ mrad originating from the Bethe-Heitler process $ep \to e\gamma p$ are detected by the LUMIG detector [49, 50]. The energy resolution of the LUMIG detector was measured under test-beam conditions to be $18\%/\sqrt{E}$. It was also determined that the carbon/lead filter placed in front of the detector to shield it against synchrotron radiation degrades the resolution to $23\%/\sqrt{E}$. The impact position of incoming photons can be determined with a resolution of 0.2 cm in X and Y, because at a depth of $7X_0$ 1 cm wide scintillator strips are installed within the LUMIG detector. The LUMIG detector is also used to determine the electron beam tilt and to measure photons from initial-state radiation.

The LUMIE calorimeter [49, 50] at Z = −35 m detects electrons in the limited energy range from 7 to 20 GeV which are produced under polar angles of less than 5 mrad with respect to the electron beam direction. These electrons are deflected by the HERA magnet system and leave the beam pipe at Z = −27 m through an exit window similar to the one in front of the LUMIG detector. The LUMIE detector

has an energy resolution of $18\%/\sqrt{E}$ under test-beam conditions. It was initially designed to measure the electrons of the Bethe-Heitler process $ep \to e\gamma p$ at the same time as the photons of this process are measured in the LUMIG detector. It was found that this was not necessary to have a precise measurement of the luminosity.

2.4 The ZEUS trigger and data acquisition systems

The short bunch crossing time at HERA of 96 ns, equivalent to a rate of of about 10^7 crossings per second , is a technical challenge and puts stringent requirements on the ZEUS trigger and data acquisition systems. The total interaction rate, which is dominated by background from upstream interactions of the proton beam with residual gas in the beampipe, is of the order 10 - 100 kilo-events per second (10 - 100 kHz) while the rate of *ep* physics events in the ZEUS detector is of the order of a few Hz [51, 52]. Other background sources are electron beam gas collisions, beam halo and cosmic events.

ZEUS employs a sophisticated three-level trigger system in order to select *ep* physics events efficiently while reducing the rate to a few Hz. A schematic diagram of the ZEUS trigger system is shown in Figure 2.9.

The First Level trigger (FLT) is a hardware trigger, designed to reduce the input rate below 1 kHz. Each detector component has its own FLT, which stores the data in a pipeline, and makes a trigger decision within 2 μs after the bunch crossing. The decision from the local FLTs are passed to the Global First Level Trigger (GFLT), which decides whether to accept or reject the event, and returns this decision readout within 4.4 μs. The typical information available at FLT are CAL activity (total transverse energy, missing transverse momentum,...), CTD tracks (number of tracks,...), hits in the muon chambers, etc.

If the event is accepted, the data is fully digitalised and transferred to the Second Level Trigger (SLT). The trigger signals at the SLT have a better resolution than those at the FLT. Moreover, some information is first available at the SLT like CAL timings, which are useful in rejecting non-*ep* background events. The SLT is designed to reduce the rates to the order of 50-100Hz. Each detector component has its own SLT, which passes a trigger decision to the Global Second trigger (GSLT) [53].

If the event is accepted by the GSLT, all detector components send their data to the Event Builder (EVB), which combines all the data of an event into a single record of ADAMO [54] database tables. This is the data structure on which the Third Level Trigger (TLT) code runs. The TLT is software based and runs part of the offline reconstruction code. It is designed to reduce the rate to a few Hz.

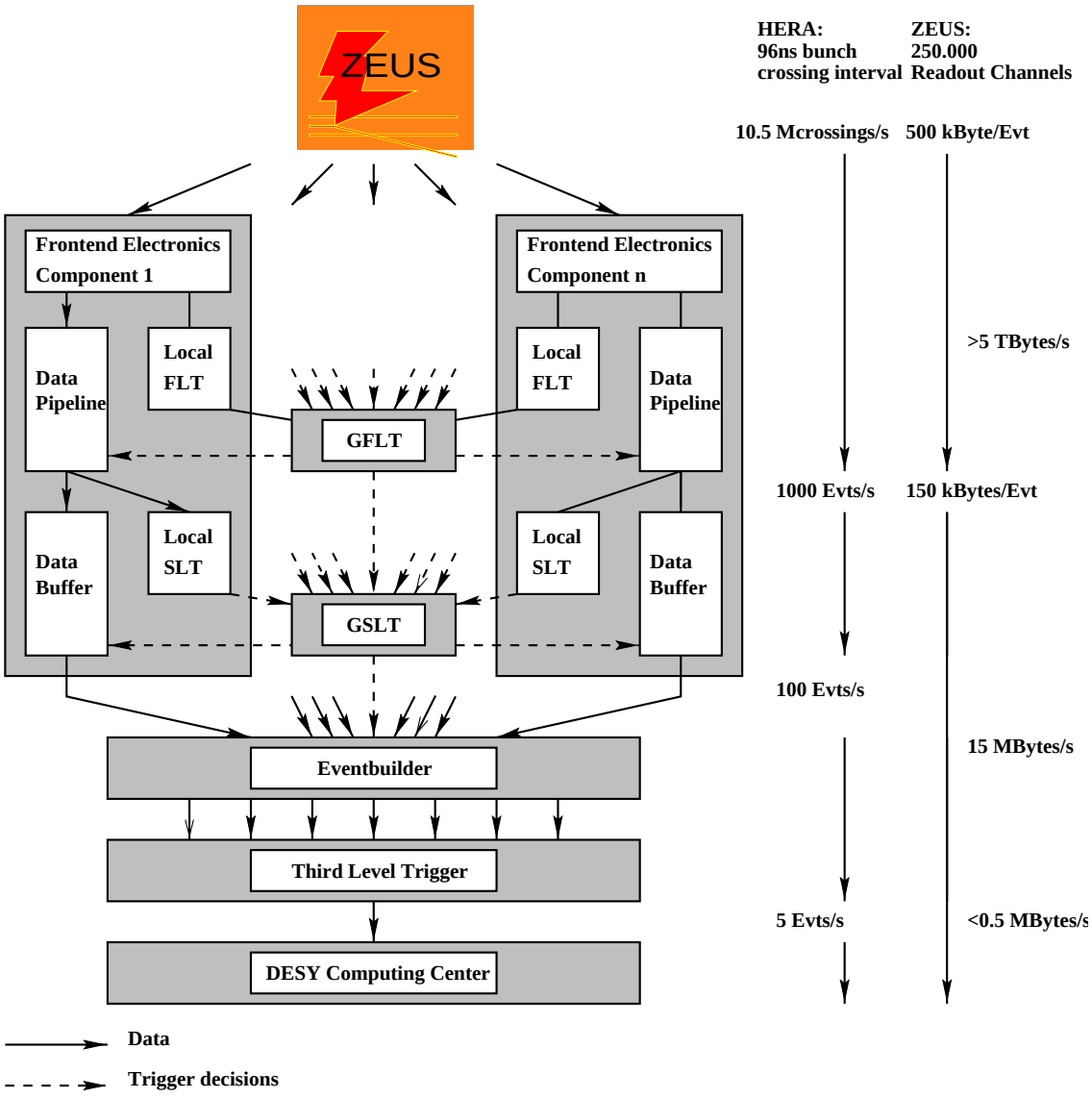

Figure 2.9: Schematic diagram of the ZEUS trigger and data acquisition systems.

2.5 Event reconstruction and analysis

The scheme of the ZEUS offline and Monte Carlo (MC) simulation programs is shown in figure 2.10. Events from the real detector or simulated events are reconstructed by the program ZEPHYR, where the signals of the different calorimeter components are calibrated and highly complex tasks like tracking reconstruction are performed. After reprocessing the raw data, the user has access to the raw and reconstructed quantities via the program EAZE. In the framework of EAZE, the user writes his own analysis program in either Fortran or C. It is used to reconstruct relevant quantities and perform selection cuts. Subsets of the data or MC simulated events can be saved for further analysis. The program LAZE is an event display program which allows

graphical viewing of various aspects of an event including the tracks of charged particles in the CTD, energy depositions in the CAL, and other component-related quantities. To allow fast access to specific types of events during reconstruction it is checked wether each event meets one of the conditions designed by the ZEUS analysis groups. If a specific condition is met, a flag called a DSTBIT is set. Before analyzing detailed component information in the user's EAZE program, the events can be preselected by requiring certain DSTBITS. This allows a faster loop over the whole data sets since only those events are processed further.

MC events are generated using the program ZDIS which contains a shell environment to steer a number of MC generator programs. The output data is stored in the same (ADAMO) format as the data from the real detector and passed to the ZEUS detector simulation program MOZART, based on the CERN GEANT program [55]. A simulation of the ZEUS trigger chain is done by the program ZGANA. Interfaces between the programs used for MC generation and the programs EAZE and LAZE provide specific MC information such as generated kinematic quantities, vertices and particles to the user. An overview of the physics analysis environment of the ZEUS experiment can be found in [56].

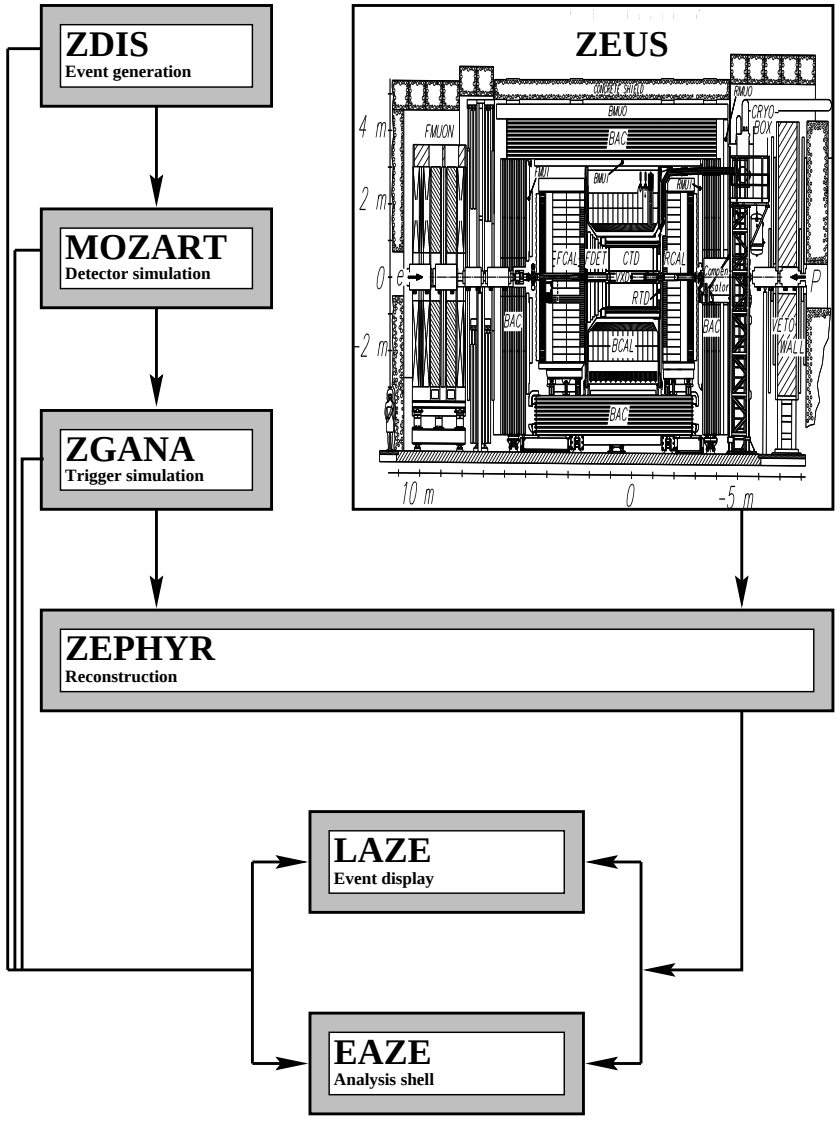

Figure 2.10: Interrelationship of the ZEUS offline and Monte Carlo (MC) simulation programs.

Chapter 3

Event Selection

In this chapter the selection criteria for the DIS charmed hadron enriched sample is presented. The data used for the present analysis was collected with the ZEUS detector at HERA during the 1998-2000 period. During 1998 and half of 1999, HERA operated with protons of energy $E_p = 920$ GeV and electrons of energy $E_e = 27.5$ GeV. From mid of 1999 to 2000, the experiment used a positron beam instead of an electron beam. The results are based on e^-p and e^+p samples corresponding to integrated luminosities of 16.7 ± 0.3 pb^{-1} and 65.1 ± 1.5 pb^{-1}, respectively. The whole sample is used in the reconstruction of the D^0, D_s^+ and D^{*+} mesons. For the reconstruction od D^+ mesons and due to trigger availability, only the positron sample was used.

3.1 Event Reconstruction

The final state of a DIS events contains two distinc objects : the scattered positron and the hadronic system. The hadronic system combines everything that is is not attributed to the scattered positron in one single object. The hadronic system can be further broken down into jets, which appear after the hadronisation of quarks and gluons, and the proton remnant.

3.1.1 The scattered positron

The identification of the scatterd electron, and accurate measurement of both its angle and energy, are important as the kinematics is partially determined from these quantiies. There are a number of software packages that are usedwithin the ZEUS analysis framework. The most commonly used is the neural-network SINISTRA [57]. In many DIS events, the scattered electron is detected in the RCAL, well separated from the hadronic activity in the event. In general, hadronic deposits shower deeper

into the calorimeter than positron deposits. There are however certain complications, such as multiple scattering in dead material before the electron reaches the calorimeter, and low energy hadrons, or π^0 conversions can "fake" a lepton signal. The SINISTRA algorithm has been trained on low Q^2 NC data and Monte Carlo to optimise its efficiency at differenciating between electromagnetic and hadronic deposits. Previous studies have shown that the efficiency has a turn on curve but it is between 99% and 100% above 10 GeV.

Energy and Position Correction

The position of the scattered electron can be identified using the calorimeter itself, but a better resolution can be obtained by using the matched track from the CTD, or the position from the HES or SRTD. The resolution of the SRTD is about 3mm, compare to centimeters in the calorimeter. The energy of the scattered electron is corrected for losses in dead material between the interaction points and the calorimeter. The components used for this corrections are the SRTD and the Presampler. The number of particles in the shower is proportional to the energy loss. Extensive studies of over-constrained events have determined the correction to be applied in data and Monte Carlo for each component. A non-uniform correction is also made to the energy measured in the calorimeter, based on the differing responses of the cells close to the cracks between the calorimeter towers. If the lepton is not detected near to these cracks, no correction is applied.

3.1.2 The Hadronic System

The hadronic activity within an event is reconstructed using the ZUFOS routine, which uses calorimeter and CTD information. Details can be found in [58], but we give an overview. Calorimeter clusters, known as "islands" are formed considering the highest-energy neighbour for each cell. A cell with no higher energy neighbours is defined as the center of the island. The island formed in the EMC and HAC sections of the calorimeter are then matched with each other into "cone islands". Track matching is then performed using good tracks from the CTD, defined as those passing through at least three superlayers. These tracks are extrapolated to the calorimeter face, and matched to the energy deposits. If a track is matched to a deposit, the CTD is used to determine the energy and momentum of the object, provided the CTD momentum resolution is better than the calorimeter energy resolution. If a track is not matched to an energy deposit, the energy is calculated assuming that the particle is a pion. If a cone island has no track matched to it, it is assumed to originate from a photon, and its momentum is calculated ignoring the mass and assuming an origin at the reconstructed primary vertex. If a cone island has more than three tracks associated to it, its momentum is also calculated in this

way. Once the objects have been trated in these way, they are referred to as ZUFOs, or ZEUS Unidentified Flow Objects.

The hadronic final state is defined in terms of detector observables: δ_h, the hadronic $E - p_z$ and the transverse momentum of the hadronic system p_T, h, which are defined as

$$\delta_h = \sum_i (E - p_{z,i})$$
$$p_{T,h}^2 = (\sum_i p_{x,i})^2 + (\sum_i p_{y,i})^2$$

where the sums run over all the calorimeter clusters that are not associated with the scattered lepton. These two observables can be combined to give another variable:

$$\cos\gamma_h = \frac{p_{T,h}^2 - \delta_h^2}{p_{T,h}^2 + \delta_h^2}$$

which is, at leading order, the polar angle of the struck quark.

3.2 Kinematic Reconstruction

The quantities Q^2, x and y can be reconstructed in different ways, each being suited to a certain kinematic region. This is possible due to the ability to reconstruct the energy and the angle of the scattered lepton, and almost the full hadronic final state with the ZEUS detector. The criteria for the ideal choice of reconstruction method are optimum resolution, and minimisation of migrations, that is, systematics shifts of the reconstructed values with respect to the true kinematics. The reconstruction of these variables can also be achieved using a combination of methods: two independent variables can be reconstructed using two different methods. Then the third one can be calculated using the relation

$$Q^2 = xys \ ,$$

where s is the center of mass energy of the ep collision. For the analysis presented here, the method used for the reconstruction of the kinematic variables was the Sigma Method.

Electron Method

This method uses only the measurement of the scattered electron angle, θ_e, and energy, E'_e. For a given value of the initial electron beam energy E_e, the kinematic

variables Q^2, y and x are given by

$$\begin{aligned} Q^2_{el} &= 2E_e E'_e(1+\cos\theta_e) \\ y_{el} &= 1 - \frac{E'_e}{2E_e}(1-\cos\theta_e) \\ x_{el} &= E_e E'_e \left(\frac{1+\cos\theta_e}{2E_p E_e - E_p E'_e(1-\cos\theta_e)} \right) \end{aligned}$$

This method is sensitive to initial and final state radiation as it implicitly assumes that the lepton interacts with the full beam energy E_e, and leaves with the scattered energy E'_e. A y_{el} cut can be used to reduce photoproduction background, where some hadronic activity cause a fake electron-like deposit, tipically in the FCAL, causing a high y_{el} value.

Jacquet-Blondel Method

The Jacquet-Blondel method [59] uses only the hadronic system to reconstruct the kinematics of the event. This is naively the quark angle and energy, but this cannot be measured directly. Instead, the sums of $E - p_z$ and p_T of all the final state particles excluding the scattered lepton are made:

$$\begin{aligned} \delta_h &= \sum_h (E - p_z) \\ p_{T,had} &= \sum_h p_{T,h} \ , \end{aligned}$$

and the kinematics is given by:

$$\begin{aligned} y_{JB} &= \frac{\delta_h}{2E_e} \\ Q^2_{JB} &= \frac{p^2_{T,had}}{1-y_{JB}} \\ x_{JB} &= \frac{Q^2_{JB}}{s y_{JB}} \end{aligned}$$

Although this method does not provides the best resolution, y_{JB} provides a measurement of the hadronic activity in the event. Therefore, y_{JB} can be used a useful background cut.

Double Angle Method

The double angle method [60] is a reconstruction method that is based on the angles both the hadronic system and the scattered lepton. The hadronic angle, which can naively interpreted as the angle of the struck quark, is given by

$$\cos\gamma = \frac{p^2_{T,had} - \delta^2_h}{p^2_{T,had} + \delta^2_h} \ ,$$

where $p_{T,had}$ and δ_h are given above. The reconstruction of the kinematics is done by

$$Q^2_{DA} = 4E_e^2 \sin\gamma \frac{1+\cos\theta_e}{\sin\gamma + \sin\theta_e - \sin(\gamma+\theta_e)}$$
$$y_{DA} = \frac{\sin\theta_e + (1-\cos\theta_e)}{\sin\gamma + \sin\theta_e - \sin(\gamma+\theta_e)}$$
$$x_{DA} = \frac{E_e \sin\gamma + \sin\theta_e + \sin(\gamma+\theta_e)}{E_p \sin\gamma + \sin\theta_e - \sin(\gamma+\theta_e)}$$

Since angles are in general better measured than energies with the ZEUS detector, this method is competitive over a large proportion of the kinematic region available.

Sigma Method

The Σ method [61] uses both the scattered lepton and the hadronic system to reconstruct the kinematics. The variables are given by:

$$y_\Sigma = \frac{\delta_h}{\delta} \tag{3.1}$$
$$Q^2_\Sigma = \frac{E'^2_e \sin^2\theta_e}{1-y_\Sigma} \tag{3.2}$$
$$x_\Sigma = \frac{Q^2_\Sigma}{s y_\Sigma}\ . \tag{3.3}$$

In the case where no particle escapes detection, this method is identical to the double-angle method, but its adventage is that it properly accounts for initial-state radiation.

3.3 Trigger Selection

The ZEUS data acquisition system uses a three level trigger system to select events online [62, 63]. After each step, the data volume is reduced and more time is available, allowing for the reconstruction of more complicated information on which to base trigger decisions.

3.3.1 First Level Trigger

At the FLT level, DIS events were triggered by either FLT30, FLT44 or FLT46.

- FLT30 requires an isolated CFLT tower (ISO-e) with energy greater than 2.08 GeV and that the HAC tower behind it is less than a third of the EMC energy or less than 0.95 GeV. In addition, one of the following conditions were imposed:

  - The RCAL EMC energy (excluding the first RCAL ring of 20×20 cm^2 towers) is larger than 2 GeV.
  - .OR. The total RCAL EMC energy is above 3.7 GeV.
  - .OR. At least one CFLT tower (excluding the first RCAL ring and the three FCAL rings closest to the beam) with energy above 0.5 GeV .AND. the presence of a SRTD hit.

- FLT44 triggers if:
  - the energy deposited at the BCAL EMC section is larger than 4.8 GeV. A CTDFLT requirement is imposed in addition.
  - .OR. The total RCAL EMC energy (excluding the first ring of 20×20 cm^2 towers) is larger than 3.4 GeV.

- FLT46 is a logical .AND. od ISO-e and a CTDFLT requirement.

FLT44 is the softer conditions for events outside the first RCAL ring while FLT30 triggers the events inside the first RCAL ring.

3.3.2 Second Level Trigger

At the SLT beam gas background is furthered suppressed with the help of the UCAL timing information. During the 1998-2000 data taking a requirement on the total $E - P_z$ was already present at the SLT. DIS06 ($E - P_z > 29$ GeV) bit was required.

3.3.3 Third Level Trigger

At the third level, events having at least a reconstructed D^{*+}, D^0, D^+, D_s^+ or Λ_c^+ candidate, as well as a scattered-electron candidate, were kept for further analysis. The efficiency of the online reconstruction for any of the above hadrons, determined relative to an inclusive DIS trigger, was generally above 95% A brief description is given below.

HFL10 triggers if a D^*+ candidate decaying in the channel $D^{*+} \rightarrow D^0(\rightarrow K^-\pi^+)\pi_s^+$ was found in the event. In addition, the following cuts are required:

- $-50\ cm < Z_{vertex} < 50\ cm$ and $3 < N_{tracks} < 100$
- $p_T(K) > 0.35$ GeV and $p_T(\pi) > 0.4$ GeV (from D^0 decay)
- $p_T(\pi_{slow}) > 0.1$ GeV
- Mass windows : $1.4 < M(K\pi) < 2.2$ GeV and $M(K\pi\pi_s) - M(K\pi) < 170$ GeV

- $p_T(D^*) > 1.35\,\text{GeV}$ GeV

.OR. same cuts plus DIS cuts (only for e^+ data):

- DIS electron from Sinistra, Elec5 or EM finders
- $E_e > 4.0$ GeV, box cut $6 \times 12\ cm^2$, $(E - p_z) > 30$ GeV

HFL12 triggers if a D^0 candidate decaying in the channel $D^0 \rightarrow K^-\pi^+$ was found in the event. In addition, the following cuts are required:

- $-50\ cm < Z_{vertex} < 50\ cm$ and $2 < N_{tracks} < 100$
- $p_T(K) > 0.7\,\text{GeV}$ and $p_T(\pi) > 0.7$ GeV
- Mass windows : $1.6 < M(K\pi) < 2.2\,\text{GeV}$
- $p_T(D^0) > 2.8$ GeV, $|\eta(D^0)| < 2.0$

.OR. same cuts plus DIS cuts (only for e^+ data)

- DIS electron from Sinistra, Elec5 or EM finders
- $E_e > 4.0$ GeV, box cut $6 \times 12\ cm^2$, $(E - p_z) > 30$ GeV

HFL13 triggers if a D_s^+ candidate decaying in the channel $D_s^+ \rightarrow \phi(\rightarrow K^+K^-)\pi^+$ was found in the event. In addition, the following cuts are required:

- $-50\ cm < Z_{vertex} < 50\ cm$ and $3 < N_{tracks} < 100$
- $p_T(K) > 0.7\,\text{GeV}$ and $p_T(\pi) > 0.7$ GeV
- Mass windows : $1.6 < M(KK\pi) < 2.2\,\text{GeV}$
- $p_T(D_s) > 1.8$ GeV, $|\eta(D_s)| < 2.0$
- No wrong charges

.OR. same cuts plus DIS cuts (only for e^+ data):

- DIS electron from Sinistra, Elec5 or EM finders
- $E_e > 4.0$ GeV, box cut $6 \times 12\ cm^2$, $(E - p_z) > 30$ GeV

HFL21 triggers if a D^+ candidate decaying in the channel $D^+ \rightarrow K^-\pi^+\pi^+$ was found in the event. In addition, the following cuts are required:

- $-50\ cm < Z_{vertex} < 50\ cm$ and $3 < N_{tracks} < 100$

- $p_T(K) > 0.45\,\text{GeV}$ and $p_T(\pi) > 0.45$ GeV
- Mass windows : $1.7 < M(K\pi\pi) < 2.1\,\text{GeV}$
- $p_T(D^{+/-}) > 2.8$ GeV, $|\eta(D^{\pm})| < 2.0$

plus DIS cuts:

- DIS electron from Sinistra, Elec5 or EM finders
- $E_e > 4.0$ GeV, box cut $6 \times 12\ cm^2$, $(E - p_z) > 30$ GeV

HFL22 triggers if a Λ_c^+ candidate decaying in the channel $\Lambda_c^+ \rightarrow K^- p\pi^+$ was found in the event. In addition, the following cuts are required:

- $-50\ cm < Z_{vertex} < 50\ cm$ and $3 < N_{tracks} < 100$
- $p_T(K) > 0.45\,\text{GeV}$, $p_T(p) > 0.45\,\text{GeV}$ and $p_T(\pi) > 0.45\,\text{GeV}$.
- Mass windows : $2.1 < M(Kp\pi) < 2.5\,\text{GeV}$
- $p_T(\Lambda_c) > 3.6$ GeV, $|\eta(\Lambda_c)| < 2.0$

plus DIS cuts:

- DIS electron from Sinistra, Elec5 or EM finders
- $E_e > 4.0$ GeV, box cut $6 \times 12\ cm^2$, $(E - p_z) > 30$ GeV

3.4 DIS Selection Criteria

Selection cuts are intendended to optimise the NC DIS sample, reducing the background from photoproduction processes. The ratio signal to background events is optimised by the kinematic cuts in (δ, Q^2, y) and also some additional requirements on the scattered electron candidate. On the event sample that passed the TLT requirements, the following criteria were applied:

- $40 < E - p_z < 65\,\text{GeV}$

  For a perfectly measured DIS event δ should have the value $\delta = 2E_e = 55$ GeV, from energy-momentum conservation. Particles that scape through the beam pipe do not contribute to the overal δ. In photoproduction events the scattered electron is not detected. This effectively lowers the measured δ for these type of events, so the δ distribution peaks at lower values, typically bellow 30 GeV.

- $-50 < Z_{vertex} < 50\ cm$

  The Z coordinate of the vertex is resticted to this range to garantee a good understanding of the acceptances of both the calorimeter and the central tracking detector.

- $y_{el} < 0.95$

  Sometimes SINISTRA identifies an electromagnetic cluster in the FCAL as the most probable candidate for the scattered electron. Usually this is due to a π^0, while the real scattered electron can be found elsewhere in the detector. As these "fake" electrons are produced in a decay, they have an energy that is much lower than expected for high Q^2 event. From the relation 3.6 it follows that y_{el} will be very high for such misidentified electrons. The cut $y_{el} < 0.95$ is intended to reject a large fraction of those events.

- Electron energy and probability cut

  We require to have at least one DIS scattered electron candidate found with SINISTRA and minimum energy $E_e > 10\,\mathrm{GeV}$.

- Box cut

  The impact point of the scattered electron in the RCAL must lie outside the region $26 \times 14\ cm^2$, which correponds to a harder box cut that those considered in the DIS01 and DIS03 triggers. The best estimation of the electron position is used (HES and STRD when available).

- $y_{JB} > 0.02$

  This cut removes part of the phase space that is characterised by low total hadronic energy in the calorimeter.

The angle of the scattered electron was determined using either its impact position on the CAL inner face or a reconstructed track in the CTD. When available, SRTD and HES were also used. The energy of the scattered electron was corrected for non-uniformity effects caused by cell and module boundaries.

The selected kinematic region of the measurement was

$$1.5 < Q^2 < 1000\,\mathrm{GeV}^2 \qquad 0.02 < y < 0.7\ .$$

3.5 Tracking Selection

In this analysis we use tracks reconstructed using only the CTD and originated from the primary vertex, passing through at least three superlayers to ensure good reconstruction, and having a minimum transverse momentum $p_T > 0.1$ GeV.

Chapter 4

Reconstruction of Charm Hadrons

In this chapter we reconstruct the D^{*+}, D^0, D^+, and D_s^+ charm mesons in the range of transverse momentum $p_T(D) > 3\,\mathrm{GeV}$ and pseudorapidity $|\eta(D)| < 1.6$. For each meson, a specific decay channel was used in the reconstruction. For the D_s^+, the $p_T(D_s^+)$ requirement was relaxed to $p_T(D_s^+) > 2\,\mathrm{GeV}$, as the kinematics of the decay channel used in its reconstruction kept the combinatorial background at acceptable levels. The reconstruction of the Λ_c^+ baryon was attempted using the decay $\Lambda_c^+ \to K^- p \pi^+$. The signal achieved had a statistical significance of around three standard deviations, and therefore it was not used.

The charm mesons were reconstructed using tracks measured in the CTD. Further background reduction was achieved by imposing cuts on the transverse momenta and decay angles of the charm-hadron decay products. The cut values were tuned using Monte Carlo (MC) simulation to enhance signal over background ratios while keeping acceptances high.

The inclusive productions of the D^0 and D^{*+} mesons and related quantities involved in the measurements of fragmentation properties can be obtained from the combination of three independent samples [2]: those of D^0 candidates with and without a "ΔM" tag and that of "additional" D^{*+} candidates. The samples are described below. The rationale for this division [2] will become apparent in Chapter 6.

4.1 Reconstruction of D^0 mesons

The D^0 mesons were reconstructed from the decay $D^0 \to K^-\pi^+$. In each event, tracks with opposite charges and $p_T > 0.8\,\mathrm{GeV}$ were combined in pairs to form D^0 candidates. The nominal kaon and pion masses were assumed in turn for each track and the pair invariant mass, $M(K\pi)$, was calculated. The distribution of the cosine

of the D^0 decay angle (defined as the angle $\theta^*(K)$ between the kaon in the $K\pi$ rest frame and the $K\pi$ line of flight in the laboratory frame; details about boosting can be found in Appendix A) is flat, whereas the combinatorial background peaks in the forward and backward directions. To suppress the background, $|\cos\theta^*(K)| < 0.85$ was required.

For selected D^0 candidates, a search was performed for a track that could be a "soft" pion (π_s) in a $D^{*+} \to D^0\pi_s^+$ decay. The soft pion was required to have $p_T > 0.2\,\mathrm{GeV}$ and a charge opposite to that of the particle taken as a kaon. The p_T cut was raised to 0.25 GeV for a data subsample, corresponding to an integrated luminosity of $17\,\mathrm{pb}^{-1}$, for which the low-momentum track reconstruction efficiency was smaller due to the operating conditions of the CTD [64]. The corresponding D^0 candidate was assigned to a class of candidates "with ΔM tag" if the mass difference, $\Delta M = M(K\pi\pi_s) - M(K\pi)$, was in the range $0.143 < \Delta M < 0.148\,\mathrm{GeV}$. All remaining D^0 candidates were assigned to a class of candidates "without ΔM tag". For D^0 candidates with ΔM tag, the kaon and pion mass assignment was fixed by the track-charge requirements. For D^0 mesons without ΔM tag, the mass assignment is ambiguous. The pion and kaon masses can therefore be assigned to two tracks either correctly, producing a signal peak, or incorrectly, producing a wider reflected signal. To remove this reflection, the mass distribution, obtained for D^0 candidates with ΔM tag and an opposite mass assignment to the kaon and pion tracks, was subtracted from the $M(K\pi)$ distribution for all D^0 candidates without ΔM tag. The subtracted mass distribution was normalised to the ratio of numbers of D^0 mesons without and with ΔM tag obtained from a fit described below.

Figure 4.1 shows the $M(K\pi)$ distribution for D^0 candidates without ΔM tag, obtained after the reflection subtraction, and the $M(K\pi)$ distribution for D^0 candidates with ΔM tag. Clear signals are seen at the nominal value of $M(D^0)$ in both distributions. The distributions were fitted simultaneously assuming the same shape for signals in both distributions. To describe the shape, a "modified" Gaussian function (see Appendix B for details) was used:

$$\mathrm{Gauss}^{\mathrm{mod}} \propto \exp[-0.5 \cdot x^{1+1/(1+0.5\cdot x)}] \,,$$

where $x = |[M(K\pi) - M_0]/\sigma|$. This functional form described both data and MC signals well. The signal position, M_0, and width, σ, as well as the numbers of D^0 mesons in each signal were free parameters of the fit. Monte Carlo studies showed that background shapes in both distributions are compatible with being linear in the mass range above the signals. For smaller $M(K\pi)$ values, the background shapes exhibit an exponential enhancement due to contributions from other D^0 decay modes and other D mesons. Therefore the background shape in the fit was described by the form $[A + B \cdot M(K\pi)]$ for $M(K\pi) > 1.86\,\mathrm{GeV}$ and $[A + B \cdot M(K\pi)] \cdot \exp\{C \cdot$

$[M(K\pi) - 1.86]\}$ for $M(K\pi) < 1.86\,\mathrm{GeV}$. The free parameters A, B and C were assumed to be independent for the two $M(K\pi)$ distributions. The numbers of D^0 mesons yielded by the fit were $N^{\mathrm{untag}}(D^0) = 7996 \pm 488$ and $N^{\mathrm{tag}}(D^0) = 1970 \pm 78$ for selections without and with ΔM tag, respectively.

4.2 Reconstruction of additional D^{*+} mesons

The $D^{*+} \to D^0\pi_s^+$ events with $p_T(D^{*+}) > 3\,\mathrm{GeV}$ and $|\eta(D^{*+})| < 1.6$ can be considered as a sum of two subsamples: events with the D^0 having $p_T(D^0) > 3\,\mathrm{GeV}$ and $|\eta(D^0)| < 1.6$, and events with the D^0 outside of that kinematic range. The former sample is represented by D^0 mesons reconstructed with ΔM tag, as discussed in the previous section. The latter sample of "additional" D^{*+} mesons was obtained using the same $D^0 \to K^-\pi^+$ decay channel and an independent selection described below.

In each event, tracks with opposite charges and $p_T > 0.4\,\mathrm{GeV}$ were combined in pairs to form D^0 candidates. To calculate the pair invariant mass, $M(K\pi)$, kaon and pion masses were assumed in turn for each track. Only D^0 candidates which satisfy $1.80 < M(K\pi) < 1.92\,\mathrm{GeV}$ were kept. Moreover, the D^0 candidates were required to have either $p_T(D^0) < 3\,\mathrm{GeV}$ or $|\eta(D^0)| > 1.6$. Any additional track, with $p_T > 0.2\,\mathrm{GeV}$ and a charge opposite to that of the kaon track, was assigned the pion mass and combined with the D^0 candidate to form a D^{*+} candidate with invariant mass $M(K\pi\pi_s)$. Here again the p_T cut was raised to $0.25\,\mathrm{GeV}$ for the data subsample for which the low-momentum track reconstruction efficiency was smaller.

Figure 4.2 shows the ΔM distribution for the D^{*+} candidates after all cuts. A clear signal is seen at the nominal value of $M(D^{*+}) - M(D^0)$. The combinatorial background was estimated from the mass-difference distribution for wrong-charge combinations, in which both tracks forming the D^0 candidate have the same charge and the third track has the opposite charge. Details are given in Appendix C.

The number of reconstructed additional D^{*+} mesons was determined by subtracting the wrong-charge ΔM distribution after normalising it to the distribution of D^{*+} candidates with the appropriate charges in the range $0.150 < \Delta M < 0.170\,\mathrm{GeV}$. The subtraction, performed in the signal range $0.143 < \Delta M < 0.148\,\mathrm{GeV}$, yielded $N^{\mathrm{add}}(D^{*+}) = 317 \pm 26$.

The ΔM distribution was also fitted to a sum of the modified Gaussian function describing the signal and a threshold function describing the non-resonant background. The threshold function had a form $A \cdot (\Delta M - m_\pi)^B$, where m_π is the pion mass [65] and A and B were free parameters. The results obtained using the fit instead of the subtraction procedure were used to estimate the systematic uncertainty of the signal extraction procedure.

4.3 Reconstruction of D^+ mesons

The D^+ mesons were reconstructed from the decay $D^+ \to K^-\pi^+\pi^+$. The analysis for this meson was done using the e^+p data sample only, where the dedicated D^+ trigger was implemented. In each event, two tracks with the same charges and $p_T > 0.5\,\text{GeV}$ and a third track with opposite charge and $p_T > 0.7\,\text{GeV}$ were combined to form D^+ candidates. The pion masses were assigned to the two tracks with the same charges and the kaon mass was assigned to the third track, after which the candidate invariant mass, $M(K\pi\pi)$, was calculated. To suppress the combinatorial background, a cut of $\cos\theta^*(K) > -0.75$ was imposed, where $\theta^*(K)$ is the angle between the kaon in the $K\pi\pi$ rest frame and the $K\pi\pi$ line of flight in the laboratory frame. To suppress background from D^{*+} decays, combinations with $M(K\pi\pi) - M(K\pi) < 0.15\,\text{GeV}$ were removed. The background from $D_s^+ \to \phi\pi^+$ with $\phi \to K^+K^-$ was suppressed by requiring that the invariant mass of any two D^+ candidate tracks with opposite charges was not within $\pm 8\,\text{MeV}$ of the ϕ mass [65] when the kaon mass was assigned to both tracks.

Figure 4.3 shows the $M(K\pi\pi)$ distribution for the D^+ candidates after all cuts. A clear signal is seen at the nominal value of D^+ mass. The mass distribution was fitted to a sum of a modified Gaussian function describing the signal and a linear function describing the non-resonant background. The number of reconstructed D^+ mesons yielded by the fit was $N(D^+) = 4785 \pm 501$.

4.4 Reconstruction of D_s^+ mesons

The D_s^+ mesons were reconstructed from the decay $D_s^+ \to \phi\pi^+$ with $\phi \to K^+K^-$. In each event, tracks with opposite charges and $p_T > 0.7\,\text{GeV}$ were assigned the kaon mass and combined in pairs to form ϕ candidates. The ϕ candidate was kept if its invariant mass, $M(KK)$, was within $\pm 8\,\text{MeV}$ of the ϕ mass [65]. Any additional track with $p_T > 0.5\,\text{GeV}$ was assigned the pion mass and combined with the ϕ candidate to form a D_s^+ candidate with invariant mass $M(KK\pi)$. To suppress the combinatorial background, the following requirements were applied:

- $\cos\theta^*(\pi) < 0.85$, where $\theta^*(\pi)$ is the angle between the pion in the $KK\pi$ rest frame and the $KK\pi$ line of flight in the laboratory frame;
- $|\cos^3\theta'(K)| > 0.1$, where $\theta'(K)$ is the angle between one of the kaons and the pion in the KK rest frame. The decay of the pseudoscalar D_s^+ meson to the ϕ (vector) plus π^+ (pseudoscalar) final state results in an alignment of the spin of the ϕ meson with respect to the direction of motion of the ϕ relative to D_s^+. Consequently, the distribution of $\cos\theta'(K)$ follows a $\cos^2\theta'(K)$ shape, implying

a flat distribution for $\cos^3\theta'(K)$. In contrast, the $\cos\theta'(K)$ distribution of the combinatorial background is flat and its $\cos^3\theta'(K)$ distribution peaks at zero. The cut suppressed the background significantly while reducing the signal by 10%.

Figure 4.4 shows the $M(KK\pi)$ distribution for the D_s^+ candidates after all cuts. A clear signal is seen at the nominal D_s^+ mass. There is also a smaller signal around the nominal D^+ mass as expected from the decay $D^+ \to \phi\pi^+$ with $\phi \to K^+K^-$. The mass distribution was fitted to a sum of two modified Gaussian functions describing the signals and an exponential function describing the non-resonant background. To reduce the number of free parameters, the width of the D^+ signal was constrained to be the same that of the D_s^+ signal width. The number of reconstructed D_s^+ mesons yielded by the fit was $N(D_s^+) = 647 \pm 80$, for $p_T(D_s^+) > 3$ GeV and $N(D_s^+) = 773 \pm 96$, for $p_T(D_s^+) > 2$ GeV.

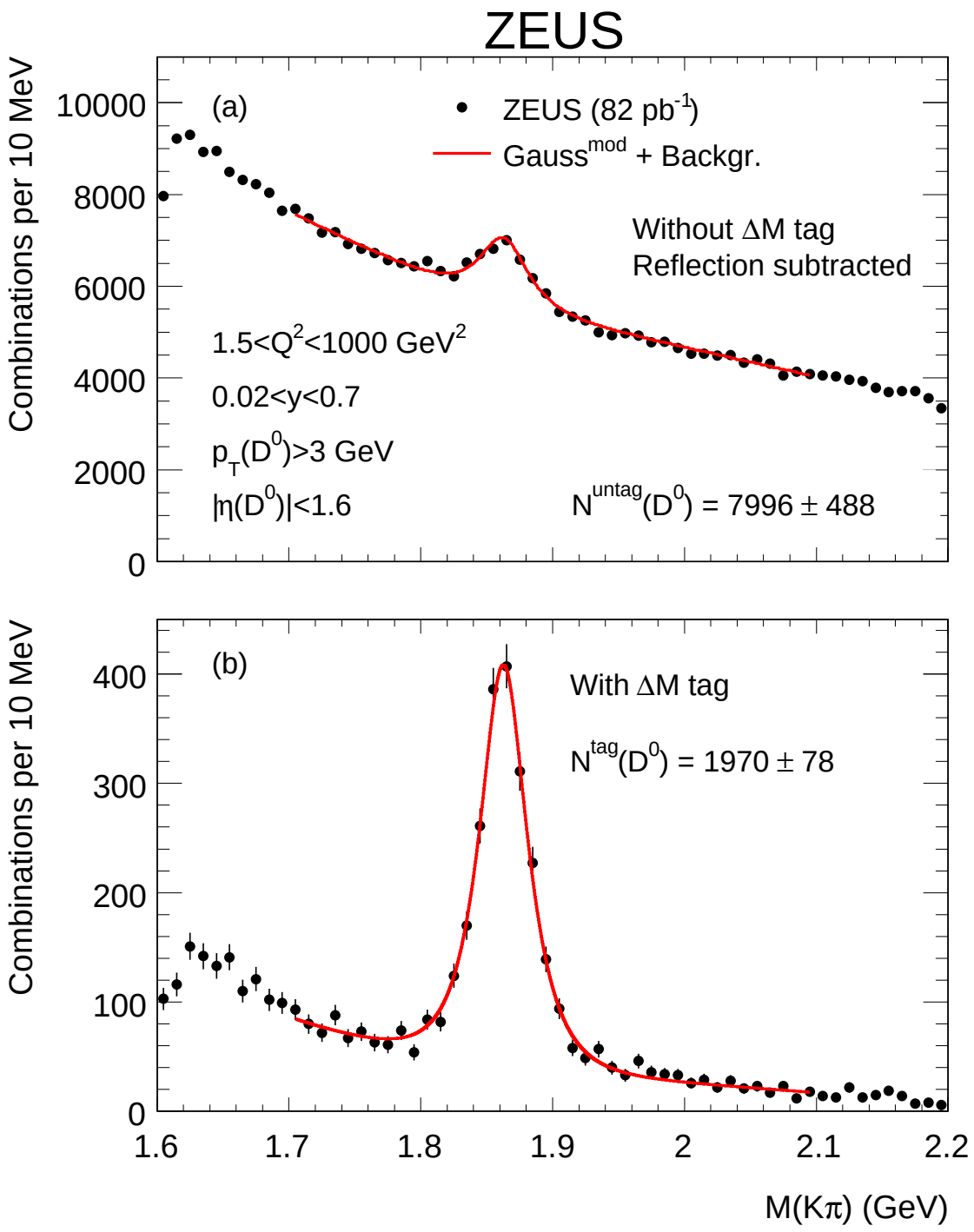

Figure 4.1: The $M(K^-\pi^+)$ distributions (dots) for (a) the D^0 candidates without ΔM tag, obtained after reflection subtraction, and for (b) the D^0 candidates with ΔM tag. The first and last bins are affected by the trigger selection. The solid curves represent a fit to the sum of a modified Gaussian function and a background function.

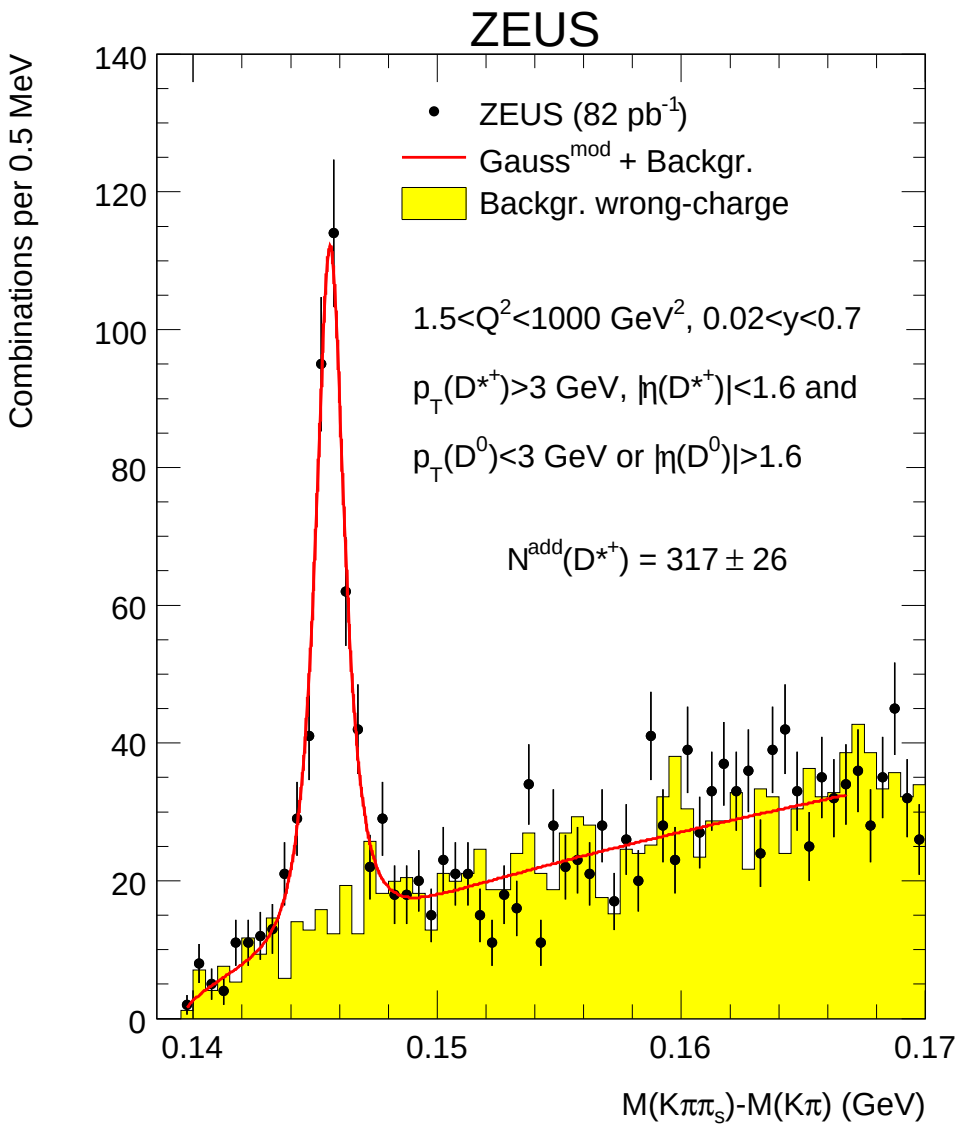

Figure 4.2: The distribution of the mass difference, $\Delta M = M(K^-\pi^+\pi_s^+) - M(K^-\pi^+)$, for the "additional" D^{*+} candidates (dots). The histogram shows the ΔM distribution for wrong-charge combinations. For illustration, the solid curve represents a fit to the sum of a modified Gaussian function and a background function.

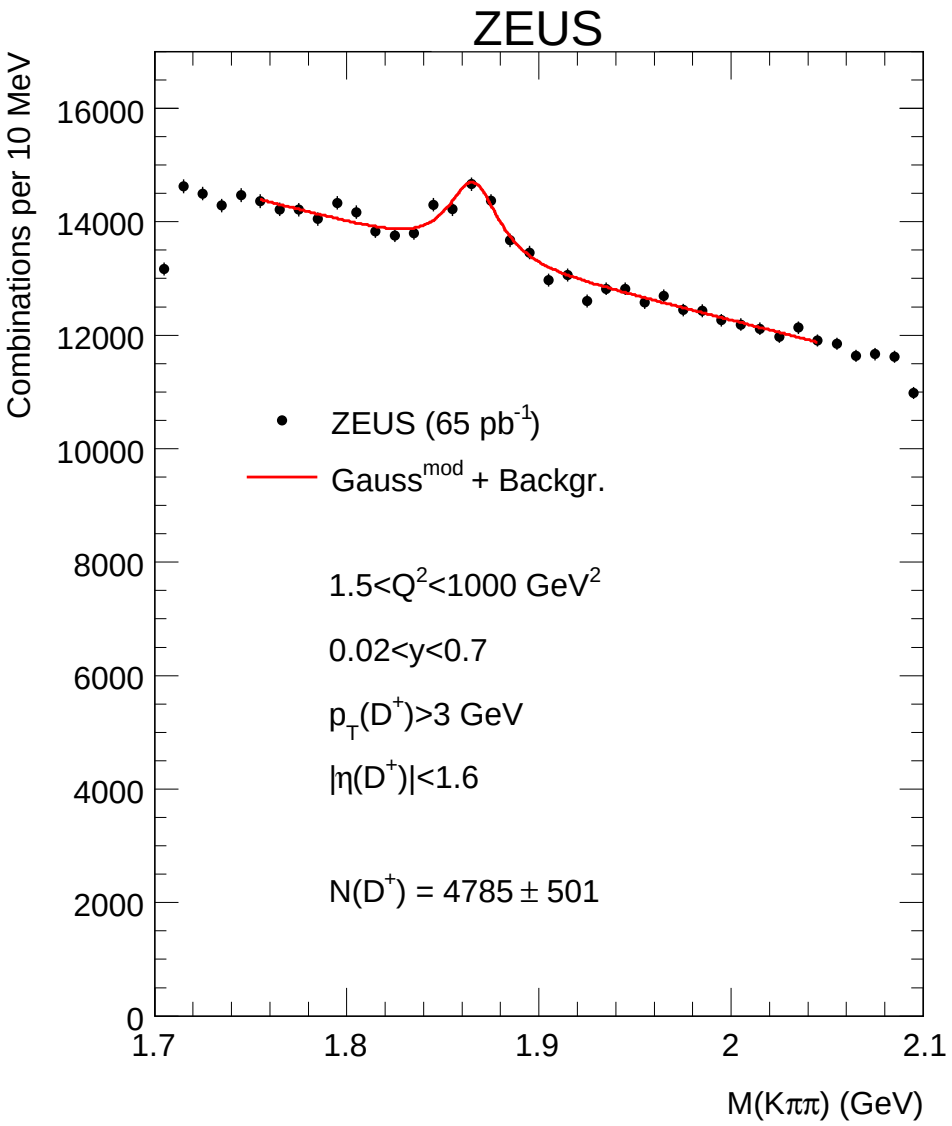

Figure 4.3: The $M(K^-\pi^+\pi^+)$ distribution for the D^+ candidates (dots). The first and last bins are affected by the trigger selection. The solid curve represents a fit to the sum of a modified Gaussian function and a linear background function.

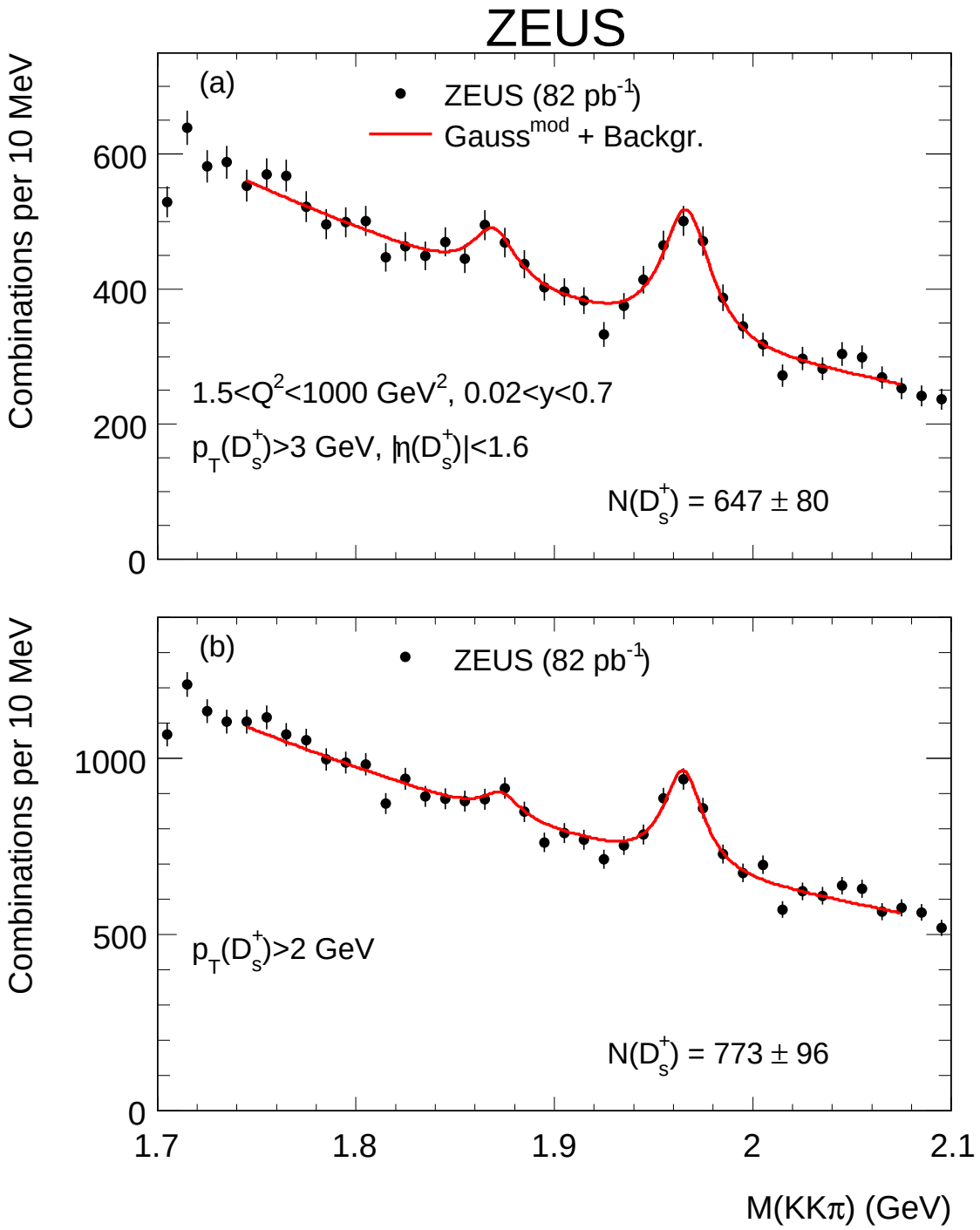

Figure 4.4: The $M(K^+K^-\pi^+)$ distribution for (a) D_s^+ candidates with $p_T(D_s^+) > 3$ GeV and (b) D_s^+ candidates with $p_T(D_s^+) > 2$ GeV. The first bins are affected by the trigger selection. The solid curves represent fits to the sum of two modified Gaussian functions and an exponential background function. The first peak in both distributions is from D^+ decaying through the same channel.

Chapter 5

Charm-meson Production Cross Sections

In this chapter we describe the simulations used to correct our data. Corrections include reconstruction efficiencies due to detector effects, QED electromagnetic radiation and contamination from beauty production. Charm-meson cross sections are then measured using the reconstructed signals for the process $ep \to eDX$ presented in Chapter 4 in the kinematic region $1.5 < Q^2 < 1000\,\mathrm{GeV}^2$, $0.02 < y < 0.7$, $p_T(D) > 3\,\mathrm{GeV}$ (for the D_s^+ also $p_T(D_s^+) > 2\,\mathrm{GeV}$) and $|\eta(D)| < 1.6$.

5.1 Event and detector simulation

5.1.1 The role of the simulations

All measurements are always affected by detector effects. In order to extract the physical observables which can be compared to the theoretical predictions, one has to correct for these detector-related effects. This is usually done using Monte Carlo methods. Monte Carlo methods are an essential tool in experimental high energy physics. They are used to simulate complete events. Simulation splits in two differents parts: *physisc simulation* and *detector simulation*. The generated events (MC events) are used to correct the data by detector effects (efficiency in the reconstruction, migrations, etc.). This can be done under the condition that the simulated final-state quatities agree well with those measured with the detector.

The physics simulation of ep interactions at HERA is divided into several separated steps:

- Hard Scattering: the SM is used to calculate the matrix elements of the hard scattering at leading or higher orders.

- Parton Showering: simulation of the initial and final state QCD radiation.
- Hadronization: partons fragment into color-neutral hadrons. This process is essentially non-perturbative and various models are used for its implementation.

The output of the physics simulation is a list containing the four-vectors of all particles generated in the event, which are then passed through a full simulation of the detector. The detector simulation is based on the GEANT 3.13 package [55]. A detailed simulation of the geometry and materials of the detector is performed at this stage. In addition, the three-level trigger is simulated. The full GEANT simulation of the ZEUS detector uses the program MOZART (Monte Carlo for Zeus Analysis, Reconstruction and Trigger). For every particle in the final state, MOZART simulates its interaction with the detector material, its possible decays, the signals produced in the different components (tracking, calorimeter...) and the digitization of the signal, including the various sources of noise. Finally, the information from the detector and the trigger simulation of the events is written to tape in an identical format as the real data. This allows to pass the Monte Carlo events through the same reconstruction chain and selection as used for the data.

The state after the parton showering is called *parton level*, the one after the hadronization *hadron level* and the final one *detector level*.

5.1.2 Monte Carlo models

In this analysis, the RAPGAP 2.08 [66] MC model is used as the nominal Monte Carlo to correct the data, and HERWIG 6.3 [67] is used for systematic studies. The RAPGAP MC model was interfaced with HERACLES 4.6.1 [68], which simulates the ep-DIS process, including first-order electroweak corrections.

The MC models were used to produce charm and beauty by the direct and the resolved photon processes. The CTEQ5L [69] and GRV-LO [70] PDFs were used for the proton and the photon, respectively. The charm and beauty quark-masses were set to 1.5 GeV and 4.75 GeV, respectively. Both the RAPGAP and HERWIG MCs use LO matrix elements with leading-logarithmic parton showers in the initial and final state to simulate higher-order processes. Charm fragmentation is implemented using either the Lund string fragmentation [71], as implemented in JETSET [72] (in RAPGAP) or a cluster fragmentation [73] model (in HERWIG).

5.1.3 Monte Carlo sample

RAPGAP MC events were generated with $Q^2 > 0.6$ GeV^2 and at least one of the

following charm hadrons decaying in the specific channel used for the reconstruction:

$$
\begin{aligned}
D^{*+} &\to D^0(\to K^-\pi^+)\pi_s^+ && \text{with } p_T(D^{*+}) > 1.25 \text{ GeV} \\
D^{*+} &\to D^0(\to K_s^0\pi^+\pi^-)\pi_s^+ && \text{with } p_T(D^{*+}) > 1.35 \text{ GeV} \\
D^{*+} &\to D^0(\to K^-\pi^+\pi^+\pi^-)\pi_s^+ && \text{with } p_T(D^{*+}) > 2.3 \text{ GeV} \\
D^0 &\to K^-\pi^+ && \text{with } p_T(D^0) > 2.6 \text{ GeV} \\
D_s^+ &\to \phi(\to K^+K^-)\pi^+ && \text{with } p_T(D_s^+) > 1.7 \text{ GeV} \\
D^+ &\to \phi(\to K^+K^-)\pi^+ && \text{with } p_T(D^+) > 1.7 \text{ GeV} \\
D^+ &\to K^-\pi^+\pi^+ && \text{with } p_T(D^+) > 2.8 \text{ GeV} \\
\Lambda_c^+ &\to K^-p\pi^+ && \text{with } p_T(\Lambda_c^+) > 2.8 \text{ GeV} .
\end{aligned}
$$

All cuts used in this analysis as well as the kinematic region of the measurement are compatible with the phase space available in the Monte Carlo. The luminosity of the MC sample, $\mathcal{L}_{MC} = 421\,\text{pb}^{-1}$ is of the order of 5.1 times the luminosity of the data sample, in order to make the statistical uncertainty of the MC simulation negligible with respect that of the data.

5.1.4 Description of data by the simulation

The kinematic variables of the selected events were compared with the simulation. All distributions have the combinatorial background subtracted, i.e. the comparison is the number of reconstructed D mesons from the fit in bins of each distribution. Figures 5.1, 5.4 and 5.5 compare the distribution of the kinematic variables Q^2, x, $p_T(D)$ and $\eta(D)$ for events containing "untagged" D^0, D^+ and D_s^+ mesons, respectively, between data and MC at detector level. The comparison shows that RAPGAP describes the data in a reasonable way. However, the convergence of the fits may be spoilt in some particular bins due to a number of reasons, i.e. the use of the same function to describe the bakcground in both data and MC, large fluctuations of the background or a small ratio signal to background in the data, leading to the observation of large discrepancies between data and MC in those bins. As a cross check, and to show that no reweighting of the MC was needed, two more, independent, sets of control plots were made for the "untagged" D^0 mesons. Figure 5.2 shows the comparison of the kinematic variables Q^2 and x for events containg untagged D^0 mesons, after subtracting the background. In the first bin of the Q^2 histogram, the width of the corresponding "untag" $M(K^-, \pi^+)$ distribution in the data was fixed to the width of the corresponding MC distribution. In the first bin of the x histogram, the width of the corresponding "untag" $M(K^-, \pi^+)$ distribution in the data was fixed to the with of the corresponding data "tag" distribution. The agreement between data and MC in these bins is better than in the nominal case (Figure 5.1).

Additionally, Figure 5.3 shows again the comparison data/MC for the kinematic variables Q^2, x, $p_T(D^0)$ and $\eta(D^0)$ for events containg "untagged" D^0 mesons, but in which the number of reconstructed D^0 in each bin (data and MC) was extracted following a method ("side bands") involving no fits at all. In the corresponding mass distribution to each bin, a signal region and two adjacents side bands regions were defined. The signal region contains both signal and background events, whereas the side bands regions contain only background. To estimate the number of D^0 mesons in the signal region, the background was subtracted according to the following procedure: candidates reconstructed inside the signal region were counted with a weight $+1$, whereas candidates reconstructed in the side bands regions were counted with weight -1. Even if the method can not be considered as accurate as the fit in order to extract the number of reconstructed mesons, it is enough to show that the MC simulation describes the data adecuately, and, moreover, it is free of convergence problems.

5.1.5 Reconstruction acceptance calculation

As mentioned, detector effects were corrected using the MC simulation. Correction factors were calculated for all particles and for all regions of the phase space in which a cross section is measured, that is, the whole kinematic region for the total cross sections and the bins of each distribution for the differential cross sections. The correction factor, or *acceptance*, for a D-meson reconstructed via the generic decay channel $D \to P_1 P_2 \cdots P_n$ in the kinematic region M of the phase space is defined as

$$A(M) = \frac{\text{reconstructed } D \text{ mesons in the region } M \text{ after all cuts (in MC)}}{\text{generated } D \to P_1 P_2 \cdots P_n \text{ in the region } M \text{ (in MC)}} \; .$$

The kinematic region M is defined in terms of the reconstructed variables in the numerator and in terms of the generated variables in the denominator. For the reconstruction acceptance calculation associated to detector effects the kinematic variables at the generated level in the MC were calculated from the virtual photon vertex rather than from the difference of the 4-momenta between the incoming and outgoing lepton. The reconstruction acceptances were calculated with RAPGAP and vary depending on the particle and the kinematic region of the measurement. For $1.5 < Q^2 < 1000$ GeV^2, $0.02 < y < 0.7$, transverse momenta $p_T(D^0, D^+) > 3\,\text{GeV}$, $p_T(D_s^+) > 2\,\text{GeV}$ and pseudorapidity $|\eta(D)| < 1.6$ the overall acceptances were $\approx 42\%$, $\approx 26\%$ and $\approx 17\%$ for D^0, D^+, and D_s^+ mesons, respectively. Figures 5.6, 5.7 and 5.8 show the reconstruction acceptances in bins of Q^2, x, $p_T(D)$ and $\eta(D)$ for the D^0, D^+ and D_s^+ mesons. The corrections decrease with $p_T(D)$ as the daughter tracks are more boosted and have less chances to scape from the CTD acceptance. They are large in the low Q^2 regime due to the decrease of the calorimeter acceptance

near the rear beam pipe hole.

5.1.6 Experimental measurement of a cross section

Reconstruction acceptances are used to correct the data in order to measure *cross sections*. The cross section corresponding to the production of the meson D in the kinematic region M of the phase space is measured as

$$\sigma(D, M) = \frac{N(D)}{A(M) \cdot \mathcal{L} \cdot \mathcal{B}} \ ,$$

where $N(D)$ is the number of reconstructed D-mesons in the data in the region M, $A(M)$ is the acceptance in the region M calculated with MC, $\mathcal{L}$ is the luminosity corresponding to the data sample used for the measurement and $\mathcal{B}$ is the branching ratio (or product of branching ratios) for the decay channel used in the reconstruction of the meson D.

It is usual to slice the phase space in bins of a general observable X to define the kinematic regions ΔX_i:

$$M \rightarrow \Delta X_i = \{X \mid X_i < X < X_{i+1}\} \ ,$$

where X_i and X_{i+1} are the lower and upper bounds which define the i-bin. The integrated cross section in each bin is then usually divided by the bin width ΔX_i as an approximation to the D-meson *differential* production cross section in the variable X:

$$\frac{d\sigma(D)}{dX} \sim \frac{\sigma(D, \Delta X_i)}{\Delta X_i} \ .$$

Higher-dimensional differential cross sections are measured in a similar way.

5.1.7 QED radiative corrections

The MC sample used for the acceptance correction factor incorporates first order electromagnetic effects, i.e. QED radiation in both the initial and final state. Measured cross section using this factors are therefore corrected at the QED "radiative" level. For consistent comparisons with theoretical predictions it is desireable to bring them to the "Born" level. For this purpose, two independent MC samples containing generated-level events were used: one without radiative correction (Born) and one with radiative corrections (RC). Then, the following relation was assume in order to bring the measured cross sections to the Born level:

$$\sigma(D, M)^{\mathrm{RC}}_{\mathrm{DATA}} \rightarrow \sigma(D, M)^{\mathrm{Born}}_{\mathrm{DATA}} = \sigma(D, M)^{\mathrm{RC}}_{\mathrm{DATA}} \cdot \beta(D, M) \ ,$$

with the factor $\beta(D, M)$ given by

$$\beta(D, M) = \frac{\sigma(D, M)^{\text{Born}}_{\text{MC}}}{\sigma(D, M)^{\text{RC}}_{\text{MC}}} \ .$$

The Born and radiative MC cross sections are determined by taking the ratio between the number of D-mesons found in the kinematic region M and the corresponding luminosities of both MC samples:

$$\sigma(D, M)^{\text{Born}}_{\text{MC}} = \frac{N(D, M)^{\text{Born}}_{\text{MC}}}{\mathcal{L}^{\text{Born}}_{\text{MC}}}$$
$$\sigma(D, M)^{\text{RC}}_{\text{MC}} = \frac{N(D, M)^{\text{RC}}_{\text{MC}}}{\mathcal{L}^{\text{RC}}_{\text{MC}}} \ .$$

β-correction factors were calculated independently for the D^0, D^+ and D_s^+ mesons in the whole kinematic region of the measurement for the total cross sections and in bins of each distributions for the differential cross sections. However, due to statistical reasons, β factors calculated with D^0, D^+ and D_s^+ mesons events all together were used to correct the measured cross sections and bring them to the Born level. Figure 5.9 show the values of the β-factors for $p_T(D) > 3.0\,\text{GeV}$ in bins of each distribution. Typical corrections due to QED radiation are found to be of the order of 1-2%.

5.1.8 Contamination from beauty production

The relative b-quark contributions, predicted by the MC simulation using branching ratios of b-quark decays to the charmed hadrons measured at LEP [74, 75], were subtracted from all measured cross sections. The subtraction of the b-quark contribution reduced the measured cross sections by 3.1% for the D^0 and D^+ and 4.3% for the D_s^+ and changed the measured charm fragmentation ratios and fractions by less than 1%.

5.2 Charm-meson production cross sections

Charm-meson cross sections were measured using the reconstructed signals for the process $ep \to eDX$ in the kinematic region $1.5 < Q^2 < 1000\,\text{GeV}^2$, $0.02 < y < 0.7$, $p_T(D) > 3\,\text{GeV}$ (for the D_s^+ also $p_T(D_s^+) > 2\,\text{GeV}$) and $|\eta(D)| < 1.6$.

The systematic uncertainties presented in this and the following chapters will be discussed in Chapter 8. The third set of uncertainties quoted for the measured cross sections and charm fragmentation ratios and fractions are due to the propagation of the relevant branching-ratio uncertainties.

The following cross sections were measured:

- the production cross section for D^0 mesons not originating from the $D^{*+} \to D^0\pi_s^+$ decays, hereafter called untagged D^0 mesons, is:

$$\sigma^{\rm untag}(D^0) = 5.56 \pm 0.35({\rm stat.})^{+0.32}_{-0.26}({\rm syst.}) \pm 0.10({\rm br.})\,{\rm nb};$$

- the production cross section for D^0 mesons originating from the $D^{*+} \to D^0\pi_s^+$ decays:

$$\sigma^{\rm tag}(D^0) = 1.78 \pm 0.08({\rm stat.})^{+0.12}_{-0.10}({\rm syst.}) \pm 0.03({\rm br.})\,{\rm nb};$$

- the production cross section for all D^0 mesons:

$$\sigma_{\rm kin}(D^0) = \sigma^{\rm untag}(D^0) + \sigma^{\rm tag}(D^0) = 7.34 \pm 0.36({\rm stat.})^{+0.35}_{-0.27}({\rm syst.}) \pm 0.13({\rm br.})\ {\rm nb};$$

- the production cross section for additional D^{*+} mesons:

$$\sigma^{\rm add}(D^{*+}) = 0.518 \pm 0.046({\rm stat.})^{+0.051}_{-0.046}({\rm syst.}) \pm 0.01({\rm br.})\,{\rm nb}.$$

  The production cross section for D^{*+} mesons in the kinematic range $p_T(D^{*+}) > 3\,{\rm GeV}$ and $|\eta(D^{*+})| < 1.6$, $\sigma_{\rm kin}(D^{*+})$, is given by the sum

$$\sigma_{\rm kin}(D^{*+}) = \sigma^{\rm add}(D^{*+}) + \sigma^{\rm tag}(D^0)/\mathcal{B}(D^{*+} \to D^0\pi_s^+)\ .$$

  Using the measured cross sections, we get:

$$\sigma_{\rm kin}(D^{*+}) = 3.14 \pm 0.12({\rm stat.})^{+0.18}_{-0.15}({\rm syst.}) \pm 0.06({\rm br.})\,{\rm nb};$$

- the production cross section for D^+ mesons:

$$\sigma_{\rm kin}(D^+) = 2.80 \pm 0.30({\rm stat.})^{+0.18}_{-0.14}({\rm syst.}) \pm 0.10({\rm br.})\,{\rm nb};$$

- the production cross section for D_s^+ mesons with $p_T(D_s^+) > 3\,{\rm GeV}$:

$$\sigma_{\rm kin}(D_s^+) = 1.27 \pm 0.16({\rm stat.})^{+0.11}_{-0.06}({\rm syst.})^{+0.19}_{-0.15}({\rm br.})\,{\rm nb};$$

- the production cross section for D_s^+ mesons with $p_T(D_s^+) > 2\,\text{GeV}$:

$$\sigma_2(D_s^+) = 2.42 \pm 0.30(\text{stat.})^{+0.30}_{-0.14}(\text{syst.})^{+0.35}_{-0.27}(\text{br.})\ \text{nb}.$$

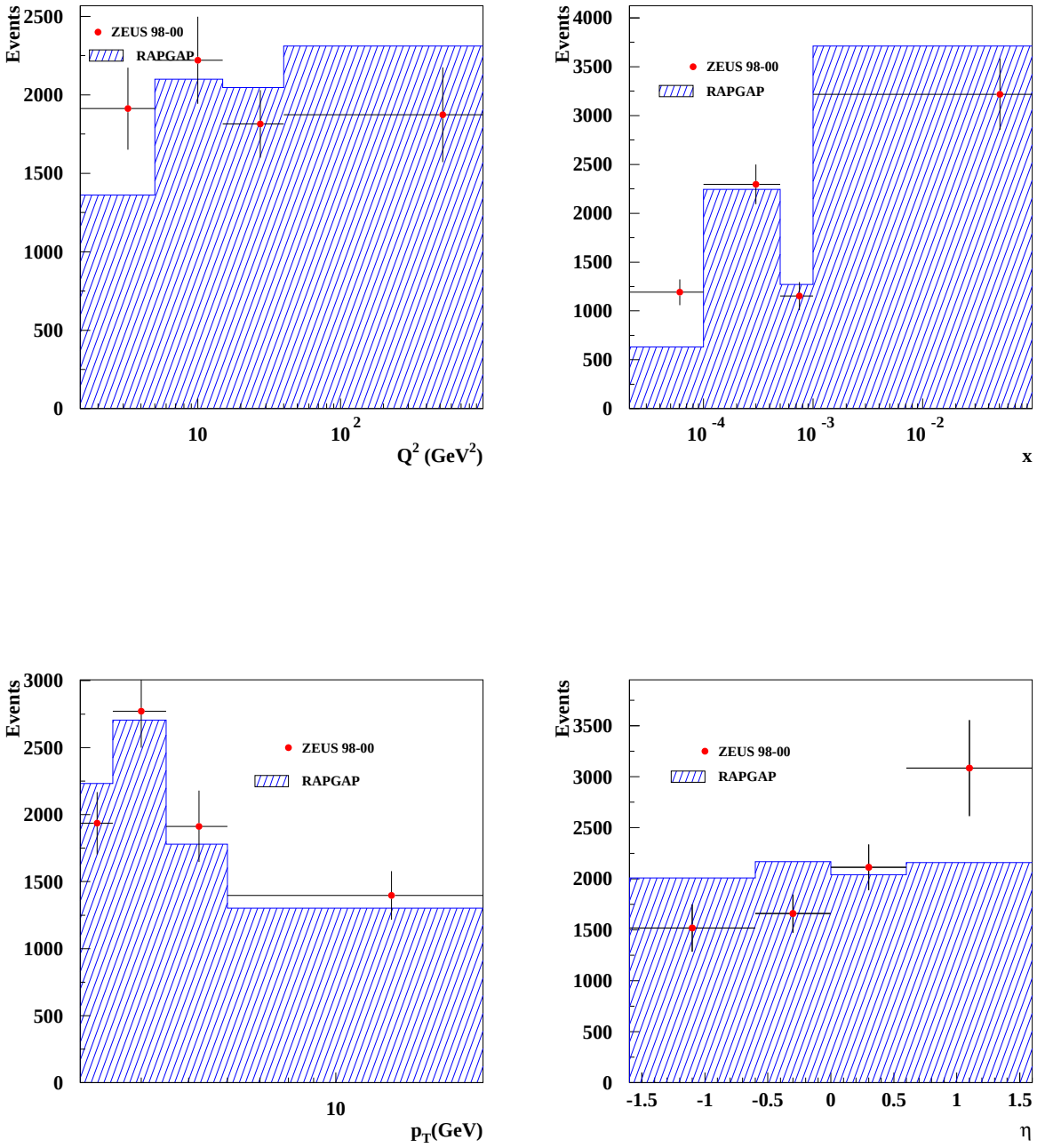

Figure 5.1: Comparison of the kinematic variables Q^2, x, $p_T(D^0)$ and $\eta(D^0)$ for events containing "untagged" D^0 between data and MC at detector level. The background has been subtracted. In each bin, the number of entries was obtained from a fit to the relevant mass distributions, both in data and MC.

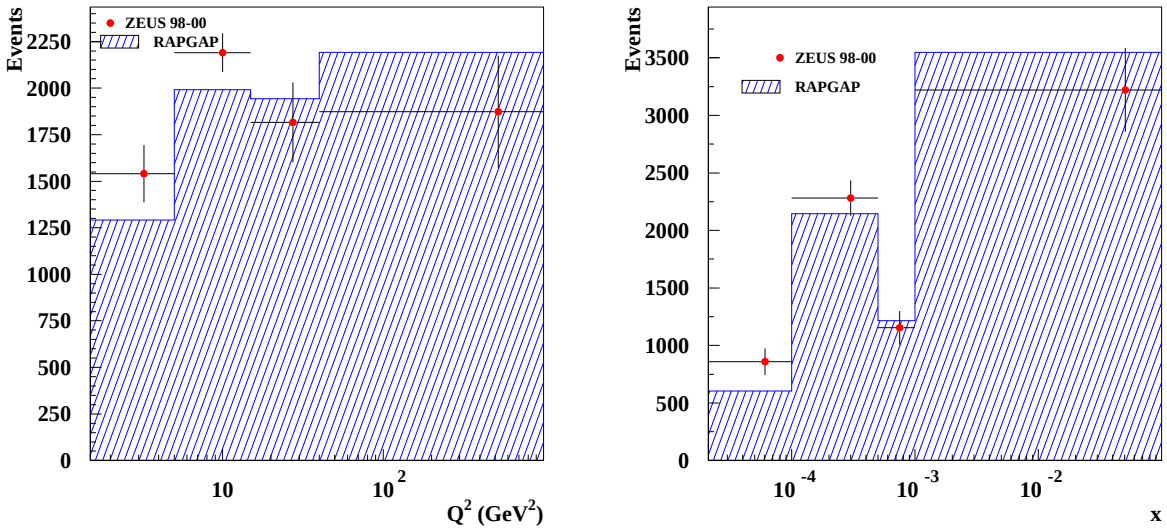

Figure 5.2: Comparison of the kinematic variables Q^2 and x for events containing "untagged" D^0 between data and MC at detector level. The background has been subtracted. In each bin, the number of entries wa obtained from a fit to the relevant mass distributions, both in data and MC. In the first bin of the Q^2 histogram, the width of the "untag" $M(K^-, \pi^+)$ distribution in the data was fixed to the width of the corresponding MC distribution. In the first bin of the x histogram, the width of the "untag" $M(K^-, \pi^+)$ distribution in the data was fixed to the with of the corresponding data "tag" distribution.

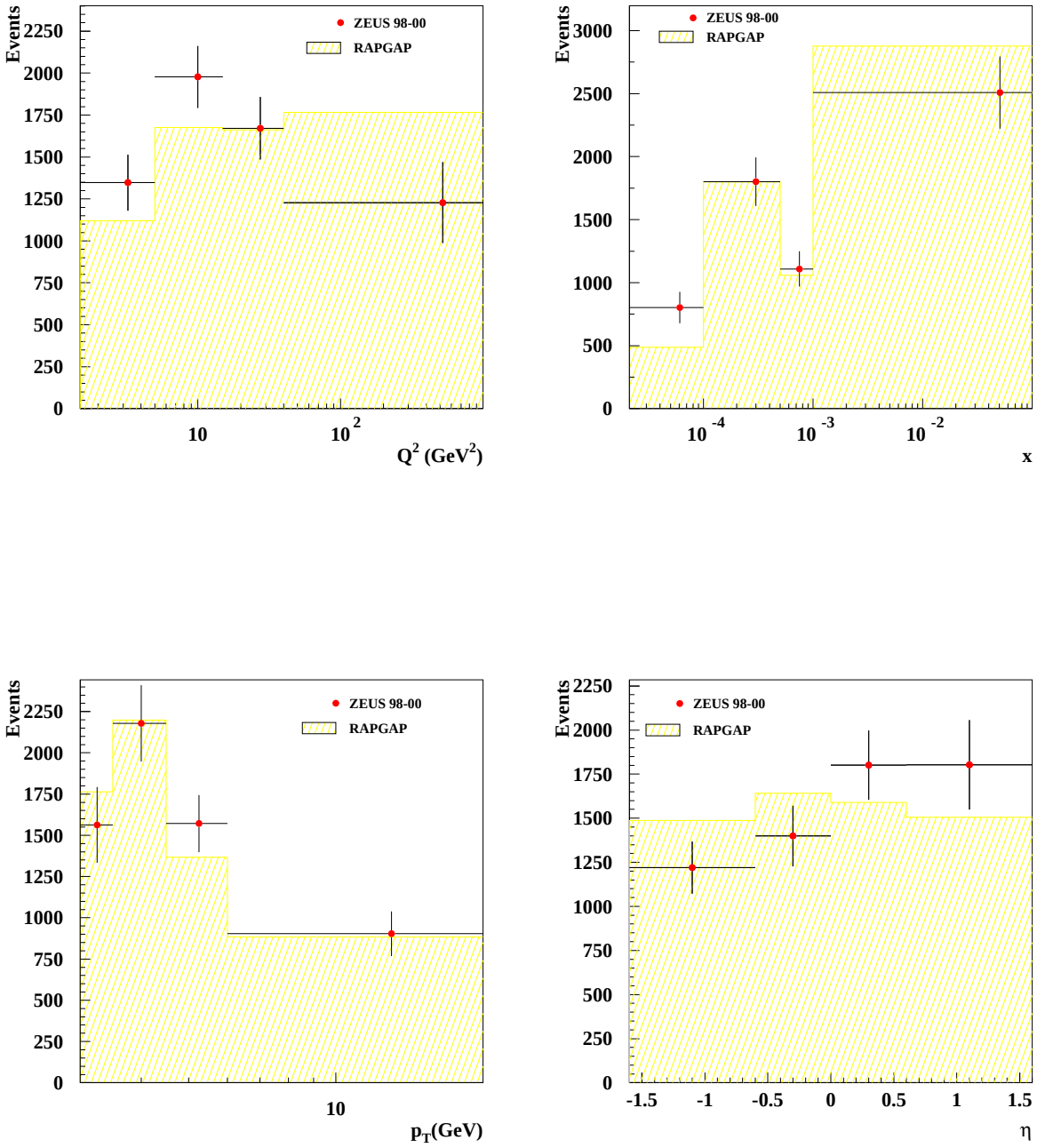

Figure 5.3: Comparison of the kinematic variables Q^2, x, $p_T(D^0)$ and $\eta(D^0)$ for events containing "untagged" D^0 between data and MC at detector level. The background has been subtracted. In each bin, the number of entries was obtained using the "side bands" method in the relevant mass distributions, both in data and MC. No fits were used.

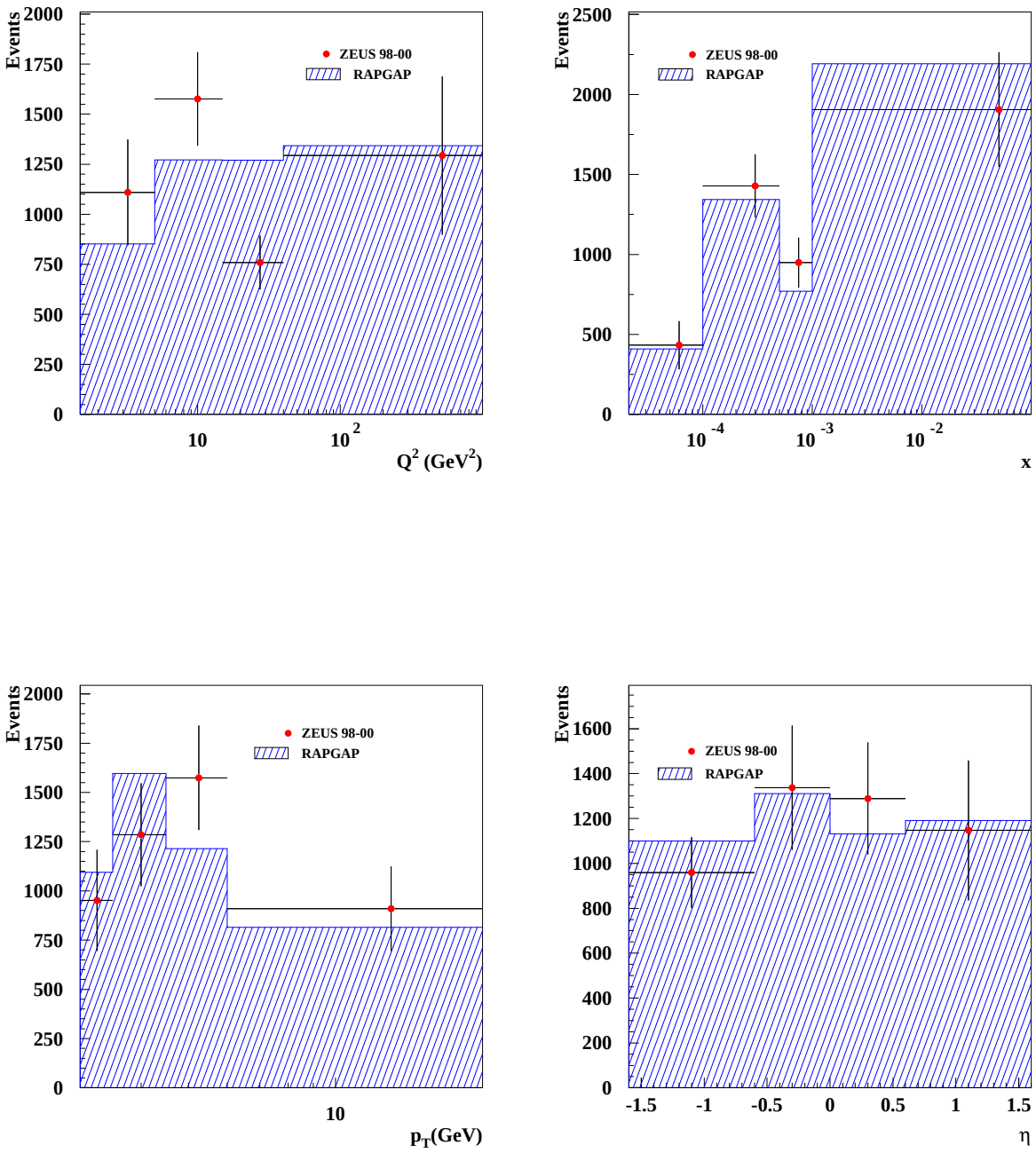

Figure 5.4: Comparison of the kinematic variables Q^2, x, $p_T(D^+)$ and $\eta(D^+)$ for events containing D^+ mesons between data and MC at detector level. The background has been subtracted. In each bin, the number of entries was obtained from a fit to the relevant mass distributions, both in data and MC.

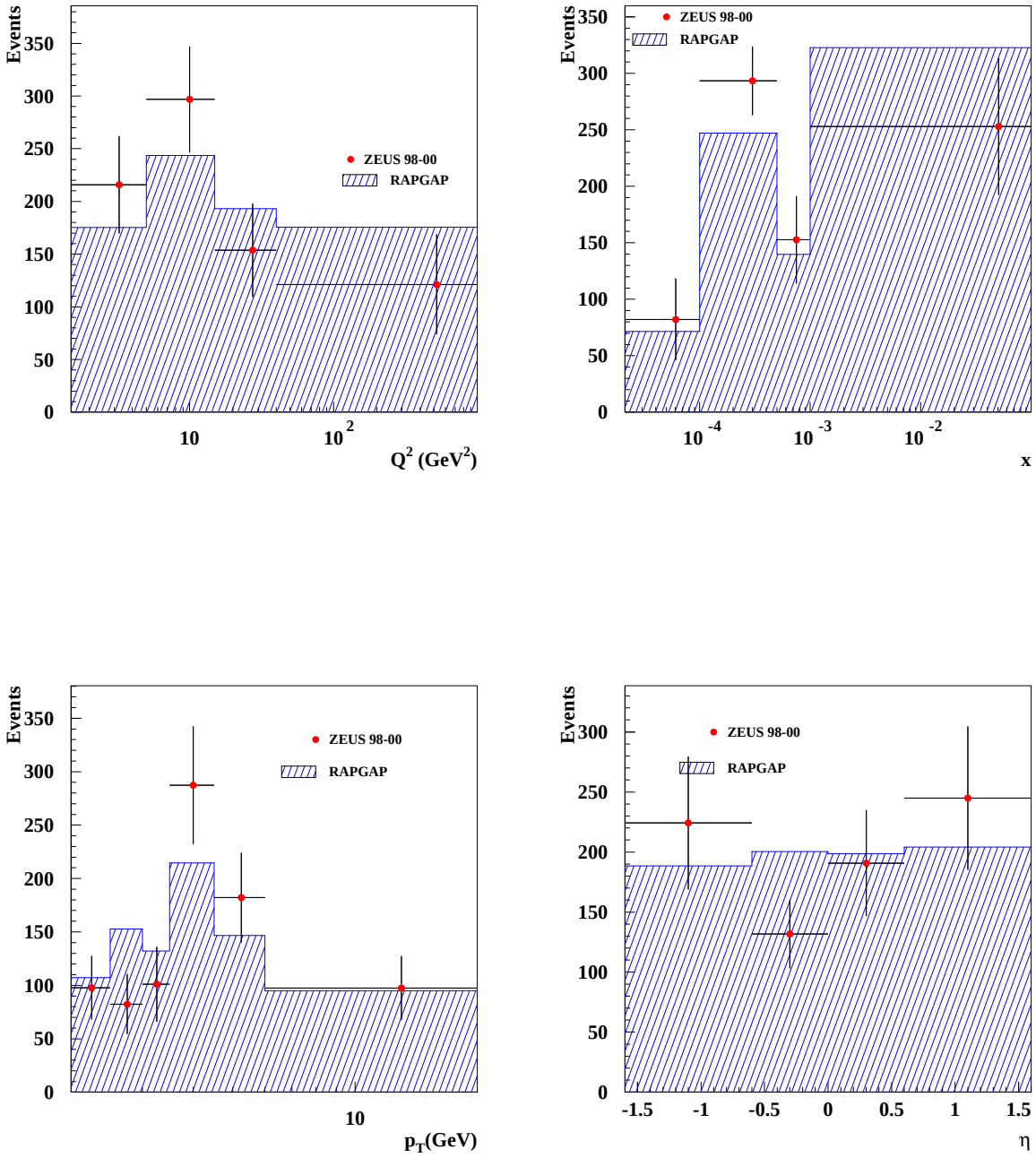

Figure 5.5: Comparison of the kinematic variables Q^2, x, $p_T(D_s^+)$ and $\eta(D_s^+)$ for events containing D_s^+ mesons between data and MC at detector level. The background has been subtracted. In each bin, the number of entries was obtained from a fit to the relevant mass distributions, both in data and MC.

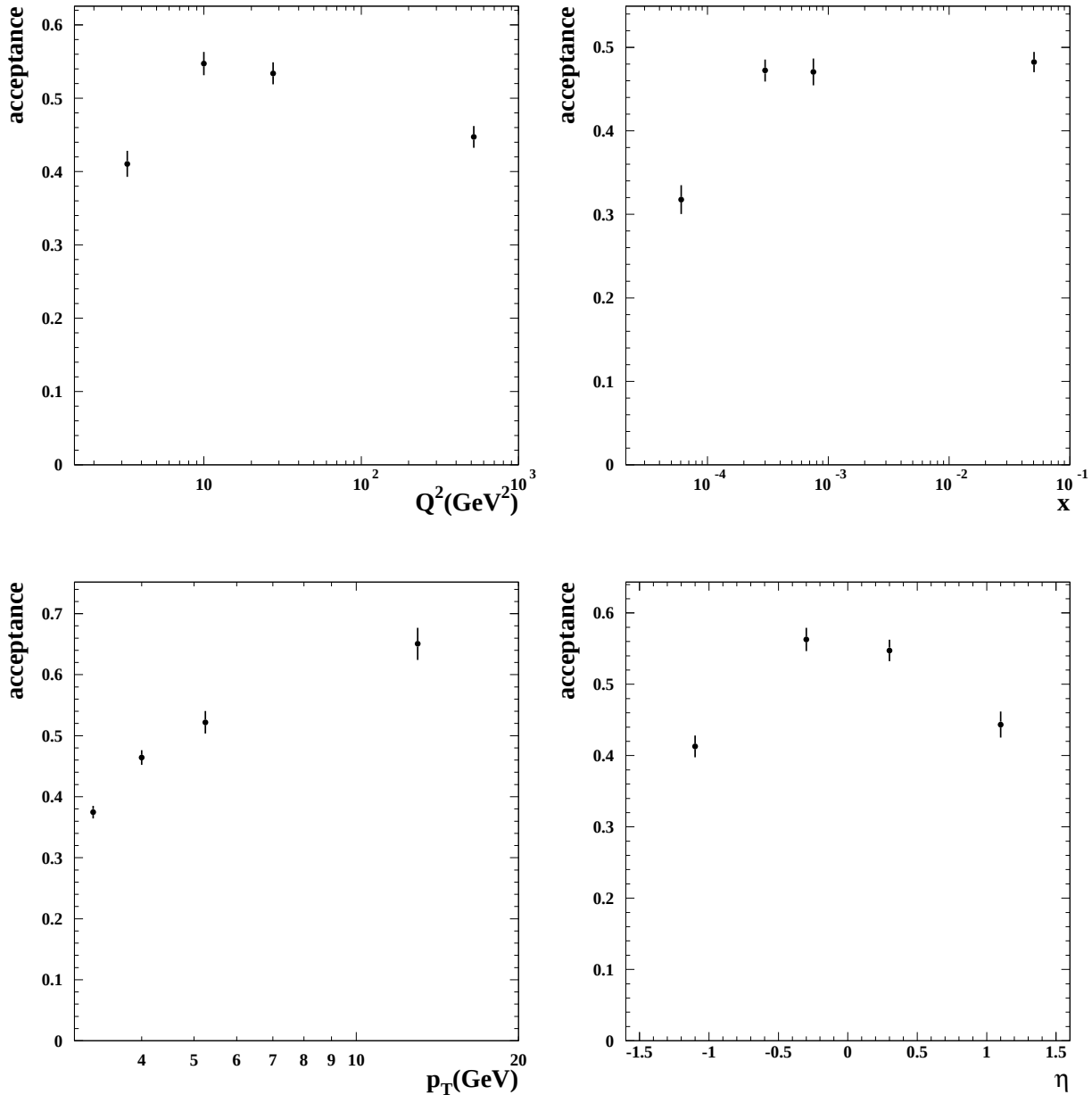

Figure 5.6: Reconstruction acceptances in bins of Q^2, x, $p_T(D^0)$ and $\eta(D^0)$ for "untagged" D^0 mesons calculated with RAPGAP.

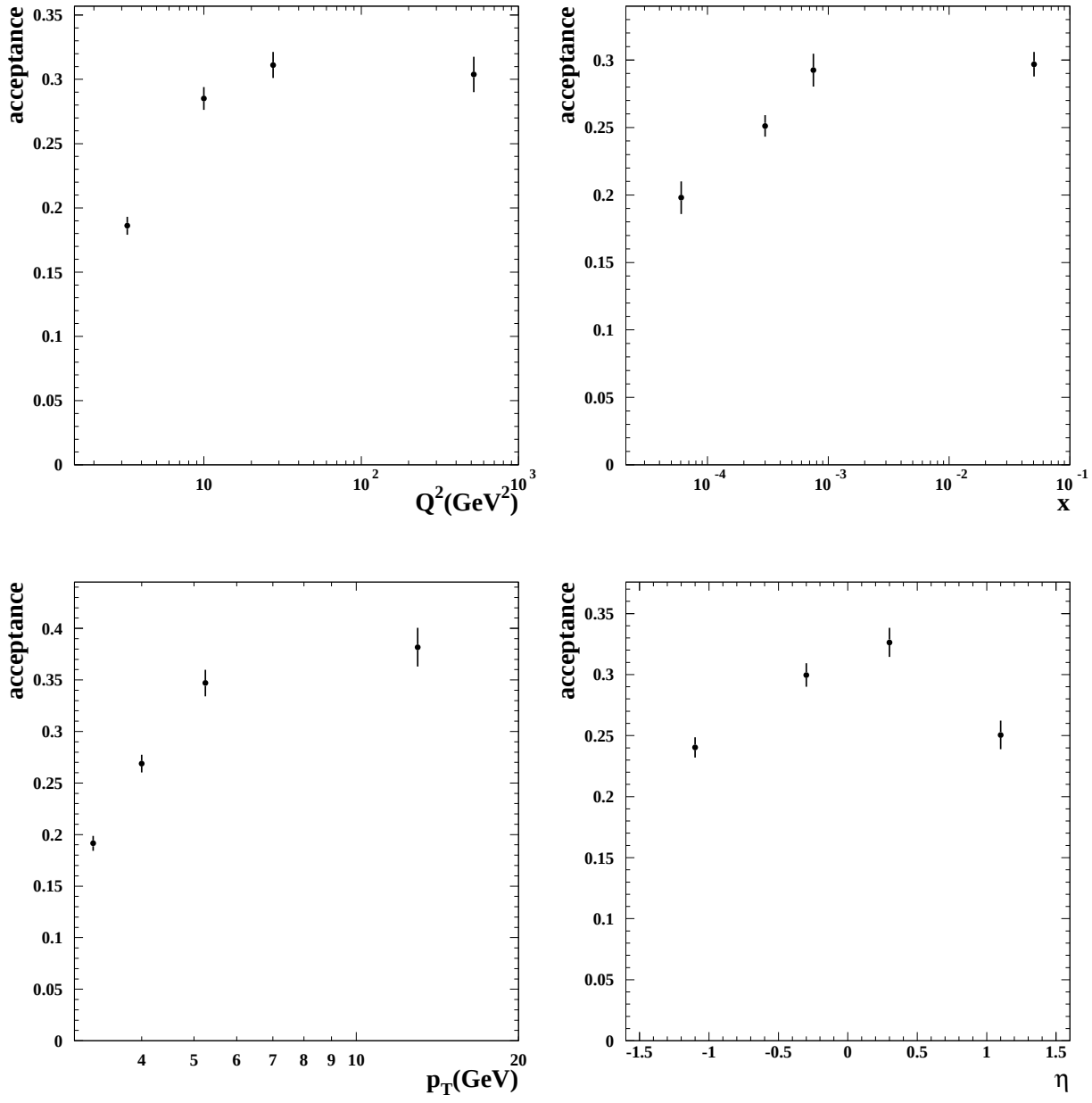

Figure 5.7: Reconstruction acceptances in bins of Q^2, x, $p_T(D^+)$ and $\eta(D^+)$ for D^+ mesons calculated with RAPGAP.

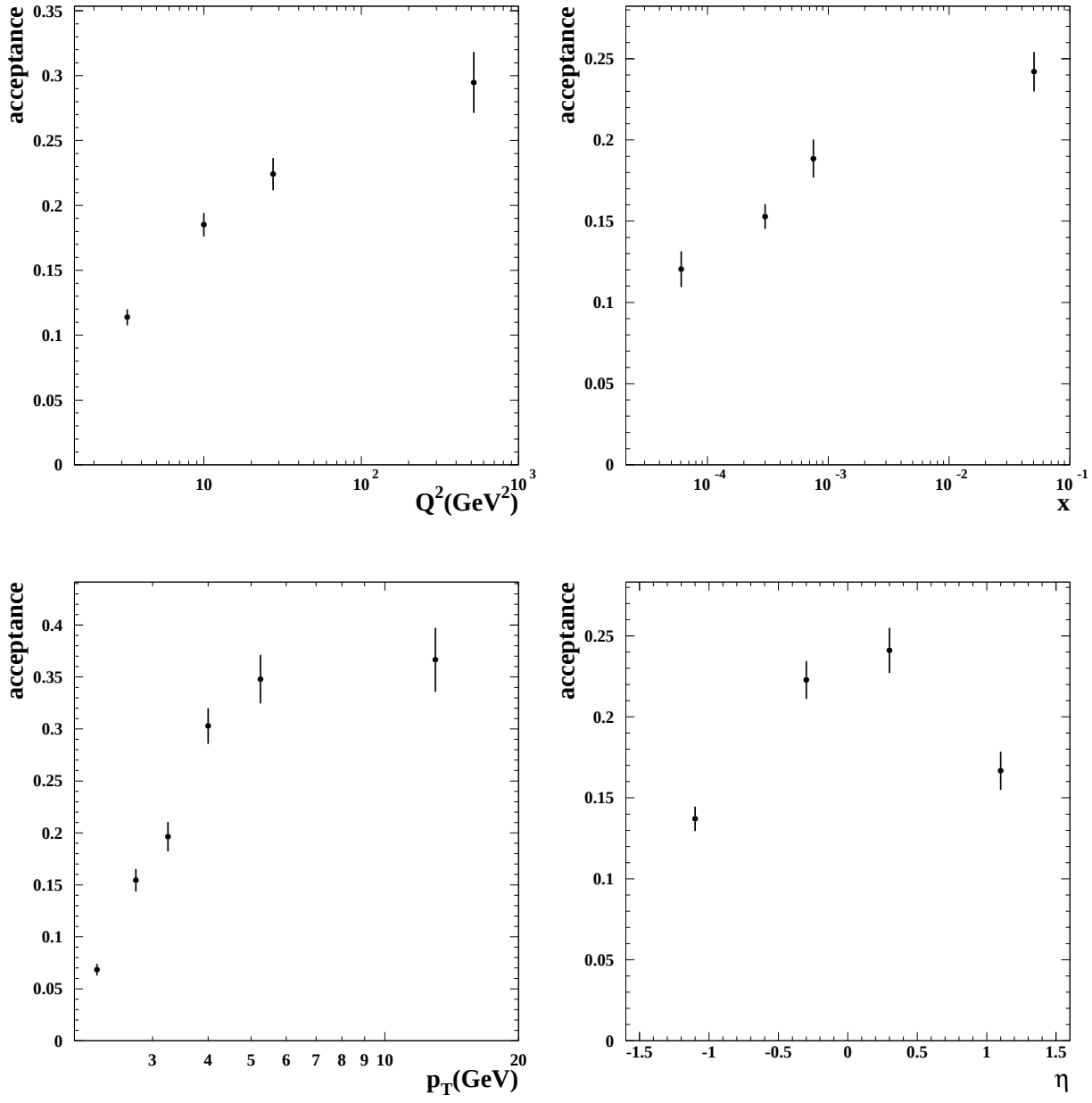

Figure 5.8: Reconstruction acceptances in bins of Q^2, x, $p_T(D_s^+)$ and $\eta(D_s^+)$ for D_s^+ mesons calculated with RAPGAP.

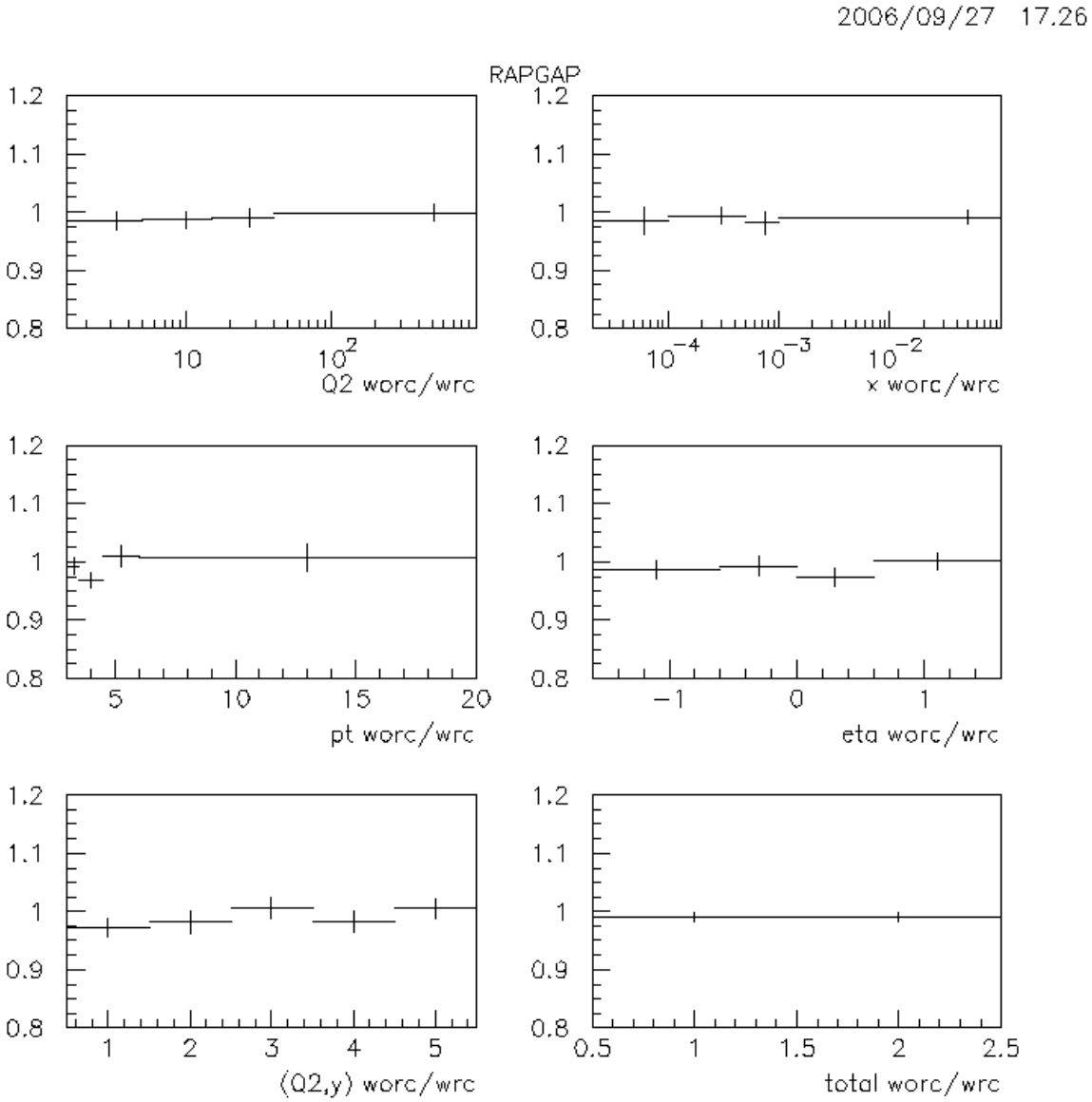

Figure 5.9: Values of the β-QED correction factors for $p_T(D) > 3\,\text{GeV}$ in bins of Q^2, x, $p_T(D)$, $\eta(D)$ and (Q^2, y).

Chapter 6

Charm Fragmentation Ratios and Fractions

In this chapter we measure the charm fragmentation ratios and fractions. Typically, these are defined as the relative productions of some particles with respect to others in charm fragmentation, and therefore involve ratios of cross sections in the full phase space. However, experimental limitations, *i.e.* finite available phase space in the measurements and impossibility of reconstruction or isolation of some signals, make impossible just to apply the theoretical definitions of ratios and fractions as they are. We are then forced to give an experimental definition of the quantities to be measured, involving necessarily some particular assumptions and prescriptions. In our approach, we express and evaluate all fractions and ratios as functions of the measured cross sections in the kinematic range $p_T(D) > 3\,\text{GeV}$ and $|\eta(D)| < 1.6$ presented in Chapter 5, plus one additional input, as we will see. In particular, finite phase space effects are treated by introducing what we call *"equivalent phase space"*. The whole procedure follows closely the treatment recently reported by ZEUS in the photoproduction regime [2].

6.1 Charm and charm-hadrons decays

Direct decays of charm quark occur mainly to one of the following states:

- *the non-strange charmed mesons* D^0, D^+ and their excited states D^{*0} and D^{*+};
- *the strange charmed meson* D_s^+ and its excited state D_s^{*+};
- *the charmed baryon* Λ_c^+;
- *the charmed strange baryons* Ξ_c^+, Ξ_c^0 and Ω_c^0.

Quark content of the previous particles is summarised in Table 6.1. Decays to heavier excited states are assumed to represent a small fraction of charm decays and are not considered.

The excited states D^{*0}, D^{*+} and D_s^{*+} always decay to some of the ground states:

- all D^{*0} decays produce a D^0 meson, *i.e.* $\sigma(D^{*0}) = \sigma(D^{*0} \to D^0\ X)$;
- the D^{*+} meson has only two possible decay modes, producing a D^0 or a D^+ meson, *i.e.* $\sigma(D^{*+}) = \sigma(D^{*+} \to D^0\pi_s^+) + \sigma(D^{*+} \to D^+\ X)$. The branching ratios corresponding to both decay channels are therefore subjected to the constraint $\mathcal{B}(D^{*+} \to D^0\pi_s^+) + \mathcal{B}(D^{*+} \to D^+\ X) = 1$;
- all D_s^{*+} decays produce a D_s^+ meson, *i.e.* $\sigma(D_s^{*+}) = \sigma(D_s^{*+} \to D_s^+\ X)$ [65].

From these considerations we can inmediately write the different terms contributing to the production of D^0, D^+ and D_s^+ mesons:

- D^0 production includes contributions from direct charm decays, D^{*0} decays and D^{*+} decays:

$$\sigma(D^0) = \sigma^{\rm dir}(D^0) + \sigma(D^{*0} \to D^0X) + \sigma(D^{*+} \to D^0\pi_s^+)\ ;$$

- D^+ production includes contributions from direct charm decays and from D^{*+} decays:

$$\sigma(D^+) = \sigma^{\rm dir}(D^+) + \sigma(D^{*+} \to D^+X)\ ;$$

- D_s^+ production includes contributions from direct charm decays and from D_s^{*+} decays:

$$\sigma(D_s^+) = \sigma^{\rm dir}(D_s^+) + \sigma(D_s^{*+} \to D_s^+X)\ .$$

6.2 Ratios and fractions : definitions

The theoretical definitions of all observables we want to measure should be first clearly stated. These ones will be used later as the basis to build the approximate, experimental definitions which are the ones we actually use to determine the values of our measurements.

6.2.1 Ratio of neutral to charge D-meson production rates

The ratio $R_{u/d}$ is defined as the relative production of u quark with respect to the production of d quark in charm fragmentation, in the D-meson sector:

$$R_{u/d} = \frac{c\bar{u}}{cd}\ .$$

Neglecting influences from heavier excited D-mesons, the direct production of u and d quarks is given by (see Table 6.1):

$$u \to \sigma(D^{*0}) + \sigma^{\rm dir}(D^0) \ ,$$
$$d \to \sigma(D^{*+}) + \sigma^{\rm dir}(D^+) \ .$$

Therefore $R_{u/d}$ becomes the ratio of neutral to charge D-meson production rates and it is given by the ratio of the sum of D^{*0} and direct D^0 production cross sections to the sum of D^{*+} and direct D^+ production cross sections:

$$R_{u/d} = \frac{\sigma(D^{*0}) + \sigma^{\rm dir}(D^0)}{\sigma(D^{*+}) + \sigma^{\rm dir}(D^+)} \ . \tag{6.1}$$

6.2.2 Strangeness-suppression factor

The strageness-suppresion factor, γ_s, is defined as twice the relative production of the s quark with respect to the d and u quarks in charm fragmentation, in the D-meson sector:

$$\gamma_s = \frac{2c\bar{s}}{cd + c\bar{u}} \ .$$

Neglecting influences from heavier excited D-mesons, the direct production of $c\bar{s}$, cd and $c\bar{u}$ quarks is given by (see Table 6.1):

$$\begin{aligned} 2c\bar{s} &\to 2\left\{\sigma^{\rm dir}(D_s^+) + \sigma(D_s^{*+})\right\} \\ &= \ 2\left\{\sigma^{\rm dir}(D_s^+) + \sigma(D_s^{*+} \to D_s^+ X)\right\} \\ &= \ 2\sigma(D_s^+) \ , \end{aligned}$$

$$\begin{aligned} cd + c\bar{u} &\to \sigma^{\rm dir}(D^0) + \sigma(D^{*0}) + \sigma^{\rm dir}(D^+) + \sigma(D^{*+}) \\ &= \sigma^{\rm dir}(D^0) + \sigma(D^{*0} \to D^0 X) \\ &\quad + \sigma^{\rm dir}(D^+) \\ &\quad + \sigma(D^{*+} \to D^0 X) + \sigma(D^{*+} \to D^+ X) \\ &= \sigma^{\rm dir}(D^0) + \sigma(D^{*0} \to D^0 X) + \sigma(D^{*+} \to D^0 X) \\ &\quad + \sigma^{\rm dir}(D^+) + \sigma(D^{*+} \to D^+ X) \\ &= \sigma(D^0) + \sigma(D^+) \ . \end{aligned}$$

Therefore, the strangeness-suppresion factor is given by the ratio of twice the D_s^+ production cross section to the sum of D^0 and D^+ production cross sections:

$$\gamma_s = \frac{2\sigma(D_s^+)}{\sigma(D^0) + \sigma(D^+)} \ . \tag{6.2}$$

6.2.3 Fraction of charged D mesons produced in a vector state

The fraction of D mesons produced in a vector state, $P_{\rm v}^d$, is defined as the relative production of vector charm mesons with respect to (vector+pseudoscalar) charm mesons, in charm fragmentation:

$$P_{\rm v}^d = \frac{V}{V+P} \ .$$

Neglecting influences from heavier excited D mesons, the direct production of vector and (vector+pseudoscalar) D mesons is given by:

$$\begin{aligned} V &\to \sigma(D^{*+}) \\ V+P &\to \sigma(D^{*+}) + \sigma^{\rm dir}(D^+) \ . \end{aligned}$$

Therefore, the fraction of D mesons produced in a vector state is given by the ratio of D^{*+} production cross section to the sum of D^{*+} and direct D^+ production cross sections:

$$P_{\rm v}^d = \frac{\sigma(D^{*+})}{\sigma(D^{*+}) + \sigma^{\rm dir}(D^+)} \ . \tag{6.3}$$

6.2.4 Charm fragmentation fractions

The charm fragmentation fraction $f(c \to D)$ is defined as the probability that a c quark hadronises as a particular charm hadron D. In terms of D and c production, we have

$$f(c \to D) = \frac{\sigma(D)}{\sigma(c)} \ .$$

As every c quark ends up decaying to one of the charm ground states, the whole c production is equal to the charm ground states production:

$$\sigma(c) \to \sigma_{\rm gs} = \sigma(D^0) + \sigma(D^+) + \sigma(D_s^+) + \sigma(\Lambda_c^+) + \sigma(\Xi_c^+, \Xi_c^0, \Omega_c^0) \ . \tag{6.4}$$

Therefore, for any charm hadron D (ground or excited state), we have

$$f(c \to D) = \frac{\sigma(D)}{\sigma_{\rm gs}} \ .$$

In our analysis, we measure the fragmentation fractions for the charm ground states D^0, D^+ and D_s^+ and for the D^{*+} meson, which are given by

$$\begin{aligned} f(c \to D^0) &= \sigma(D^0)/\sigma_{\rm gs} & f(c \to D^+) &= \sigma(D^+)/\sigma_{\rm gs} \\ f(c \to D_s^+) &= \sigma(D_s^+)/\sigma_{\rm gs} & f(c \to D^{*+}) &= \sigma(D^{*+})/\sigma_{\rm gs} \ . \end{aligned} \tag{6.5}$$

6.3 Ratios and fractions: evaluation

In the previous section we have defined the ratios $R_{u/d}$, γ_s and $P_{\rm v}^d$ and the fractions $f(c \to D^0, D^+, D_s^+, D^{*+})$, which are the observables in charm fragmentation that we measure. In this section we provide detailed computations of all cross sections needed for the evaluation of fractions and ratios. With these cross sections, we determine their values. All prescriptions, assumptions and additional inputs needed are also explained.

General

From the formulas derived in the previous section we have seen that a general observable X, *i.e.* ratio or fraction, is a function of the inclusive and perhaps also direct cross sections corresponding to the production of several charm hadrons D^i, in the full phase space:

$$X = f(\sigma(D^i), \sigma^{\rm dir}(D^i)) \ .$$

Signal reconstruction is necessarily performed not in the full phase space, but in some kinematic region which is determined by the detector. The production cross sections we measure are therefore refered to that region. It seems natural just to replace the cross sections in the full phase space by those measured in the accepted kinematic range $p_T(D) > 3\,\text{GeV}$ and $|\eta(D)| < 1.6$:

$$\begin{aligned} \sigma(D^i) &\to \sigma_{\rm kin}(D^i) \\ \sigma^{\rm dir}(D^i) &\to \sigma^{\rm dir}_{\rm kin}(D^i) \ , \end{aligned}$$

and take the last ones as the arguments of the function f to evaluate the observable X in the kinematic region:

$$X \to X_{\rm kin} = f(\sigma_{\rm kin}(D^i), \sigma^{\rm dir}_{\rm kin}(D^i)) \ .$$

Deciding if the proposed experimental definition needs or not extra corrections is something that can only be answered relying on a MC simulation. Using simulated data, one would compute the extrapolation factor corresponding to the observable X as the ratio between the value of X evaluated with the MC cross sections in the full phase space and the value of X evaluated with the MC cross sections in the accepted kinematic region:

$$\text{extrapolation}(X) = \frac{X^{\rm MC}}{X^{\rm MC}_{\rm kin}} \ .$$

MC studies show that to minimise differences between the values measured in the accepted kinematic region and those in the full phase space, *i.e.* having extrapolation

factors close to unity, the inclusive cross sections for D^0 and D^+ in the kinematic range $\sigma_{\rm kin}(D^0)$ and $\sigma_{\rm kin}(D^+)$ need to be corrected with extra terms [2]. Qualitative kinematic arguments can give us an idea about why and what kind of corrections are needed. Apart from the direct component, D^0 and D^+ production has contributions from D^* decays: D^0 production from D^{*0} and D^{*+} mesons, D^+ production from D^{*+} mesons. Let's analyze, as an example, the D^+ case. When a D^{*+} meson decays producing a D^+, only a fraction of the parent D^* momentum is transferred to the daughter D^+. This means that, even if the parent D^{*+} was produced inside the accepted kinematic region, the daughter D^+ may escape from the kinematic range, *i.e.*, it may be produced *outside* the kinematic range. Therefore, including only D^+ mesons reconstructed inside the kinematic range induces *losses* due to these boundary effects in the available phase space of the measurement. The relative production of D^+ with respect to D^{*+} measured in this way would be biased. The same arguments apply to the production of D^0 mesons. Therefore, to compare the inclusive D^+ and D^0 cross sections with each other and with the inclusive D^{*+} cross section it is necessary to include their non direct contributions which lie outside the accepted kinematic range. This is the idea behind the *equivalent phase space* treatment. The "equivalent" D^+ and D^0 cross sections will be defined as the sums of their direct cross sections and contributions from D^{*+} and D^{*0} decays:

$$\begin{aligned}\sigma(D^+) \to \sigma^{\rm eq}(D^+) &= \sigma^{\rm dir}_{\rm kin}(D^+) + \{\text{contributions from } D^{*+}\} \\ \sigma(D^0) \to \sigma^{\rm eq}(D^0) &= \sigma^{\rm dir}_{\rm kin}(D^0) + \{\text{contributions from } D^{*+} \text{and } D^{*0}\}\ .\end{aligned}$$

MC studies show that these effects are suppressed in D_s^+ production (which has a contribution from D_s^{*+}), and therefore no equivalent phase space tratment was used for the D_s^+ meson.

6.3.1 Ratio of neutral to charge D-meson production rates

The actual computation of $R_{u/d}$ represents an exception to the general treatment we claimed in the previous paragraph. In the definition with cross sections in the full phase space (Eq. 6.1) we make the replacements

$$\begin{aligned}\sigma(D^{*0}) &\to \sigma(D^{*0} \to D^0_{\rm in} X) \quad \text{(instead of } \sigma_{\rm kin}(D^{*0})) \\ \sigma^{\rm dir}(D^0) &\to \sigma^{\rm dir}_{\rm kin}(D^0) \\ \sigma(D^{*+}) &\to \frac{\sigma(D^{*+} \to D^0_{\rm in}\pi_s^+)}{\mathcal{B}(D^{*+} \to D^0\pi^+)} = \frac{\sigma^{\rm tag}(D^0)}{\mathcal{B}(D^{*+} \to D^0\pi^+)} \quad \text{(instead of } \sigma_{\rm kin}(D^{*+})) \\ \sigma^{\rm dir}(D^+) &\to \sigma^{\rm dir}_{\rm kin}(D^+)\ .\end{aligned}$$

We have used the subscript "in" to indicate "inside the kinematic region". In the same way, we will use the subscript "out" to denote "outside the kinematic region".

The direct production of D^+ mesons is estimated by subtracting the D^{*+} contribution to its inclusive production, in the kinematic region:

$$\sigma^{\rm dir}_{\rm kin}(D^+) = \sigma_{\rm kin}(D^+) - \sigma(D^{*+} \to D^+_{\rm in} X) \ .$$

To perform the subtraction, we notice that in the full phase space, production of D^+ and D^0 mesons originated from D^{*+} decays are related by scaling of their cross sections with the appropiate branching ratios:

$$\begin{aligned}\sigma(D^{*+} \to D^+ X) &= \sigma(D^{*+} \to D^0 \pi_s^+) \frac{\mathcal{B}(D^{*+} \to D^+ X)}{\mathcal{B}(D^{*+} \to D^0 \pi_s^+)} \\ &= \sigma(D^{*+} \to D^0 \pi_s^+) \frac{1 - \mathcal{B}(D^{*+} \to D^0 \pi_s^+)}{\mathcal{B}(D^{*+} \to D^0 \pi_s^+)} \ .\end{aligned}$$

Assuming that the kinematics of the reactions $D^{*+} \to D^+ X$ and $D^{*+} \to D^0 \pi_s^+$ is the same, the previous relation also holds in the kinematic region of the measurement:

$$\begin{aligned}\sigma(D^{*+} \to D^+_{\rm in} X) &= \sigma(D^{*+} \to D^0_{\rm in} \pi_s^+) \frac{1 - \mathcal{B}(D^{*+} \to D^0 \pi_s^+)}{\mathcal{B}(D^{*+} \to D^0 \pi_s^+)} \\ &= \sigma^{\rm tag}(D^0) \frac{1 - \mathcal{B}(D^{*+} \to D^0 \pi_s^+)}{\mathcal{B}(D^{*+} \to D^0 \pi_s^+)} \ ,\end{aligned}$$

and therefore

$$\boxed{\sigma^{\rm dir}_{\rm kin}(D^+) = \sigma_{\rm kin}(D^+) - \sigma^{\rm tag}(D^0) \frac{1 - \mathcal{B}(D^{*+} \to D^0 \pi_s^+)}{\mathcal{B}(D^{*+} \to D^0 \pi_s^+)} \ .}$$

We have now all the necessary pieces for the actual computation of $R_{u/d}$. Substitution in the general formula gives, for the numerator:

$$\sigma(D^{*0}) + \sigma^{\rm dir}(D^0) \to \sigma(D^{*0} \to D^0_{\rm in} X) + \sigma^{\rm dir}_{\rm kin}(D^0) = \sigma^{\rm untag}(D^0) \ ,$$

and, for the denominator:

$$\sigma(D^{*+}) + \sigma^{\rm dir}(D^+) \to \sigma^{\rm tag}(D^0) + \sigma_{\rm kin}(D^+) \ .$$

Our final expression for the experimental estimation of $R_{u/d}$ is, therefore

$$\boxed{R_{u/d} = \frac{\sigma^{\rm untag}(D^0)}{\sigma^{\rm tag}(D^0) + \sigma_{\rm kin}(D^+)} \ .}$$

Using the measured cross sections, the ratio of neutral to charged D-meson production rates is

$$R_{u/d} = 1.22 \pm 0.11({\rm stat.})^{+0.05}_{-0.02}({\rm syst.}) \pm 0.03({\rm br.}) \ .$$

The measured $R_{u/d}$ value agrees with unity, i.e. it is consistent with isospin invariance, which implies that u and d quarks are produced equally in charm fragmentation. In Table 6.2 and Fig. 6.1, this measurement is compared with those obtained in DIS by the H1 collaboration [4], in photoproduction [2] and in e^+e^- annihilations [76]. All measurements agree within experimental uncertainties.

6.3.2 Strangeness-suppression factor

According to the general treatment, in the definition of γ_s with cross sections in the full phase space (Eq. 6.2) we make the replacements

$$\begin{aligned}\sigma(D_s^+) &\to \sigma_{\rm kin}(D_s^+)\\ \sigma(D^0) &\to \sigma^{\rm eq}(D^0)\\ \sigma(D^+) &\to \sigma^{\rm eq}(D^+)\ .\end{aligned}$$

The equivalent D^0 cross section includes, apart from the direct component in the kinematic range, the contributions from D^{*+} and D^{*0} decays with the D^0 meson inside and outside the kinematic range:

$$\begin{aligned}\sigma^{\rm eq}(D^0) &= \sigma^{\rm dir}_{\rm kin}(D^0) + \sigma(D^{*0}\to D^0X) + \sigma(D^{*+}\to D^0\pi_s^+)\\ &= \sigma^{\rm dir}_{\rm kin}(D^0)\\ &\quad + \sigma(D^{*0}\to D^0_{\rm in}X) + \sigma(D^{*0}\to D^0_{\rm out}X)\\ &\quad + \sigma(D^{*+}\to D^0_{\rm in}\pi_s^+) + \sigma(D^{*+}\to D^0_{\rm out}\pi_s^+)\\ &= \sigma^{\rm dir}_{\rm kin}(D^0) + \sigma(D^{*0}\to D^0_{\rm in}X)\\ &\quad + \sigma(D^{*+}\to D^0_{\rm in}\pi_s^+)\\ &\quad + \sigma(D^{*+}\to D^0_{\rm out}\pi_s^+)\\ &\quad + \sigma(D^{*0}\to D^0_{\rm out}X)\\ &= \sigma^{\rm untag}(D^0)\\ &\quad + \sigma^{\rm tag}(D^0)\\ &\quad + \sigma^{\rm add}(D^{*+})\mathcal{B}(D^{*+}\to D^0\pi_s^+)\\ &\quad + \sigma(D^{*0}\to D^0_{\rm out}X)\ .\end{aligned}$$

The production of D^0 mesons outside the kinematic range from neutral and charged D^* decays is assumed to be identical, up to the factor $R_{u/d}$. Under this assumption, the last term in the previous equation, which escapes detection, becomes:

$$\sigma(D^{*0}\to D^0_{\rm out}X) = \sigma(D^{*+}\to D^0_{\rm out}\pi_s^+)R_{u/d} = \sigma^{\rm add}(D^{*+})\mathcal{B}(D^{*+}\to D^0\pi_s^+)R_{u/d}\ .$$

Our final expression for the equivalent D^0 cross section is therefore:

$$\boxed{\sigma^{\rm eq}(D^0) = \sigma^{\rm untag}(D^0) + \sigma^{\rm tag}(D^0) + \sigma^{\rm add}(D^{*+})\left\{R_{u/d} + \mathcal{B}(D^{*+}\to D^0\pi_s^+)\right\}\ .}$$

In a totally analogous way, the equivalent D^+ cross section includes, apart from the direct component in the kinematic range, the contribution from D^{*+} decays with

the D^+ meson inside and outside the kinematic range:

$$\begin{aligned}\sigma^{\rm eq}(D^+) &= \sigma^{\rm dir}_{\rm kin}(D^+) + \sigma(D^{*+} \to D^+ X) \\ &= \sigma^{\rm dir}_{\rm kin}(D^+) + \sigma(D^{*+} \to D^+_{\rm in} X) \\ &\quad + \sigma(D^{*+} \to D^+_{\rm out} X) \\ &= \sigma_{\rm kin}(D^+) + \sigma(D^{*+} \to D^+_{\rm out} X) \ .\end{aligned}$$

To estimate the last term, which escapes detection, we assume once more that production of D^+ and D^0 mesons originated from D^{*+} decays are identical in any kinematic range, up to branching ratio:

$$\begin{aligned}\sigma(D^{*+} \to D^+_{\rm out} X) &= \sigma(D^{*+} \to D^0_{\rm out}\pi^+_s)\frac{\mathcal{B}(D^{*+} \to D^+ X)}{\mathcal{B}(D^{*+} \to D^0\pi^+_s)} \\ &= \frac{\sigma(D^{*+} \to D^0_{\rm out}\pi^+_s)}{\mathcal{B}(D^{*+} \to D^0\pi^+_s)}\left\{1 - \mathcal{B}(D^{*+} \to D^0\pi^+_s)\right\} \\ &= \sigma^{\rm add}(D^{*+})\left\{1 - \mathcal{B}(D^{*+} \to D^0\pi^+_s)\right\}\end{aligned}$$

Substitution in the previous equation gives, for the equivalent D^+ cross section:

$$\boxed{\sigma^{\rm eq}(D^+) = \sigma_{\rm kin}(D^+) + \sigma^{\rm add}(D^{*+})\left\{1 - \mathcal{B}(D^{*+} \to D^0\pi^+_s)\right\} \ .}$$

Computation of the equivalent D^+ and D^0 cross sections completes the calculations needed to determine the strangeness suppression factor γ_s, which we evaluate according to:

$$\gamma_s = \frac{2\sigma_{\rm kin}(D^+_s)}{\sigma^{\rm eq}(D^0) + \sigma^{\rm eq}(D^+)} \ .$$

Using the expressions for $\sigma^{\rm eq}(D^0)$ and $\sigma^{\rm eq}(D^+)$, we get:

$$\boxed{\gamma_s = \frac{2\sigma_{\rm kin}(D^+_s)}{\sigma_{\rm kin}(D^+) + \sigma^{\rm untag}(D^0) + \sigma^{\rm tag}(D^0) + \sigma^{\rm add}(D^{*+})\left\{1 + R_{u/d}\right\}} \ .}$$

Using the measured cross sections, the strangeness-suppression factor is

$$\gamma_s = 0.225 \pm 0.030({\rm stat.})^{+0.018}_{-0.007}({\rm syst.})^{+0.034}_{-0.026}({\rm br.}) \ .$$

Table 6.3 and Fig. 6.1 compare this measurement with the values measured in photoproduction [2], in DIS by the H1 collaboration [4] and in e^+e^- annihilations [76]. All measurements agree within experimental uncertainties. The large branching-ratio uncertainties are dominated by the uncertainties of the $D^+_s \to \phi\pi^+$ branching ratio.

6.3.3 Fraction of charged D mesons produced in a vector state

According to the general treatment, in the definition of $P_{\rm v}^d$ with cross sections in the full phase space (Eq. 6.3) we make the replacements

$$\sigma(D^{*+}) \to \sigma_{\rm kin}(D^{*+})$$
$$\sigma^{\rm dir}(D^+) \to \sigma^{\rm dir}_{\rm kin}(D^+) \ .$$

The direct production of D^+ mesons in the kinematic region of the measurement was already computed in Subsection 6.3.1. The inclusive production of D^{*+} mesons in the kinematic range can be recovered from the production of D^0 mesons produced in D^{*+} decays, scaling with branching ratio:

$$\begin{aligned}
\sigma_{\rm kin}(D^{*+}) &= \frac{\sigma(D^{*+} \to D^0\pi_s^+)}{\mathcal{B}(D^{*+} \to D^0\pi^+)} \\
&= \frac{1}{\mathcal{B}(D^{*+} \to D^0\pi^+)} \left\{\sigma(D^{*+} \to D^0_{\rm in}\pi_s^+) + \sigma(D^{*+} \to D^0_{\rm out}\pi_s^+)\right\} \\
&= \frac{\sigma(D^{*+} \to D^0_{\rm in}\pi_s^+)}{\mathcal{B}(D^{*+} \to D^0\pi^+)} + \frac{\sigma(D^{*+} \to D^0_{\rm out}\pi_s^+)}{\mathcal{B}(D^{*+} \to D^0\pi^+)} \\
&= \frac{\sigma^{\rm tag}(D^0)}{\mathcal{B}(D^{*+} \to D^0\pi^+)} + \sigma^{\rm add}(D^{*+}) \ ,
\end{aligned}$$

that is,

$$\boxed{\sigma_{\rm kin}(D^{*+}) = \frac{\sigma^{\rm tag}(D^0)}{\mathcal{B}(D^{*+} \to D^0\pi^+)} + \sigma^{\rm add}(D^{*+}) \ .}$$

This completes the calculations needed to get, according to our treatment, the experimental formula we use to evaluate $P_{\rm v}^d$:

$$P_{\rm v}^d = \frac{\sigma_{\rm kin}(D^{*+})}{\sigma_{\rm kin}(D^{*+}) + \sigma^{\rm dir}_{\rm kin}(D^+)} \ .$$

Using the expressions for $\sigma_{\rm kin}(D^{*+})$ and $\sigma^{\rm dir}_{\rm kin}(D^+)$, we get:

$$\boxed{P_{\rm v}^d = \frac{\sigma^{\rm tag}(D^0)/\mathcal{B}(D^{*+} \to D^0\pi^+) + \sigma^{\rm add}(D^{*+})}{\sigma_{\rm kin}(D^+) + \sigma^{\rm tag}(D^0) + \sigma^{\rm add}(D^{*+})} \ .}$$

Using the measured cross sections, the fraction of charged D mesons produced in a vector state is

$$P_{\rm v}^d = 0.617 \pm 0.038({\rm stat.})^{+0.017}_{-0.009}({\rm syst.}) \pm 0.017({\rm br.}) \ .$$

The measured $P_{\rm v}^d$ value is smaller than the naive spin-counting prediction of 0.75. Recent calculations suggest a value which is closer to the measurement [77]. Table 6.4 and Fig. 6.1 compare this measurement with the values measured in photoproduction [2], in DIS by the H1 collaboration [4] and in e^+e^- annihilations [76]. All the measurements are consistent.

6.3.4 Charm fragmentation fractions

To compute the fractions of c quark hadronising as a D^0, D^+, D_s^+ and D^{*+} meson we start with the genaral formulas with cross sections in the full phase space (Eqs. 6.4 and 6.5) and replace the cross sections according to our general procedure:

$$\begin{aligned}\sigma(D^0) &\to \sigma^{\rm eq}(D^0)\\ \sigma(D^+) &\to \sigma^{\rm eq}(D^+)\\ \sigma(D_s^+) &\to \sigma_{\rm kin}(D_s^+)\\ \sigma(D^{*+}) &\to \sigma_{\rm kin}(D^{*+})\ .\end{aligned}$$

The contribution from the charmed strange baryons Ξ_c^+, Ξ_c^0 and Ω_c^0 and from the Λ_c^+ baryon still remains to be determined.

The production rates of the charm-strange baryons Ξ_c^+, Ξ_c^0 and Ω_c^0 were estimated from the non-charm sector following the LEP procedure [78]. The measured Ξ^-/Λ and Ω^-/Λ relative rates are $(6.65 \pm 0.28)\%$ and $(0.42 \pm 0.07)\%$, respectively [65]. Assuming equal production of Ξ^0 and Ξ^- states and that a similar suppression is applicable to the charm baryons, the total rate for the three charm-strange baryons relative to the Λ_c^+ state is expected to be about 14%:

$$\sigma(\Xi_c^+, \Xi_c^0, \Omega_c^0) \to 0.14 \cdot \sigma(\Lambda_c^+)\ .$$

Therefore, the Λ_c^+ production cross section was scaled by a factor 1.14 in the sum of the production cross sections:

$$\sigma_{\rm gs} = \sigma^{\rm eq}(D^0) + \sigma^{\rm eq}(D^+) + \sigma_{\rm kin}(D_s^+) + 1.14 \cdot \sigma(\Lambda_c^+)\ .$$

An error of ± 0.05 was assigned to the scale factor when evaluating systematic uncertainties.

The $\sigma(\Lambda_c^+)$ was estimated using the corresponding fragmentation fraction measured in e^+e^- [76], $f(c \to \Lambda_c^+)_{e^+e^-}$, by the relation below:

$$f(c \to \Lambda_c^+)_{e^+e^-} = \frac{\sigma(\Lambda_c^+)}{\sigma_{\rm gs}} = \frac{\sigma(\Lambda_c^+)}{\sigma^{\rm eq}(D^0) + \sigma^{\rm eq}(D^+) + \sigma_{\rm kin}(D_s^+) + 1.14 \cdot \sigma(\Lambda_c^+)}\ .$$

Solving the previous equation for $\sigma(\Lambda_c^+)$ gives:

$$\sigma(\Lambda_c^+) = \frac{f(c \to \Lambda_c^+)_{e^+e^-}\left\{\sigma^{\rm eq}(D^0) + \sigma^{\rm eq}(D^+) + \sigma_{\rm kin}(D_s^+)\right\}}{1 - 1.14 \cdot f(c \to \Lambda_c^+)_{e^+e^-}}\ ,$$

which, using the expressions for $\sigma^{\rm eq}(D^0)$ and $\sigma^{\rm eq}(D^+)$ can be rewrited as

$$\begin{aligned}\sigma(\Lambda_c^+) = &\frac{f(c \to \Lambda_c^+)_{e^+e^-}}{1 - 1.14 \cdot f(c \to \Lambda_c^+)_{e^+e^-}}\\ &\times \left\{\sigma_{\rm kin}(D^+) + \sigma^{\rm untag}(D^0) + \sigma^{\rm tag}(D^0) + \sigma^{\rm add}(D^{*+}) \cdot \left(1 + R_{u/d}\right)\right.\\ &\left. + \sigma_{\rm kin}(D_s^+)\right\}\ .\end{aligned}$$

The uncertainty of this procedure was estimated by using $f(c \to \Lambda_c^+)$ obtained in photoproduction [2], and considering the uncertainty in $f(c \to \Lambda_c^+)_{e^+e^-}$ [76].

With the expressions for $\sigma^{\mathrm{eq}}(D^0)$ and $\sigma^{\mathrm{eq}}(D^+)$ and the relation obtained for $\sigma(\Lambda_c^+)$, the sum of the production cross sections for all open-charm ground states is given by

$$\begin{aligned}\sigma_{\mathrm{gs}} = {} & \sigma_{\mathrm{kin}}(D^+) + \sigma^{\mathrm{untag}}(D^0) + \sigma^{\mathrm{tag}}(D^0) + \sigma^{\mathrm{add}}(D^{*+}) \cdot \left(1 + R_{u/d}\right) + \sigma_{\mathrm{kin}}(D_s^+) \\ & + 1.14 \cdot \frac{f(c \to \Lambda_c^+)_{e^+e^-}}{1 - 1.14 \cdot f(c \to \Lambda_c^+)_{e^+e^-}} \times \\ & \left\{\sigma_{\mathrm{kin}}(D^+) + \sigma^{\mathrm{untag}}(D^0) + \sigma^{\mathrm{tag}}(D^0) + \sigma^{\mathrm{add}}(D^{*+}) \cdot \left(1 + R_{u/d}\right) + \sigma_{\mathrm{kin}}(D_s^+)\right\} .\end{aligned}$$

Using the measured cross sections yields

$$\sigma_{\mathrm{gs}} = 13.7 \pm 0.6\,(\mathrm{stat.})^{+1.4}_{-0.6}\,(\mathrm{syst.}) \pm 0.6\,(\mathrm{br.})\,\mathrm{nb} .$$

The estimation of the contribution from the charmed strange baryons Ξ_c^+, Ξ_c^0 and Ω_c^0 and the estimation of the (non-observed) $\sigma(\Lambda_c^+)$ were the remaining pieces we needed to determine the charm fragmentation fractions, which are finally given by

$$\begin{aligned} f(c \to D^0) &= \sigma^{\mathrm{eq}}(D^0)/\sigma_{\mathrm{gs}} & f(c \to D^+) &= \sigma^{\mathrm{eq}}(D^+)/\sigma_{\mathrm{gs}} \\ f(c \to D_s^+) &= \sigma_{\mathrm{kin}}(D_s^+)/\sigma_{\mathrm{gs}} & f(c \to D^{*+}) &= \sigma_{\mathrm{kin}}(D^{*+})/\sigma_{\mathrm{gs}} . \end{aligned}$$

Using the expressions for $\sigma^{\mathrm{eq}}(D^0)$, $\sigma^{\mathrm{eq}}(D^+)$ and $\sigma_{\mathrm{kin}}(D^{*+})$, we have

$$\begin{aligned} f(c \to D^0) &= \frac{\sigma^{\mathrm{untag}}(D^0) + \sigma^{\mathrm{tag}}(D^0) + \sigma^{\mathrm{add}}(D^{*+})\left\{R_{u/d} + \mathcal{B}(D^{*+} \to D^0\pi_s^+)\right\}}{\sigma_{\mathrm{gs}}} \\ f(c \to D^+) &= \frac{\sigma_{\mathrm{kin}}(D^+) + \sigma^{\mathrm{add}}(D^{*+})\left\{1 - \mathcal{B}(D^{*+} \to D^0\pi_s^+)\right\}}{\sigma_{\mathrm{gs}}} \\ f(c \to D_s^+) &= \frac{\sigma_{\mathrm{kin}}(D_s^+)}{\sigma_{\mathrm{gs}}} \\ f(c \to D^{*+}) &= \frac{\sigma^{\mathrm{tag}}(D^0)/\mathcal{B}(D^{*+} \to D^0\pi_s^+) + \sigma^{\mathrm{add}}(D^{*+})}{\sigma_{\mathrm{gs}}} . \end{aligned}$$

The open-charm fragmentation fractions, measured in the kinematic region $1.5 < Q^2 < 1000\,\mathrm{GeV}^2$, $0.02 < y < 0.7$, $p_T(D) > 3\,\mathrm{GeV}$ and $|\eta(D)| < 1.6$, are summarised in Table 6.5 and Fig. 6.1. The results are compared with the values obtained in photoproduction [2], in DIS by the H1 collaboration [4] and in e^+e^- annihilations [76]. All the measurements are consistent. A Monte Carlo study [2] suggested that the measured charm fragmentation ratios and fractions are close to those in the full $p_T(D)$ and $\eta(D)$ phase space.

The hadronisation fraction into untagged D^0, needed later for comparisons with theory, is defined as the probability that a c quark originates as a D^0 which has not

been produced in a D^{*+} decay. Therefore, we have the identity:

$$f^{\text{untag}}(c \to D^0) = f(c \to D^0) - f(c \to D^{*+})\mathcal{B}(D^{*+} \to D^0\pi_s^+) \ .$$

Substituting the expressions for $f(c \to D^0)$ and $f(c \to D^{*+})$ we get:

$$\boxed{f^{\text{untag}}(c \to D^0) = \frac{\sigma^{\text{untag}}(D^0) + \sigma^{\text{add}}(D^{*+})R_{u/d}}{\sigma_{\text{gs}}} \ .}$$

Using the measured cross sections, the value for $f^{\text{untag}}(c \to D^0)$ is

$$f^{\text{untag}}(c \to D^0) = 0.450 \pm 0.020(\text{stat.}) \ {}^{+0.009}_{-0.039}(\text{syst.}) \ {}^{+0.012}_{-0.017}(\text{br.}) \ .$$

Charmed hadron	Quark content
D^0, D^{*0}	$c\bar{u}$
D^+, D^{*+}	$c\bar{d}$
D_s^+, D_s^{*+}	$c\bar{s}$
Λ_c^+	udc
Ξ_c^+	usc
Ξ_c^0	dsc
Ω_c^0	ssc

Table 6.1: Quark content of the different charmed hadrons.

	$R_{u/d}$
ZEUS (DIS)	$1.22 \pm 0.11(\text{stat.})^{+0.05}_{-0.02}(\text{syst.}) \pm 0.03(\text{br.})$
ZEUS (γp) [2]	$1.100 \pm 0.078(\text{stat.})^{+0.038}_{-0.061}(\text{syst.})^{+0.047}_{-0.049}(\text{br.})$
combined e^+e^- data	$1.020 \pm 0.069(\text{stat.} \oplus \text{syst.})^{+0.045}_{-0.047}(\text{br.})$
H1 (DIS) [4]	$1.26 \pm 0.20(\text{stat.}) \pm 0.11(\text{syst.}) \pm 0.04(\text{br.} \oplus \text{theory})$

Table 6.2: The ratio of neutral to charged D-meson production rates, $R_{u/d}$. The e^+e^- values are taken from [2]; they are an update of the compilation in [76] using the branching-ratio values of [79]. The measurements in this analysis, ZEUS (DIS), took the values for all the branching ratios involved from [65], the rest of the quoted measurements took them from [79].

	γ_s
ZEUS (DIS)	$0.225 \pm 0.030(\text{stat.})^{+0.018}_{-0.007}(\text{syst.})^{+0.034}_{-0.026}(\text{br.})$
ZEUS (γp) [2]	$0.257 \pm 0.024(\text{stat.})^{+0.013}_{-0.016}(\text{syst.})^{+0.078}_{-0.049}(\text{br.})$
ZEUS (γp) [11]	$0.27 \pm 0.04(\text{stat.})^{+0.02}_{-0.03}(\text{syst.}) \pm 0.07(\text{br.})$
combined e^+e^- data	$0.259 \pm 0.023(\text{stat.} \oplus \text{syst.})^{+0.087}_{-0.052}(\text{br.})$
H1 (DIS) [4]	$0.36 \pm 0.10(\text{stat.}) \pm 0.01(\text{syst.}) \pm 0.08(\text{br.} \oplus \text{theory})$

Table 6.3: The strangeness-suppression factor in charm fragmentation, γ_s. The e^+e^- values are taken from [2]; they are an update of the compilation in [76] using the branching-ratio values of [79]. The measurements in this analysis, ZEUS (DIS), took the values for all the branching ratios involved from [65], the rest of the quoted measurements took them from [79].

	$P_{\rm v}^d$
ZEUS (DIS)	$0.617 \pm 0.038(\text{stat.})^{+0.017}_{-0.009}(\text{syst.}) \pm 0.017(\text{br.})$
ZEUS (γp) [2]	$0.566 \pm 0.025(\text{stat.})^{+0.007}_{-0.022}(\text{syst.})^{+0.022}_{-0.023}(\text{br.})$
combined e^+e^- data	$0.614 \pm 0.019(\text{stat.} \oplus \text{syst.})^{+0.023}_{-0.025}(\text{br.})$
H1 (DIS) [4]	$0.693 \pm 0.045(\text{stat.}) \pm 0.004(\text{syst.}) \pm 0.009(\text{br.} \oplus \text{theory})$

Table 6.4: The fraction of charged D mesons produced in a vector state, $P_{\rm v}^d$. The e^+e^- values are taken from [2]; they are an update of the compilation in [76] using the branching-ratio values of [79]. The measurements in this analysis, ZEUS (DIS), took the values for all the branching ratios involved from [65], the rest of the quoted measurements took them from [79].

	ZEUS (DIS) $p_T(D) > 3\,\text{GeV}$ $\lvert\eta(D)\rvert < 1.6$	ZEUS (γp) [2] $p_T(D) > 3.8\,\text{GeV}$ $\lvert\eta(D)\rvert < 1.6$	Combined e^+e^- data [76]	H1 (DIS) [4]
	stat. syst. br.	stat. syst.	stat.$\oplus$syst. br.	total
$f(c \to D^+)$	$0.216 \pm 0.019\ ^{+0.002\,+0.008}_{-0.020\,-0.010}$	$0.217 \pm 0.014\ ^{+0.013}_{-0.005}$	$0.226\ \pm 0.010\ ^{+0.016}_{-0.014}$	0.203 ± 0.026
$f(c \to D^0)$	$0.605 \pm 0.020\ ^{+0.009\,+0.015}_{-0.052\,-0.023}$	$0.523 \pm 0.021\ ^{+0.018}_{-0.017}$	$0.557\ \pm 0.023\ ^{+0.014}_{-0.013}$	0.560 ± 0.046
$f(c \to D_s^+)$	$0.092 \pm 0.011\ ^{+0.007\,+0.012}_{-0.008\,-0.010}$	$0.095 \pm 0.008\ ^{+0.005}_{-0.005}$	$0.101\ \pm 0.009\ ^{+0.034}_{-0.020}$	0.151 ± 0.055
$f(c \to D^{*+})$	$0.229 \pm 0.011\ ^{+0.006\,+0.007}_{-0.021\,-0.010}$	$0.200 \pm 0.009\ ^{+0.008}_{-0.006}$	$0.238\ \pm 0.007\ ^{+0.003}_{-0.003}$	0.263 ± 0.032

Table 6.5: The fractions of c quarks hadronising as a particular charm hadron, $f(c \to D)$. The fractions are shown for the D^+, D^0 and D_s^+ charm ground states and for the D^{*+} state. The measurements in this analysis, ZEUS (DIS), took the values for all the branching ratios involved from [65], the rest of the quoted measurements took them from [79].

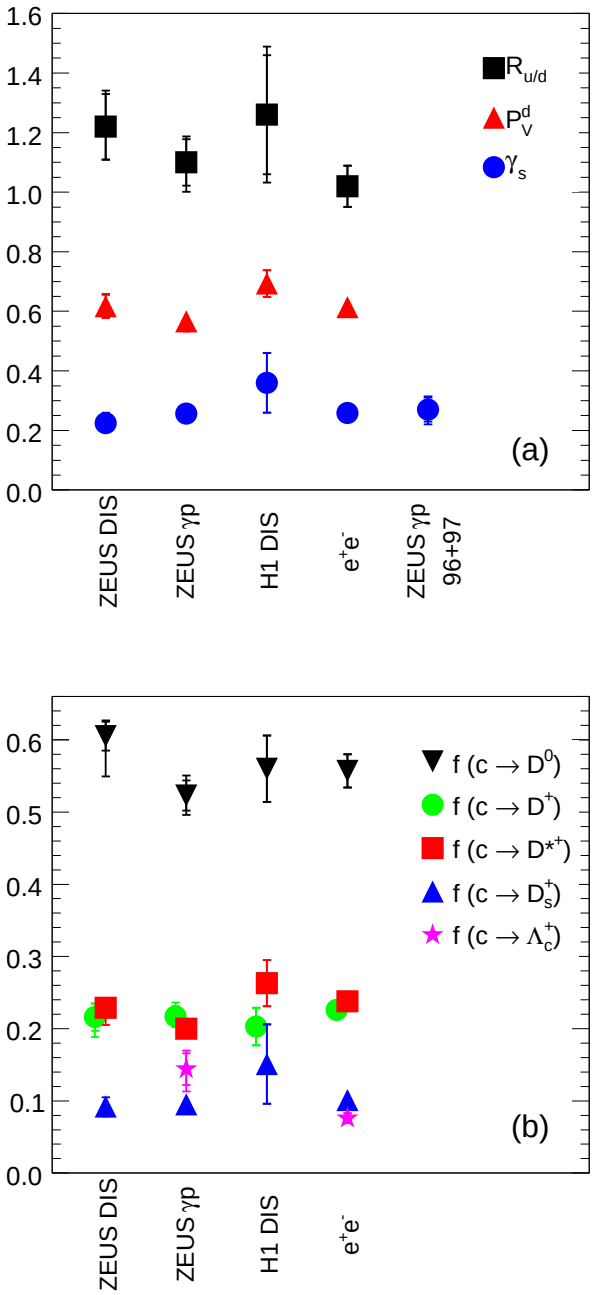

Figure 6.1: (a) The ratio of neutral to charged D-meson production rates, $R_{u/d}$, the strangeness-suppression factor in charm fragmentation, γ_s, and the fraction of charged D mesons produced in a vector state, $P_{\rm v}^d$. (b) The fractions of c quarks hadronising as D^+, D^0 and D_s^+ charm ground-state mesons, as D^{*+} mesons and as Λ_c^+ baryons. The inner error bars show the statistical uncertainties and the outer bars show the statistical and systematic uncertainties added in quadrature. The measurements have further uncertainties coming from the different branching ratios involved; their magnitudes are shown in Tables 6.2, 6.3 and 6.4 for $R_{u/d}$, γ_s and $P_{\rm v}^d$, respectively, and in Table 6.5 for the fractions.

Chapter 7

Cross Sections and pQCD Comparisons

In this chapter the production of untagged D^0, D^+ and D_s^+ mesons in bins of Q^2, x, $p_T(D)$ and $\eta(D)$ is studied. Measured cross sections are compared to the theoretical predictions given by pQCD.

7.1 Theoretical predictions

The next-to-leading order (NLO) QCD predictions for $c\bar{c}$ cross sections were obtained using the HVQDIS program [33] based on the so-called fixed-flavour-number scheme (FFNS). In this scheme, only light partons (u, d, s, g) are included in the proton parton density functions (PDFs) which obey the DGLAP equations [80], and the $c\bar{c}$ pair is produced via the BGF mechanism [32] with NLO corrections [34]. This calculation is expected to be valid in the kinematic range of this measurement, a photon virtuality $1.5 < Q^2 < 1000$ GeV^2.

The following inputs have been used to obtain the predictions for D-meson production at NLO using the program HVQDIS. The FFNS variant of the ZEUS-S NLO QCD fit [24] to structure-function data was used as the parameterisation of the proton PDFs. In this fit $\Lambda^{(3)}_{\rm QCD}$ was set to 0.363 GeV and the mass of the charm quark was set to 1.35 GeV; the same mass and $\Lambda^{(3)}_{\rm QCD}$ were therefore used in the HVQDIS calculation. The renormalisation and factorisation scales were set to $\mu = \sqrt{Q^2 + 4m_c^2}$ for charm production both in the fit and in the HVQDIS calculation. The charm fragmentation to the particular D meson was carried out using the Peterson function [39]. The values used for the hadronisation fractions to D mesons, $f(c \to D)$, were those measured in this paper, and the Peterson parameter, ϵ, was set to 0.035[81]. The effect of J/ψ production was found to be negligible [82, 83].

7.2 Total cross sections

For the cross sections presented in Chapter 5 the predictions from the HVQDIS program are $\sigma_{\rm kin}(D^0) = 7.90$ nb, $\sigma^{\rm untag}(D^0) = 5.88$ nb, $\sigma_{\rm kin}(D^+) = 2.82$ nb and $\sigma_2(D_s^+) = 2.40$ nb, with uncertainties around 15%, dominated by the input PDF and the mass of the charm quark. They are in good agreement with the data.

7.3 Differential cross sections

Reconstruction of D^0, D^+ and D_s^+ mesons in the kinematic region $1.5 < Q^2 < 1000$ GeV^2, $0.02 < y < 0.7$, $p_T(D^0, D^+, \{D_s^+\}) > 3\{2\}$ GeV and $|\eta(D)| < 1.6$ has been done in bins of Q^2, x, $p_T(D)$ and $\eta(D)$ according to the procedures described in Chapter 4. Figures 7.1, 7.2 and 7.3 show the corresponding mass distributions fitted with the appropiate fuctions modelling signal and background, which allows to extract the number of reconstructed mesons in each case. In addition, Figure 7.4 shows the mass distributions for the three particles in bins of (Q^2, y).

The differential cross sections for untagged D^0 (the D^0 mesons coming from D^{*+} are already included in the previous ZEUS publication [3]), D^+ and D_s^+ as a function of Q^2, x, $p_T(D)$ and $\eta(D)$ are shown in Figs. 7.5, 7.6 and 7.7 and given in Tables 7.1 and 7.2. All cross sections are measured in the kinematic region. The subscript "kin" has been removed to simplify the notation. The cross sections in Q^2 and x both fall by about three orders of magnitude in the measured region. The cross-section $d\sigma/dp_T(D)$ falls by two orders of magnitude with increasing $p_T(D)$. The cross-section $d\sigma/d\eta(D^0)$ shows a mild increase with increasing $\eta(D^0)$; for the D^+ and D_s^+ no statistically significant dependence with $\eta(D)$ is observed.

Figures 7.5, 7.6 and 7.7 show also the corresponding NLO calculations implemented in the HVQDIS program as well as their uncertainties (Section 8.2). All the differential cross sections measured are well described by the NLO calculation.

	untagged D^0			D^+		
Q^2 bin (GeV^2)	$d\sigma/dQ^2$	Δ_{stat} ($\mathrm{nb/\,GeV}^2$)	Δ_{syst}	$d\sigma/dQ^2$	Δ_{stat} ($\mathrm{nb/\,GeV}^2$)	Δ_{syst}
1.5, 5	0.56	± 0.08	$^{+0.09}_{-0.03}$	0.275	± 0.066	$^{+0.056}_{-0.044}$
5, 15	0.141	± 0.008	$^{+0.011}_{-0.006}$	0.089	± 0.014	$^{+0.003}_{-0.010}$
15, 40	0.044	± 0.005	$^{+0.003}_{-0.002}$	0.016	± 0.003	$^{+0.002}_{-0.001}$
40, 1000	0.0012	± 0.0002	$^{+0.0002}_{-0.0001}$	0.0007	± 0.0002	$^{+0.0001}_{-0.0001}$
x bin	$d\sigma/dx$	Δ_{stat} (nb)	Δ_{syst}	$d\sigma/dx$	Δ_{stat} (nb)	Δ_{syst}
0.000021, 0.0001	15197	± 2543	$^{+1137}_{-5789}$	4470	± 1572	$^{+1078}_{-1112}$
0.0001, 0.0005	4162	± 304	$^{+457}_{-231}$	2295	± 327	$^{+157}_{-199}$
0.0005, 0.001	1476	± 195	$^{+128}_{-72}$	1049	± 178	$^{+39}_{-125}$
0.001, 0.1	20.7	± 2.3	$^{+2.7}_{-1.0}$	10.5	± 2.2	$^{+1.4}_{-0.5}$
$p_T(D)$ bin (GeV)	$d\sigma/dp_T(D^0)$	Δ_{stat} ($\mathrm{nb/\,GeV}$)	Δ_{syst}	$d\sigma/dp_T(D^+)$	Δ_{stat} ($\mathrm{nb/\,GeV}$)	Δ_{syst}
3.0, 3.5	3.13	± 0.39	$^{+0.28}_{-0.12}$	1.61	± 0.44	$^{+0.45}_{-0.21}$
3.5, 4.5	1.93	± 0.20	$^{+0.12}_{-0.11}$	0.77	± 0.14	$^{+0.09}_{-0.06}$
4.5, 6.0	0.78	± 0.11	$^{+0.05}_{-0.08}$	0.49	± 0.08	$^{+0.05}_{-0.02}$
6.0, 20.	0.051	± 0.009	$^{+0.004}_{-0.003}$	0.028	± 0.007	$^{+0.002}_{-0.001}$
$\eta(D)$ bin	$d\sigma/d\eta(D^0)$	Δ_{stat} (nb)	Δ_{syst}	$d\sigma/d\eta(D^+)$	Δ_{stat} (nb)	Δ_{syst}
-1.6, -0.6	1.18	± 0.19	$^{+0.13}_{-0.10}$	0.65	± 0.11	$^{+0.08}_{-0.09}$
-0.6, 0.0	1.59	± 0.19	$^{+0.10}_{-0.11}$	1.20	± 0.25	$^{+0.15}_{-0.22}$
0.0, 0.6	2.05	± 0.22	$^{+0.18}_{-0.14}$	1.06	± 0.21	$^{+0.08}_{-0.15}$
0.6, 1.6	2.31	± 0.37	$^{+0.09}_{-0.20}$	0.74	± 0.23	$^{+0.22}_{-0.07}$

Table 7.1: Measured differential cross sections for D^0 not coming from a D^{*+} (left), and D^+ (right) as a function of Q^2, x, $p_T(D)$ and $\eta(D)$ for $1.5 < Q^2 < 1000$ GeV^2, $0.02 < y < 0.7$, $p_T(D) > 3$ GeV and $|\eta(D)| < 1.6$. The estimated b-quark contribution of 3.1 % has been subtracted. The statistical and systematic uncertainties are shown separately. The D^0 (D^+) cross sections have a further 1.8% (3.6%) uncertainty from the $D^0 \to K^-\pi^+$ ($D^+ \to K^-\pi^+\pi^+$) branching ratios.

D_s^+

Q^2 bin (GeV^2)	$d\sigma/dQ^2$	Δ_{stat} (nb/ GeV^2)	Δ_{syst}
1.5, 5	0.31	± 0.07	$^{+0.08}_{-0.05}$
5, 15	0.092	± 0.016	$^{+0.004}_{-0.017}$
15, 40	0.016	± 0.005	$^{+0.004}_{-0.003}$
40, 1000	0.00025	± 0.00010	$^{+0.00008}_{-0.00004}$
x bin	$d\sigma/dx$	Δ_{stat} (nb)	Δ_{syst}
0.000021, 0.0001	4982	± 1967	$^{+1354}_{-1333}$
0.0001, 0.0005	2765	± 443	$^{+65}_{-644}$
0.0005, 0.001	934	± 250	$^{+118}_{-155}$
0.001, 0.1	6.1	± 1.5	$^{+0.8}_{-0.6}$
$p_T(D_s^+)$ bin (GeV)	$d\sigma/dp_T(D_s^+)$	Δ_{stat} (nb/ GeV)	Δ_{syst}
2.0, 2.5	1.65	± 0.52	$^{+0.36}_{-0.50}$
2.5, 3.0	0.62	± 0.22	$^{+0.14}_{-0.11}$
3.0, 3.5	0.59	± 0.21	$^{+0.08}_{-0.12}$
3.5, 4.5	0.55	± 0.11	$^{+0.05}_{-0.05}$
4.5, 6.0	0.20	± 0.05	$^{+0.02}_{-0.01}$
6.0, 20.	0.011	± 0.004	$^{+0.002}_{-0.001}$
$\eta(D_s^+)$ bin	$d\sigma/d\eta(D_s^+)$	Δ_{stat} (nb)	Δ_{syst}
-1.6, -0.6	0.94	± 0.24	$^{+0.11}_{-0.26}$
-0.6, 0.0	0.57	± 0.15	$^{+0.14}_{-0.04}$
0.0, 0.6	0.76	± 0.18	$^{+0.06}_{-0.09}$
0.6, 1.6	0.85	± 0.22	$^{+0.17}_{-0.12}$

Table 7.2: Measured D_s^+ differential cross sections as a function of Q^2, x, $p_T(D_s^+)$ and $\eta(D_s^+)$ for $1.5 < Q^2 < 1000$ GeV^2, $0.02 < y < 0.7$, $p_T(D_s^+) > 2$ GeV and $|\eta(D_s^+)| < 1.6$. The estimated b-quark contribution of 4.3 % has been subtracted. The statistical and systematic uncertainties are shown separately. The cross sections have a further 13% uncertainty from the $D_s^+ \to \phi\pi^+ \to K^+K^-\pi^+$ branching ratio.

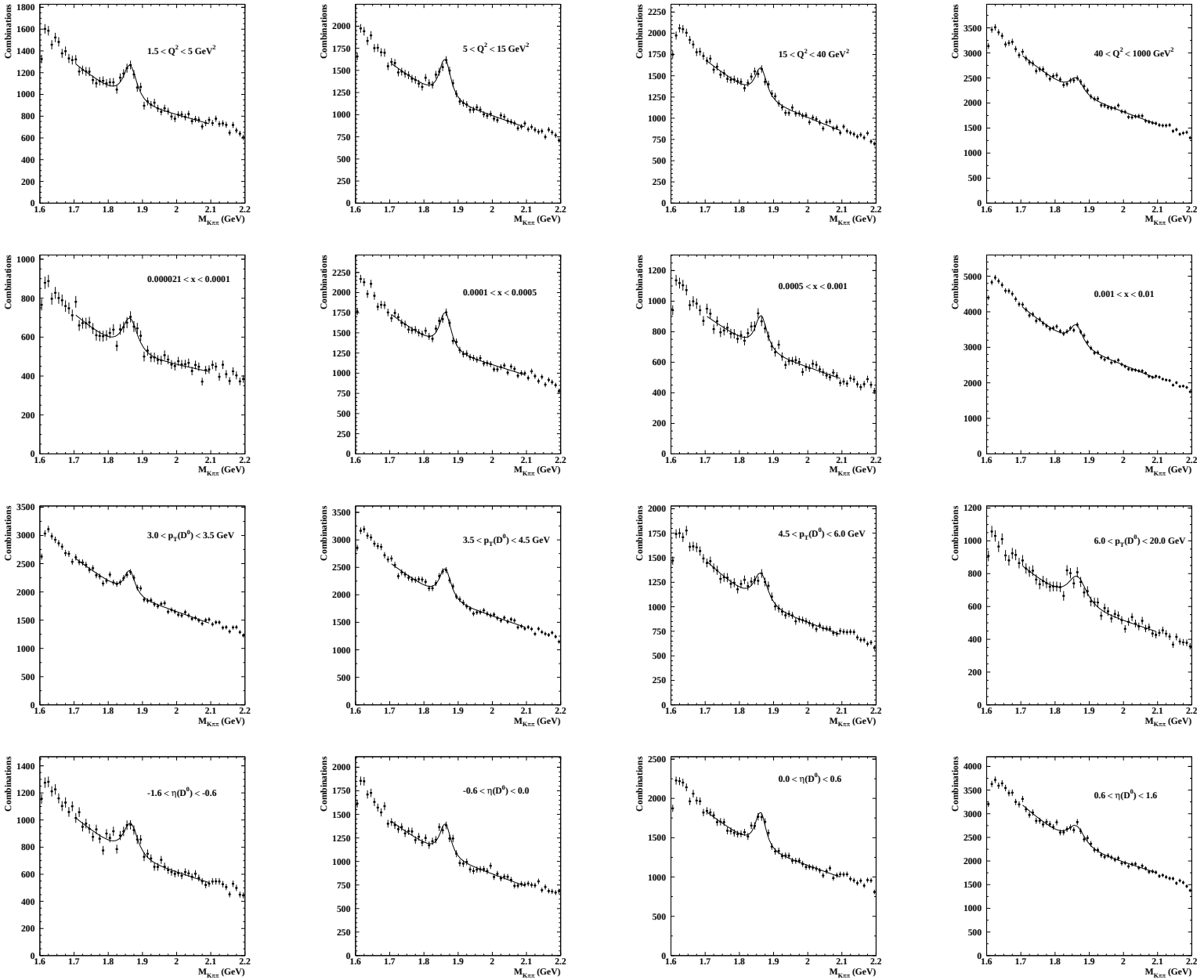

Figure 7.1: The $M(K^-, \pi^+)$ distributions for untagged D^0 candidates in bins of Q^2, x, $p_T(D^0)$ and $\eta(D^0)$.

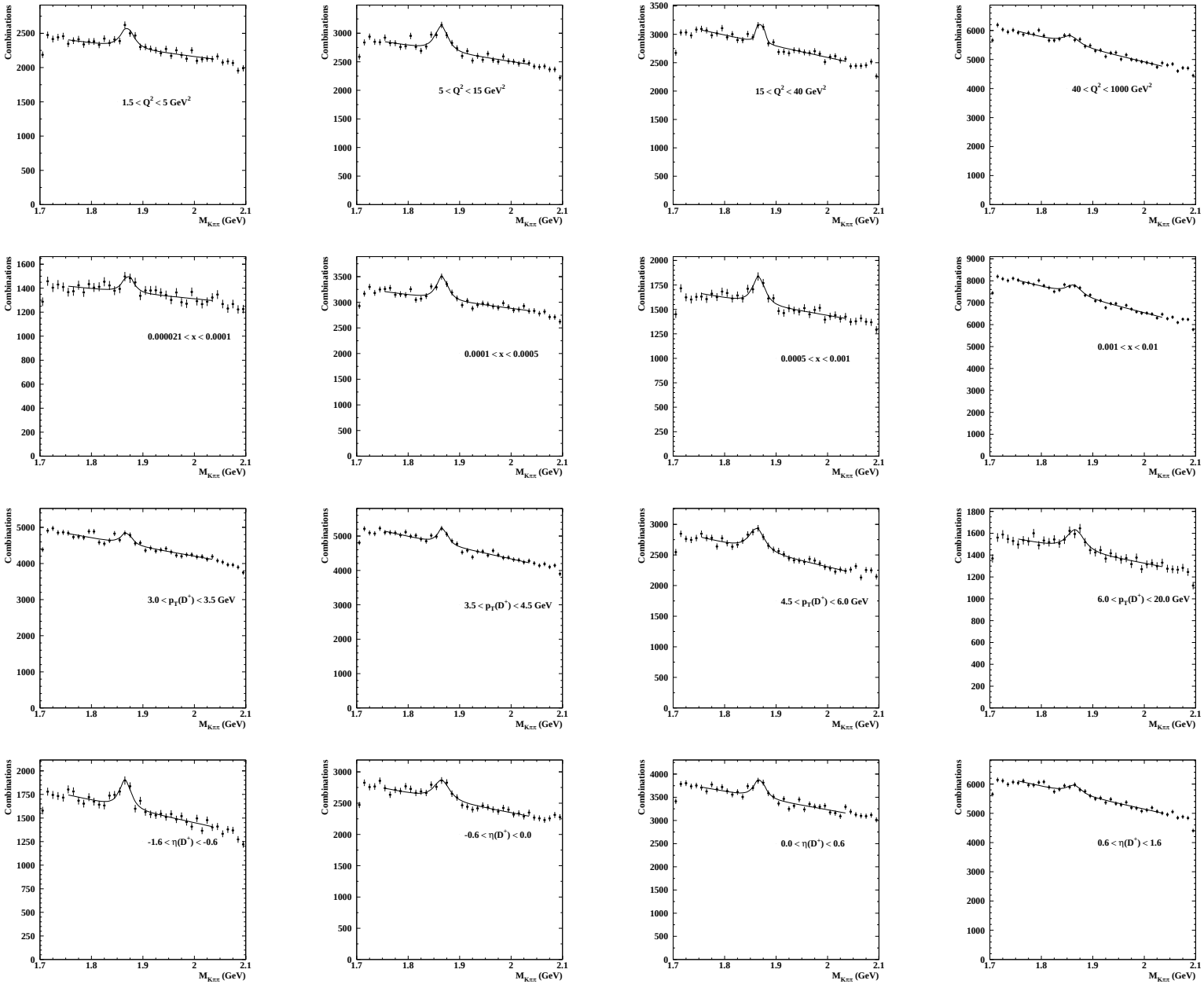

Figure 7.2: The $M(K^-, \pi^+, \pi^+)$ distributions for D^+ candidates in bins of Q^2, x, $p_T(D^+)$ and $\eta(D^+)$.

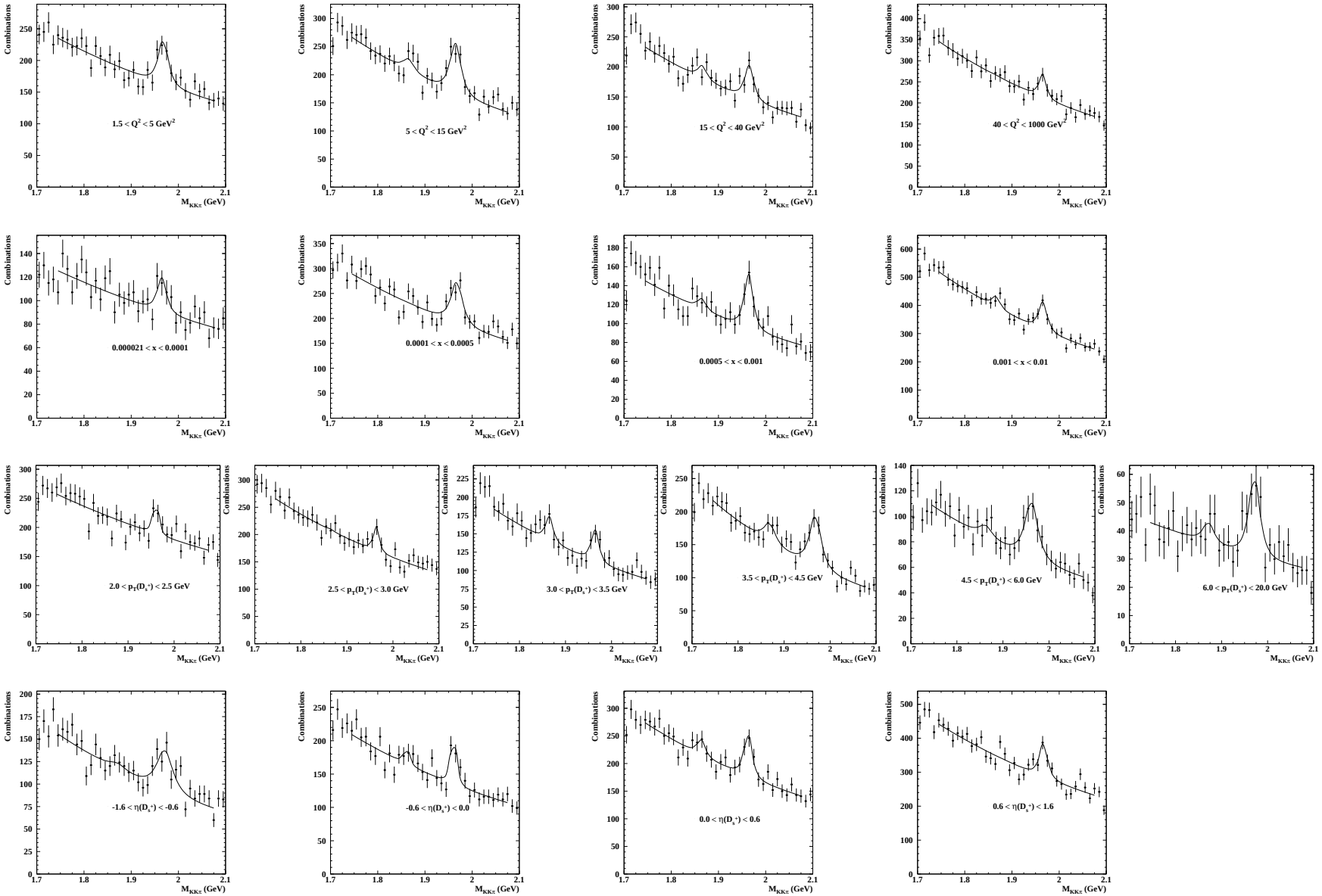

Figure 7.3: The $M(K^-, K^+, \pi^+)$ distributions for D_s^+ candidates in bins of Q^2, x, $p_T(D_s^+)$ and $\eta(D_s^+)$.

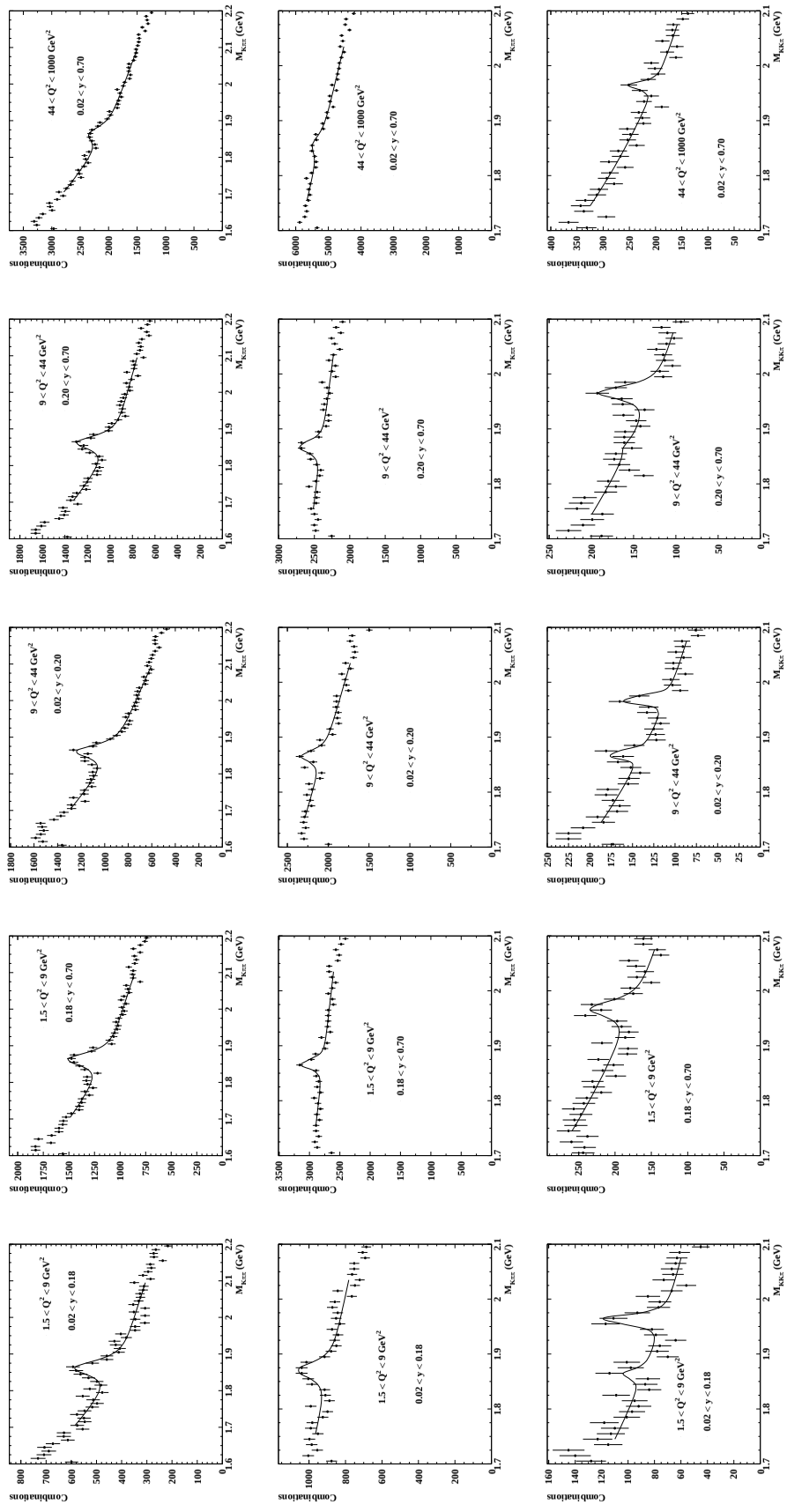

Figure 7.4: The $M(K^-,\pi^+)$, $M(K^-,\pi^+,\pi^+)$ and $M(K^-,K^+,\pi^+)$ distributions for untagged D^0, D^+ and D_s^+ candidates respectively, in bins of (Q^2, y).

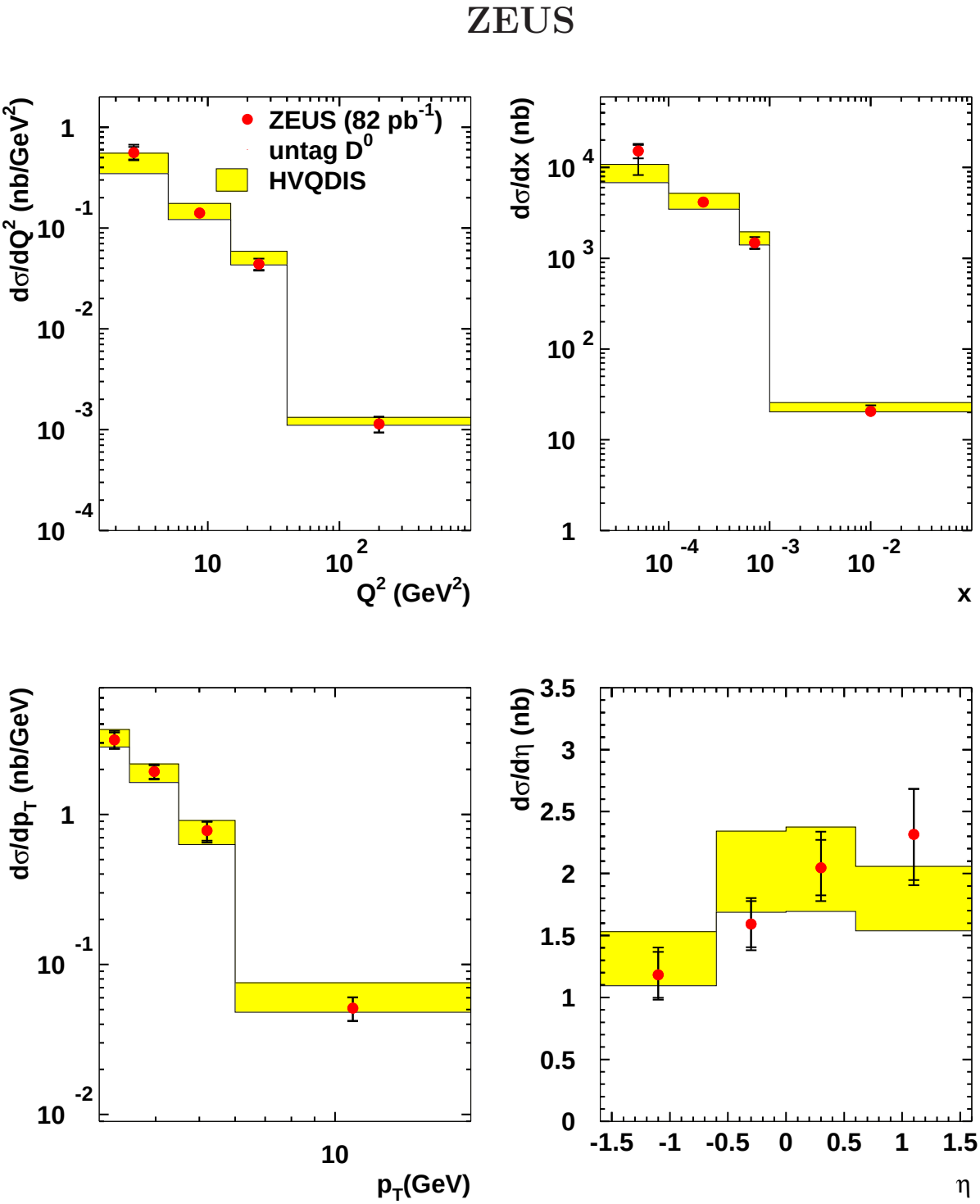

Figure 7.5: Differential cross sections for D^0 not coming from D^{*+} as a function of Q^2, x, $p_T(D^0)$ and $\eta(D^0)$ compared to the NLO QCD calculation of HVQDIS. The inner error bars show the statistical uncertainties and the outer bars show the statistical and systematic uncertainties added in quadrature. The lower and upper NLO QCD predictions show the estimated theoretical uncertainty of the HVQDIS calculations. The data points have a further 1.8% uncertainty from the $D^0 \to K^-\pi^+$ branching ratio.

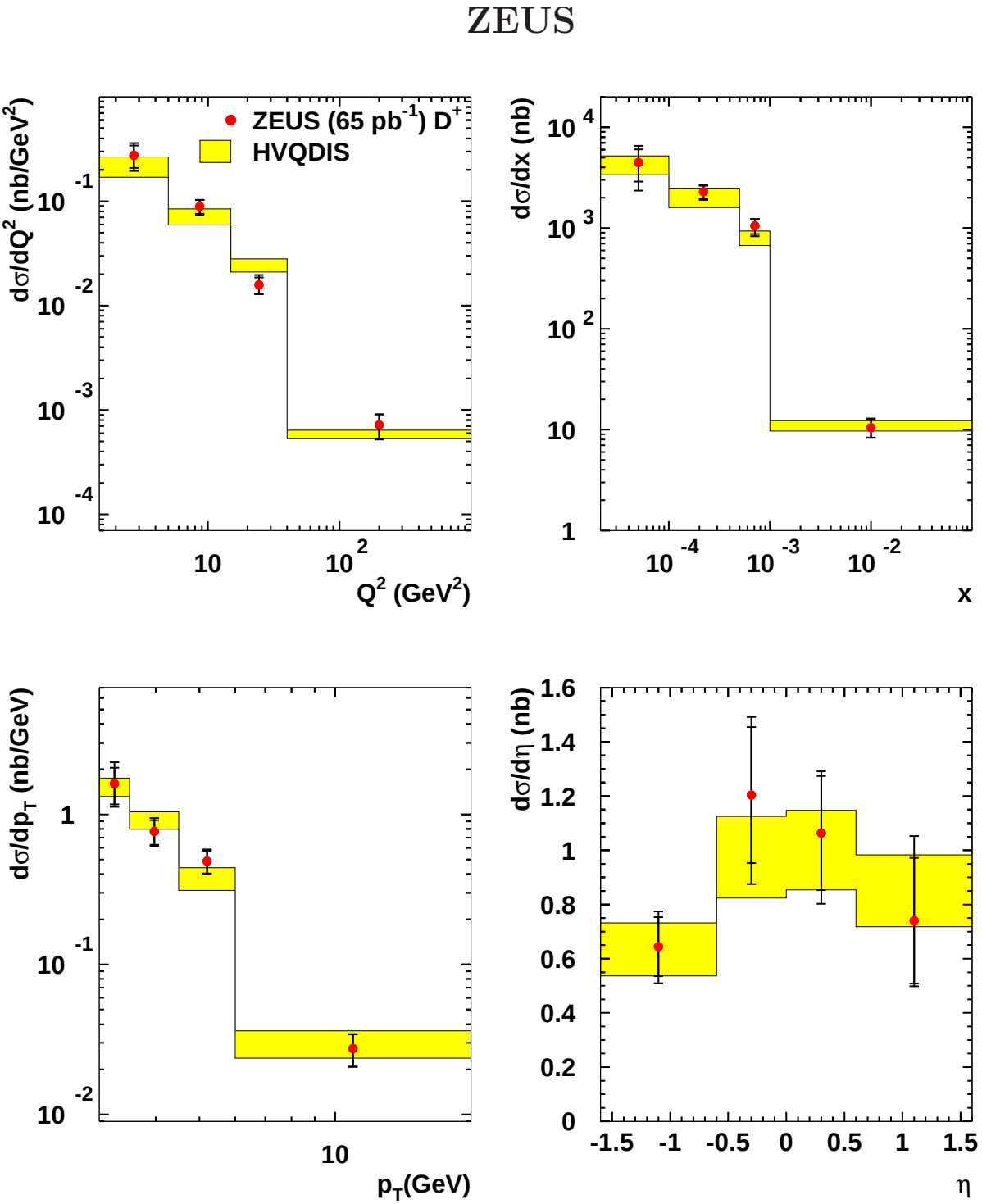

Figure 7.6: Differential D^+ cross sections as a function of Q^2, x, $p_T(D^+)$ and $\eta(D^+)$ compared to the NLO QCD calculation of HVQDIS. The inner error bars show the statistical uncertainties and the outer bars show the statistical and systematic uncertainties added in quadrature. The lower and upper NLO QCD predictions show the estimated theoretical uncertainty of the HVQDIS calculations. The data points have a further 3.6% uncertainty from the $D^+ \to K^-\pi^+\pi^+$ branching ratio.

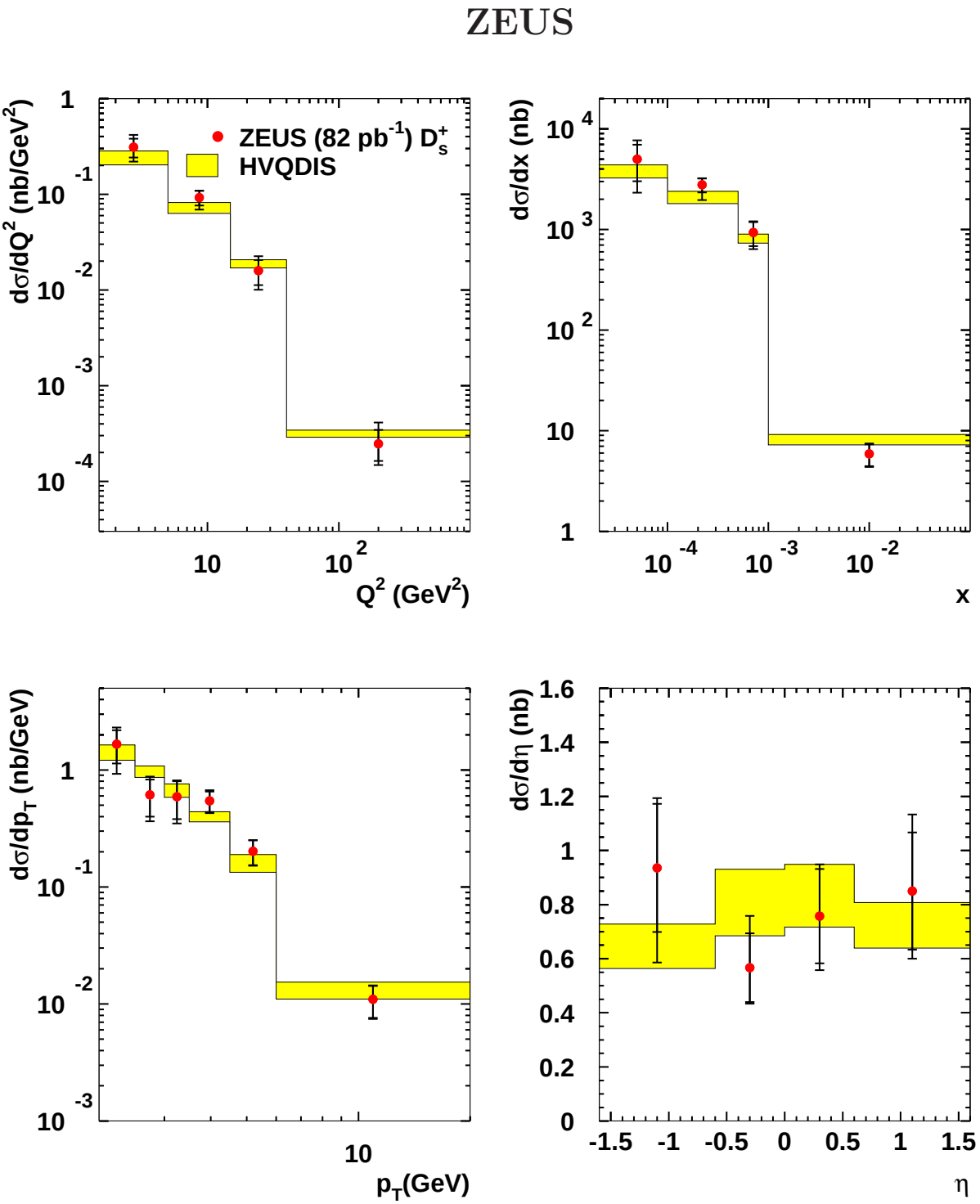

Figure 7.7: Differential D_s^+ cross sections as a function of Q^2, x, $p_T(D_s^+)$ and $\eta(D_s^+)$ compared to the NLO QCD calculation of HVQDIS. The inner error bars show the statistical uncertainties and the outer bars show the statistical and systematic uncertainties added in quadrature. The lower and upper NLO QCD predictions show the estimated theoretical uncertainty of the HVQDIS calculations. The data points have a further 13% uncertainty from the $D_s^+ \to \phi\pi^+ \to K^+K^-\pi^+$ branching ratio.

Chapter 8

Systematics Uncertainties

In this chapter the systematic uncertainties of the measured cross sections and fragmentation ratios and fractions are described. The uncertainties on the theoretical predictions are also discussed.

8.1 Systematic uncertainties of measurements

The systematic uncertainties of the measured cross sections and fragmentation ratios and fractions were determined by changing the analysis procedure and repeating all calculations.

In the measurement of fragmentation ratios and fractions the following groups of systematic uncertainty sources were considered (Table 8.1):

- $\{\delta_1\}$ the model dependence of the acceptance corrections was estimated using the HERWIG MC sample;
- $\{\delta_2\}$ the uncertainty of the beauty subtraction was determined by varying the b-quark cross section by a factor of two in the reference MC sample;
- $\{\delta_3\}$ the uncertainty of the tracking simulation was obtained by varying all momenta by $\pm 0.3\%$ which corresponds to the uncertainty in the magnetic field; and by changing the track momentum resolution and the angular resolution by $^{+20}_{-10}\%$ of their values. The asymmetric resolution variations were used since the MC signals typically had somewhat narrower widths than observed in the data;
- $\{\delta_4\}$ the uncertainty in the CAL energy scale was studied by varying in the MC the energy of the scattered e^- by $\pm 1\%$ and the energy of the hadronic system by $\pm 3\%$;

- $\{\delta_5\}$ the uncertainties related to the signal extraction procedures were studied as follows:
  - the cuts on the minimum p_T for the π and K candidates were independently raised and lowered by 10% from their nominal values,
  - the cut on the minimum p_T for the π_s was raised and lowered by 0.02 GeV (for $\sigma^{\text{tag}}(D^0)$, $\sigma^{\text{untag}}(D^0)$, $\sigma^{\text{add}}(D^{*+})$),
  - the ΔM signal region was widened symmetrically by 0.003 GeV (for $\sigma^{\text{tag}}(D^0)$, $\sigma^{\text{untag}}(D^0)$, $\sigma^{\text{add}}(D^{*+})$),
  - the $M(K\pi)$ signal region was widened and narrowed symmetrically by 0.01 GeV (for $\sigma^{\text{add}}(D^{*+})$),
  - the wrong-charge background normalisation region was changed to $0.152 < \Delta M < 0.168$ (for $\sigma^{\text{add}}(D^{*+})$);
- $\{\delta_6\}$ the uncertainties of the luminosities of the e^-p ($\pm 1.8\%$) and e^+p ($\pm 2.25\%$) data samples were included, taking into account their correlations;
- $\{\delta_7\}$ the uncertainty in the estimate of $\sigma(\Lambda_c^+)$ (see Subsection 6.3.4);
- $\{\delta_8\}$ the uncertainty in the rate of the charm-strange baryons (see Subsection 6.3.4);

Contributions from the different systematic uncertainties were calculated and added in quadrature separately for positive and negative variations. Correlated systematic uncertainties largely cancel in the calculation of the fragmentation ratios and fractions.

For the total and differential cross-section measurements discussed in Sections 7.2 and 7.3 and those used for the extraction of $F_2^{c\bar{c}}$ (Section 9.1), further sources of systematics were studied [3, 5], $\{\delta_9\}$:

- the cut on y_e was changed to $y_e \leq 0.90$;
- the cut on y_{JB} was changed to $y_{\text{JB}} \geq 0.03$;
- the cut on δ was changed to $42 \leq \delta \leq 70$ GeV;
- the cut on $|Z_{\text{vertex}}|$ was changed to $|Z_{\text{vertex}}| < 45$ cm;
- the cut on $E_{e'}$ was changed to $E_{e'} > 11$ GeV;
- the excluded region for the impact position of the scattered electron in the RCAL was increased by 1 cm in each direction;

- the electron method was used, except for cases when the scattered electron track was reconstructed by the CTD. In the latter case, the DA method, which has the best resolution at high Q^2, was used.

These estimations were made in each bin in which the differential cross sections were measured. In addition, for the lowest x bin of the differential cross section of untagged D^0, the systematic error accounted also for instabilities in the signal extraction, not encountered in any other bin. The overall systematic uncertainty was determined by adding the individual uncertainties in quadrature. Typically δ_9 was below 4%. The uncertainty on the luminosity measurement was not included in the systematic uncertainties for the differential cross sections.

Figures 8.1 and 8.2 show the effect of each systematic check in the values of the charm fragmentation fraction and ratios and in the values of the measured total cross sections, respectively.

8.2 Uncertainties on theoretical predictions

The NLO QCD predictions for D meson production are affected by the systematic uncertainties listed below. Typical values are quoted for the total cross section:

- the ZEUS PDF uncertainties were propagated from the experimental uncertainties of the fitted data ($\pm 5\%$). As an alternative parametrisation in the FFNS, the CTEQ5F3 PDF was used in HVQDIS with a charm mass of 1.3 GeV (-2%);
- the charm mass was changed simultaneously in the PDF fit and in HVQDIS by ∓ 0.15 GeV $\left(^{+8}_{-8}\%\right)$. The largest effect was at low $p_T(D)$;
- the scale was changed to $2\sqrt{Q^2 + 4m_c^2}$ and to $\max(\sqrt{Q^2/4 + m_c^2}, 2m_c)$ $\left(^{+5}_{-6}\%\right)$;
- the JETSET fragmentation (see Appendix D for details) as implemented in the previous analyses [3, 5] was used instead of the Peterson fragmentation (+5% to +20%). The largest deviations were observed for D^0 and D^+ particles at the lowest Q^2 and x.

	$\delta_1-\delta_9$ (%)	$\delta_1-\delta_8$ (%)	δ_1 (%)	δ_2 (%)	δ_3 (%)	δ_4 (%)	δ_5 (%)	δ_6 (%)	δ_7 (%)	δ_8 (%)
$\sigma^{\rm untag}(D^0)$	$^{+5.8}_{-4.7}$	$^{+5.4}_{-4.1}$	$^{+2.5}_{-0.0}$	$^{+1.7}_{-3.3}$	$^{+1.3}_{-0.9}$	$^{+1.5}_{-0.6}$	$^{+3.5}_{-0.4}$	$^{+2.2}_{-2.1}$		
$\sigma_{\rm kin}(D^+)$	$^{+6.6}_{-5.0}$	$^{+3.2}_{-4.6}$	$^{+0.6}_{-0.0}$	$^{+1.5}_{-3.1}$	$^{+1.0}_{-1.9}$	$^{+1.4}_{-0.6}$	$^{+0.0}_{-1.5}$	$^{+2.3}_{-2.2}$		
$\sigma_2(D_s^+)$	$^{+9.1}_{-7.4}$	$^{+8.8}_{-7.2}$	$^{+0.0}_{-2.0}$	$^{+0.0}_{-4.0}$	$^{+1.2}_{-0.0}$	$^{+0.5}_{-0.4}$	$^{+8.0}_{-5.1}$	$^{+2.2}_{-2.1}$		
$\sigma^{\rm tag}(D^0)$		$^{+5.6}_{-4.6}$	$^{+0.0}_{-1.5}$	$^{+1.8}_{-3.5}$	$^{+2.3}_{-1.1}$	$^{+1.5}_{-0.3}$	$^{+4.0}_{-0.8}$	$^{+2.2}_{-2.1}$		
$\sigma^{\rm add}(D^{*+})$		$^{+9.9}_{-8.9}$	$^{+0.0}_{-2.9}$	$^{+1.9}_{-3.8}$	$^{+4.2}_{-0.2}$	$^{+2.3}_{-0.5}$	$^{+8.2}_{-7.2}$	$^{+2.2}_{-2.1}$		
$\sigma_{\rm kin}(D^{*+})$		$^{+5.7}_{-4.7}$	$^{+0.0}_{-1.8}$	$^{+1.8}_{-3.6}$	$^{+2.5}_{-0.8}$	$^{+1.6}_{-0.3}$	$^{+4.0}_{-1.1}$	$^{+2.2}_{-2.1}$		
$\sigma_{\rm kin}(D_s^+)$		$^{+8.9}_{-4.9}$	$^{+2.8}_{-0.0}$	$^{+2.2}_{-4.5}$	$^{+4.0}_{-0.0}$	$^{+0.4}_{-0.1}$	$^{+6.8}_{-0.0}$	$^{+2.2}_{-2.1}$		
$R_{u/d}$		$^{+4.3}_{-1.4}$	$^{+2.7}_{-0.0}$	$^{+0.0}_{-0.1}$	$^{+1.4}_{-1.4}$	$^{+0.1}_{-0.1}$	$^{+3.0}_{-0.3}$	$^{+0.1}_{-0.1}$		
γ_s		$^{+7.9}_{-3.0}$	$^{+1.8}_{-0.0}$	$^{+0.5}_{-1.2}$	$^{+4.1}_{-0.4}$	$^{+0.6}_{-1.3}$	$^{+6.4}_{-2.4}$	$^{+0.0}_{-0.0}$		
$P_{\rm v}^d$		$^{+2.8}_{-1.4}$	$^{+0.0}_{-1.3}$	$^{+0.1}_{-0.3}$	$^{+1.4}_{-0.0}$	$^{+0.2}_{-0.0}$	$^{+2.4}_{-0.0}$	$^{+0.0}_{-0.1}$		
$\sigma_{\rm gs}$		$^{+10.3}_{-4.3}$	$^{+1.2}_{-0.0}$	$^{+1.7}_{-3.4}$	$^{+1.2}_{-0.5}$	$^{+1.4}_{-0.5}$	$^{+2.4}_{-0.5}$	$^{+2.2}_{-2.1}$	$^{+9.3}_{-0.9}$	$^{+0.4}_{-0.4}$
$f(c\to D^+)$		$^{+1.1}_{-9.2}$	$^{+0.0}_{-0.7}$	$^{+0.3}_{-0.2}$	$^{+0.1}_{-1.7}$	$^{+0.1}_{-0.2}$	$^{+0.2}_{-2.9}$	$^{+0.1}_{-0.1}$	$^{+0.9}_{-8.5}$	$^{+0.4}_{-0.4}$
$f(c\to D^0)$		$^{+1.1}_{-8.6}$	$^{+0.0}_{-0.0}$	$^{+0.0}_{-0.0}$	$^{+0.5}_{-0.4}$	$^{+0.2}_{-0.1}$	$^{+1.8}_{-0.0}$	$^{+0.0}_{-0.0}$	$^{+0.9}_{-8.5}$	$^{+0.4}_{-0.4}$
$f^{\rm untag}(c\to D^0)$		$^{+2.0}_{-8.6}$	$^{+1.0}_{-0.0}$	$^{+0.1}_{-0.0}$	$^{+0.5}_{-0.9}$	$^{+0.2}_{-0.1}$	$^{+1.4}_{-0.2}$	$^{+0.0}_{-0.0}$	$^{+0.9}_{-8.5}$	$^{+0.4}_{-0.4}$
$f(c\to D_s^+)$		$^{+7.1}_{-8.9}$	$^{+1.6}_{-0.0}$	$^{+0.5}_{-1.0}$	$^{+3.7}_{-0.3}$	$^{+0.5}_{-1.2}$	$^{+5.7}_{-2.1}$	$^{+0.0}_{-0.0}$	$^{+0.9}_{-8.5}$	$^{+0.4}_{-0.4}$
$f(c\to D^{*+})$		$^{+2.8}_{-9.1}$	$^{+0.0}_{-2.9}$	$^{+0.1}_{-0.1}$	$^{+1.5}_{-0.3}$	$^{+0.2}_{-0.0}$	$^{+2.2}_{-1.5}$	$^{+0.0}_{-0.0}$	$^{+0.9}_{-8.5}$	$^{+0.4}_{-0.4}$

Table 8.1: The systematic uncertainties resulting from δ_1-δ_9, from δ_1-δ_8, and from δ_1 to δ_8 independently (see text) for the charm hadron cross sections and charm fragmentation ratios and fractions.

Systematic identifier	Description
1	statistical error
2	RAPGAP $\rightarrow$ HERWIG
3	in MC, $\sigma(b\bar{b}) \rightarrow 2\sigma(b\bar{b})$
4	in MC, $p_T(\text{track}) \rightarrow (1+0.003)p_T(\text{track})$
5	in MC, $p_T(\text{track}) \rightarrow (1-0.003)p_T(\text{track})$
6	in MC, $E_e \rightarrow (1+0.01)E_e$
7	in MC, $E_e \rightarrow (1-0.01)E_e$
8	in MC, $E_{had} \rightarrow (1+0.03)E_{had}$
9	in MC, $E_{had} \rightarrow (1-0.03)E_{had}$
10	mimimum $p_T(\pi) \rightarrow (1+0.01)$ mimimum $p_T(\pi)$
11	mimimum $p_T(\pi) \rightarrow (1-0.01)$ mimimum $p_T(\pi)$
12	mimimum $p_T(\pi_s) \rightarrow$ mimimum $p_T(\pi_s) + 0.02$ GeV
13	mimimum $p_T(\pi_s) \rightarrow$ mimimum $p_T(\pi_s) - 0.02$ GeV
14	mimimum $p_T(K) \rightarrow (1+0.01)$ mimimum $p_T(K)$
15	mimimum $p_T(K) \rightarrow (1-0.01)$ mimimum $p_T(K)$
16	ΔM signal region $\rightarrow \Delta M$ signal region $+0.003$ GeV
17	$M(K\pi)$ signal region $\rightarrow M(K\pi)$ signal region $+0.01$ GeV
18	$M(K\pi)$ signal region $\rightarrow M(K\pi)$ signal region -0.01 GeV
19	$y_e \leq 0.95 \rightarrow y_e \leq 0.90$
20	$y_{JB} \geq 0.02 \rightarrow y_{JB} \geq 0.03$
21	$40 \leq (E-p_z) \leq 60$ GeV $\rightarrow 42 \leq (E-p_z) \leq 70$ GeV
22	$\lvert Z_{\text{vertex}} \rvert \leq 50$ cm $\rightarrow \lvert Z_{\text{vertex}} \rvert \leq 45$ cm
23	$E_e \geq 10$ GeV $\rightarrow E_e \geq 11$ GeV
24	boxcut in RCAL 26×14 cm^2 $\rightarrow 27 \times 15$ cm^2
25	reconstruction kinematic variables: Σ method $\rightarrow DA$ method

Table 8.2: Description of systematic checks in the order in which they appear in the Figures.

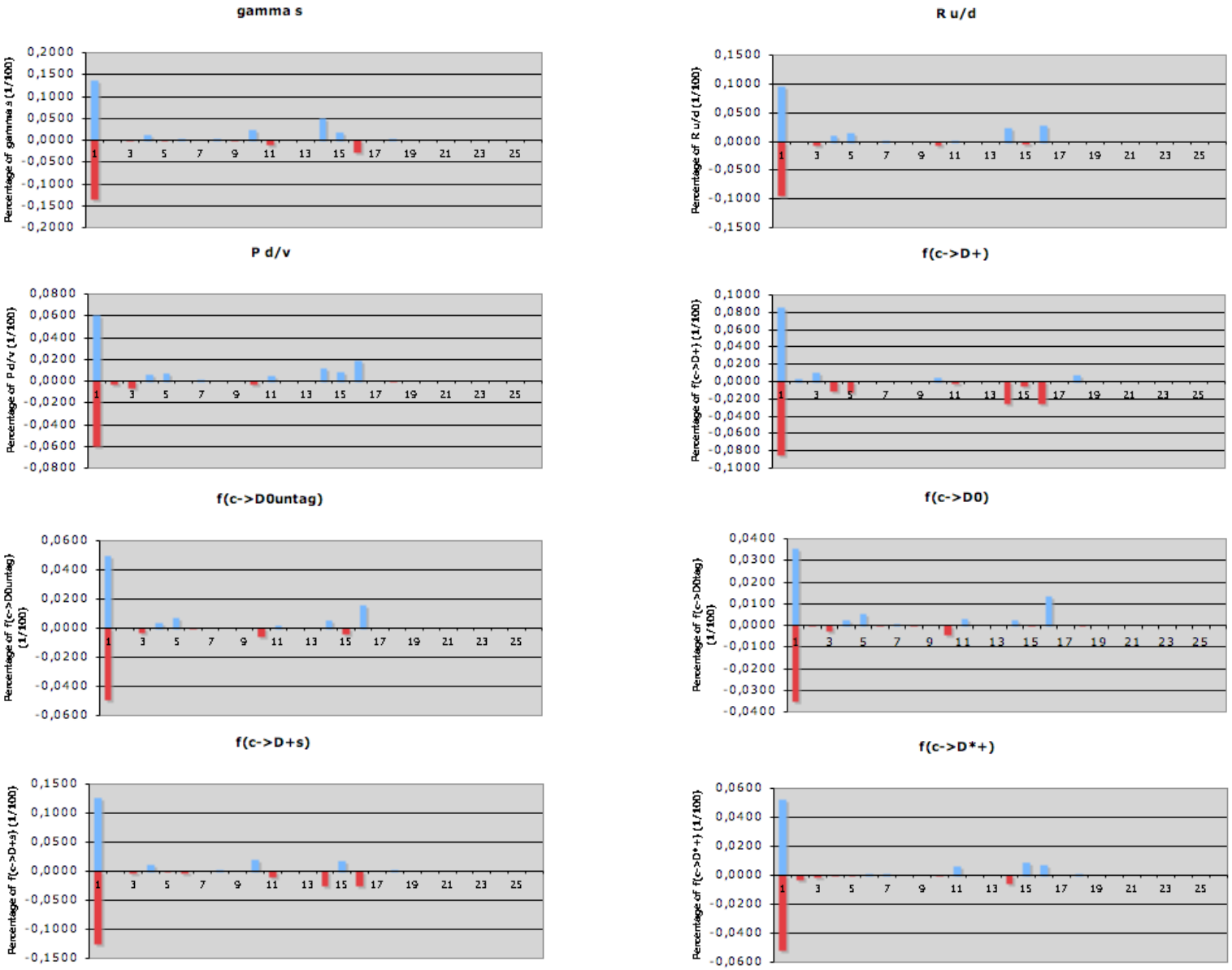

Figure 8.1: Systematic uncertainties for the charm fragmentation ratios and fractions. In each case, the first bin represents the statistical error whereas the rest of the bins represent the effect of each systematic check.

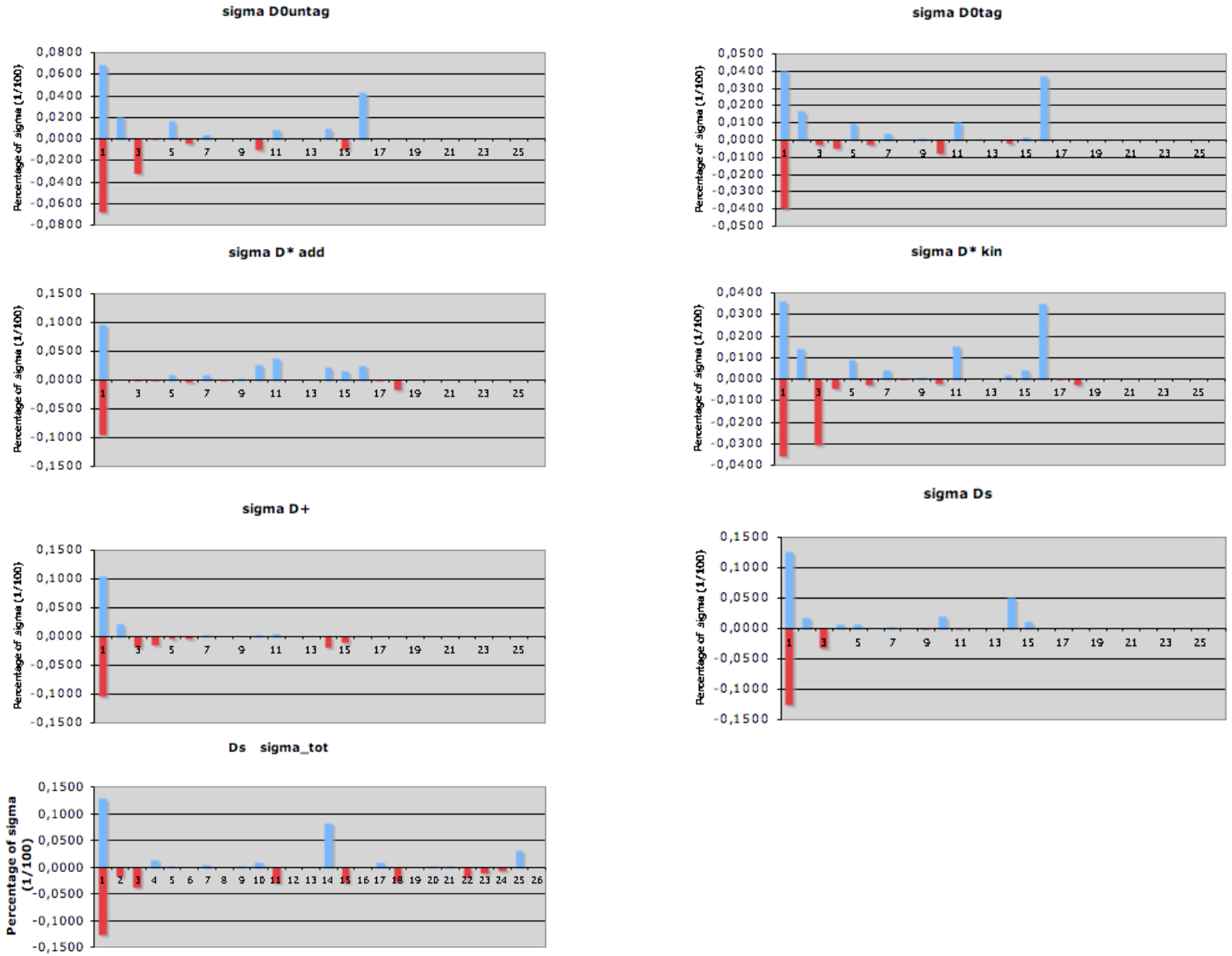

Figure 8.2: Systematic uncertainties for the measured total cross sections. The kinematic region extends up to $p_T(D) > 3$ GeV, except for the plot in the fourth row, where $p_T(D_s^+) > 2$ GeV. In each case, the first bin represents the statistical error whereas the rest of the bins represent the effect of each systematic check.

Chapter 9

Extraction of $F_2^{c\bar{c}}$

9.1 Extraction of $F_2^{c\bar{c}}$

The open charm contribution, $F_2^{c\bar{c}}$, to the proton structure-function F_2 can be defined in terms of the inclusive double-differential $c\bar{c}$ cross section in x and Q^2 by

$$\frac{d^2\sigma^{c\bar{c}}(x,Q^2)}{dxdQ^2} = \frac{2\pi\alpha^2}{xQ^4}\{[1+(1-y)^2]F_2^{c\bar{c}}(x,Q^2) - y^2 F_L^{c\bar{c}}(x,Q^2)\} \ .$$

In this analysis, the $c\bar{c}$ cross section is obtained by measuring the untagged D^0, D^+ and D_s^+ production cross sections and employing the measured hadronisation fractions $f(c \to D)$. Since only a limited kinematic region in $p_T(D)$ and $\eta(D)$ is accessible, a prescription for extrapolating to the full kinematic phase space is needed.

As reported in Chapter 7, the measured differential cross-sections are well described in the probed kinematic region. Therefore the following relation was used to extract $F_2^{c\bar{c}}$:

$$F_2^{c\bar{c}}(x_i,Q_i^2) = \frac{\sigma_{i,\mathrm{meas}}(ep \to DX)}{\sigma_{i,\mathrm{theo}}(ep \to DX)} F_{2,\mathrm{theo}}^{c\bar{c}}(x_i,Q_i^2), \tag{9.1}$$

where $\sigma_{i,\mathrm{meas}}$ is the cross section in the bin i in the measured region of $p_T(D)$ and $\eta(D)$ and $\sigma_{i,\mathrm{theo}}$ is the corresponding cross section evaluated with HVQDIS. The value of $F_{2,\mathrm{theo}}^{c\bar{c}}$ was calculated in FFNS from the NLO coefficient functions [24] using the same values of parameters as in the calculation of $\sigma_{i,\mathrm{theo}}$. The cross sections $\sigma_{i,\mathrm{meas}}(ep \to DX)$ were measured in bins of Q^2 and y (Table 9.1) and $F_2^{c\bar{c}}$ was quoted at representative Q^2 and x values for each bin (Table 9.2). The $F_2^{c\bar{c}}$ measurements obtained from each D meson were combined into a single set of measurements; the result is also shown in Table 9.2.

The extrapolation factors from the measured $p_T(D)$ and $\eta(D)$ ranges to the full phase space, as estimated using HVQDIS, were between 17 at low Q^2 and 2.5 at

high Q^2 for the D^0 and D^+ measurements. For the D_s^+, the lower p_T requirement leads to lower extrapolation factors between 5.6 and 1.9. They are all shown in Table 9.2. The uncertainty from the branching ratios was estimated by changing each branching ratio independently in the calculation by ± 1 standard deviation and adding in quadrature the resulting variations of $F_2^{c\bar{c}}$ $(^{+2.7}_{-4.1}\%)$.

The following uncertainties of the extrapolation prescription of Eq. (9.1) have been evaluated:

- using JETSET instead of the Peterson fragmentation yielded changes of $\approx$ +28%, +15% and +5% for the data points at the lowest, middle and largest Q^2 ranges, respectively;
- changing the charm mass by ± 0.15 GeV consistently in the HVQDIS calculation and in the calculation of $F_{2,\mathrm{theo}}^{c\bar{c}}$ led to differences in the extrapolation of $\pm 5\%$ at low x, low Q^2; the value decreases rapidly at higher x and higher Q^2;
- the uncertainty in the ZEUS NLO PDF fit led to uncertainties in the extracted values of $F_2^{c\bar{c}}$ typically less than 1%;
- the extrapolation factors were evaluated using the CTEQ5F3 proton PDF yielding differences compared to the nominal factors of $\approx$ +10%, +6% and +1% for the lowest, middle and largest Q^2 ranges, respectively.

As an illustration, Figure 9.1 shows the effect of each systematic check in the values of $F_2^{c\bar{c}}$ measured using untagged D^0.

The combined $F_2^{c\bar{c}}$ measurements are shown in Fig. 9.2. The quadratic addition of the extrapolation uncertainties is shown independently as a band. Also shown in Fig. 9.2 is the previous measurement [3] and the ZEUS NLO QCD fit. The two sets of data are consistent[1]. The prediction describes the data well for all Q^2 and x. The uncertainty on the theoretical prediction is that from the PDF fit propagated from the experimental uncertainties of the fitted data.

[1]The previous data were measured at $Q^2 = 4$, 18 and 130 GeV^2 and have been shifted to $Q^2 = 4.2$, 20.4 and 111.8 GeV^2 using the ZEUS NLO QCD fit.

untagged D^0

Q^2 bin (GeV^2)	y bin	σ	Δ_{stat}	Δ_{syst} (nb)
1.5, 9	0.18, 0.70	1.50	± 0.19	$^{+0.14}_{-0.16}$
	0.02, 0.18	1.03	± 0.19	$^{+0.16}_{-0.12}$
9, 44	0.20, 0.70	1.02	± 0.14	$^{+0.12}_{-0.09}$
	0.02, 0.20	1.02	± 0.14	$^{+0.12}_{-0.05}$
44, 1000	0.02, 0.70	1.03	± 0.19	$^{+0.16}_{-0.05}$

D^+

Q^2 bin (GeV^2)	y bin	σ	Δ_{stat}	Δ_{syst} (nb)
1.5, 9	0.18, 0.70	0.63	± 0.14	$^{+0.05}_{-0.10}$
	0.02, 0.18	0.65	± 0.13	$^{+0.09}_{-0.08}$
9, 44	0.20, 0.70	0.52	± 0.11	$^{+0.03}_{-0.10}$
	0.02, 0.20	0.44	± 0.11	$^{+0.06}_{-0.03}$
44, 1000	0.02, 0.70	0.61	± 0.25	$^{+0.08}_{-0.09}$

D_s^+

Q^2 bin (GeV^2)	y bin	σ	Δ_{stat}	Δ_{syst} (nb)
1.5, 9	0.18, 0.70	0.97	± 0.23	$^{+0.16}_{-0.21}$
	0.02, 0.18	0.56	± 0.15	$^{+0.11}_{-0.08}$
9, 44	0.20, 0.70	0.61	± 0.15	$^{+0.14}_{-0.15}$
	0.02, 0.20	0.29	± 0.07	$^{+0.12}_{-0.03}$
44, 1000	0.02, 0.70	0.20	± 0.11	$^{+0.08}_{-0.03}$

Table 9.1: Measured cross sections for D^0 not coming from a D^{*+}, D^+ and D_s^+ in each of the Q^2 and y bins for $p_T(D^0, D^+) > 3$ GeV, $p_T(D_s^+) > 2$ GeV and $|\eta(D)| < 1.6$. The estimated b-quark contribution of 3.1 % for D^0 and D^+ and 4.3 % for D_s^+ has been subtracted. The statistical and systematic uncertainties are shown separately. The D^0, D^+ and D_s^+ cross sections have further 1.8%, 3.6% an d 13% uncertainties from the $D^0 \to K^-\pi^+$, $D^+ \to K^-\pi^+\pi^+$ and $D_s^+ \to \phi\pi^+ \to K^+K^-\pi^+$ branching ratios, respectively.

untagged D^0

Q^2 (GeV^2)	x	$F_2^{c\bar{c}}$	Δ_{stat}	Δ_{syst}	Δ_{extrap}	factor
4.2	0.00013	0.141	± 0.017	$^{+0.013}_{-0.015}$	$^{+0.048}_{-0.013}$	8.9
	0.00061	0.090	± 0.017	$^{+0.014}_{-0.011}$	$^{+0.036}_{-0.006}$	17
20.4	0.00062	0.320	± 0.044	$^{+0.037}_{-0.029}$	$^{+0.061}_{-0.020}$	4.9
	0.00281	0.156	± 0.021	$^{+0.019}_{-0.008}$	$^{+0.041}_{-0.004}$	5.8
111.8	0.00676	0.217	± 0.039	$^{+0.033}_{-0.011}$	$^{+0.014}_{-0.002}$	2.5

D^+

Q^2 (GeV^2)	x	$F_2^{c\bar{c}}$	Δ_{stat}	Δ_{syst}	Δ_{extrap}	factor
4.2	0.00013	0.123	± 0.025	$^{+0.010}_{-0.020}$	$^{+0.037}_{-0.011}$	8.9
	0.00061	0.109	± 0.020	$^{+0.015}_{-0.014}$	$^{+0.039}_{-0.007}$	17
20.4	0.00062	0.331	± 0.067	$^{+0.016}_{-0.067}$	$^{+0.066}_{-0.021}$	4.9
	0.00281	0.130	± 0.039	$^{+0.017}_{-0.009}$	$^{+0.030}_{-0.003}$	5.8
111.8	0.00676	0.293	± 0.124	$^{+0.037}_{-0.041}$	$^{+0.021}_{-0.003}$	2.5

D_s^+

Q^2 (GeV^2)	x	$F_2^{c\bar{c}}$	Δ_{stat}	Δ_{syst}	Δ_{extrap}	factor
4.2	0.00013	0.221	± 0.044	$^{+0.037}_{-0.048}$	$^{+0.036}_{-0.016}$	4.3
	0.00061	0.075	± 0.017	$^{+0.016}_{-0.011}$	$^{+0.019}_{-0.004}$	5.6
20.4	0.00062	0.470	± 0.100	$^{+0.109}_{-0.112}$	$^{+0.037}_{-0.017}$	2.8
	0.00281	0.100	± 0.022	$^{+0.043}_{-0.009}$	$^{+0.013}_{-0.001}$	2.9
111.8	0.00676	0.179	± 0.058	$^{+0.075}_{-0.025}$	$^{+0.013}_{-0.001}$	1.9

Combined

Q^2 (GeV^2)	x	$F_2^{c\bar{c}}$	Δ_{stat}	Δ_{syst}	Δ_{extrap}
4.2	0.00013	0.144	± 0.014	$^{+0.022}_{-0.015}$	$^{+0.045}_{-0.013}$
	0.00061	0.090	± 0.010	$^{+0.010}_{-0.004}$	$^{+0.029}_{-0.005}$
20.4	0.00062	0.341	± 0.035	$^{+0.046}_{-0.042}$	$^{+0.063}_{-0.021}$
	0.00281	0.132	± 0.014	$^{+0.024}_{-0.005}$	$^{+0.024}_{-0.001}$
111.8	0.00676	0.211	± 0.032	$^{+0.044}_{-0.013}$	$^{+0.013}_{-0.002}$

Table 9.2: The extracted values of $F_2^{c\bar{c}}$ from the production cross sections of D^0 not coming from D^{*+}, D^+ and D_s^+ and the combination of the m at each Q^2 and x value. The statistical, systematic and extrapolation uncertainties are shown separa tely. The values of the extrapolation factor used to correct the full $p_T(D)$ and $\eta(D)$ phase space are also shown. All the extracted $F_2^{c\bar{c}}$ values have a further $+2.7\%$ -4.1% uncertainty from the $D^0 \to K^-\pi^+$, $D^+ \to K^-\pi^+\pi^+$ and $D_s^+ \to \phi\pi^+ \to K^+K^-\pi^+$ branching ratios and the $f(c \to \Lambda_c^+)$ value.

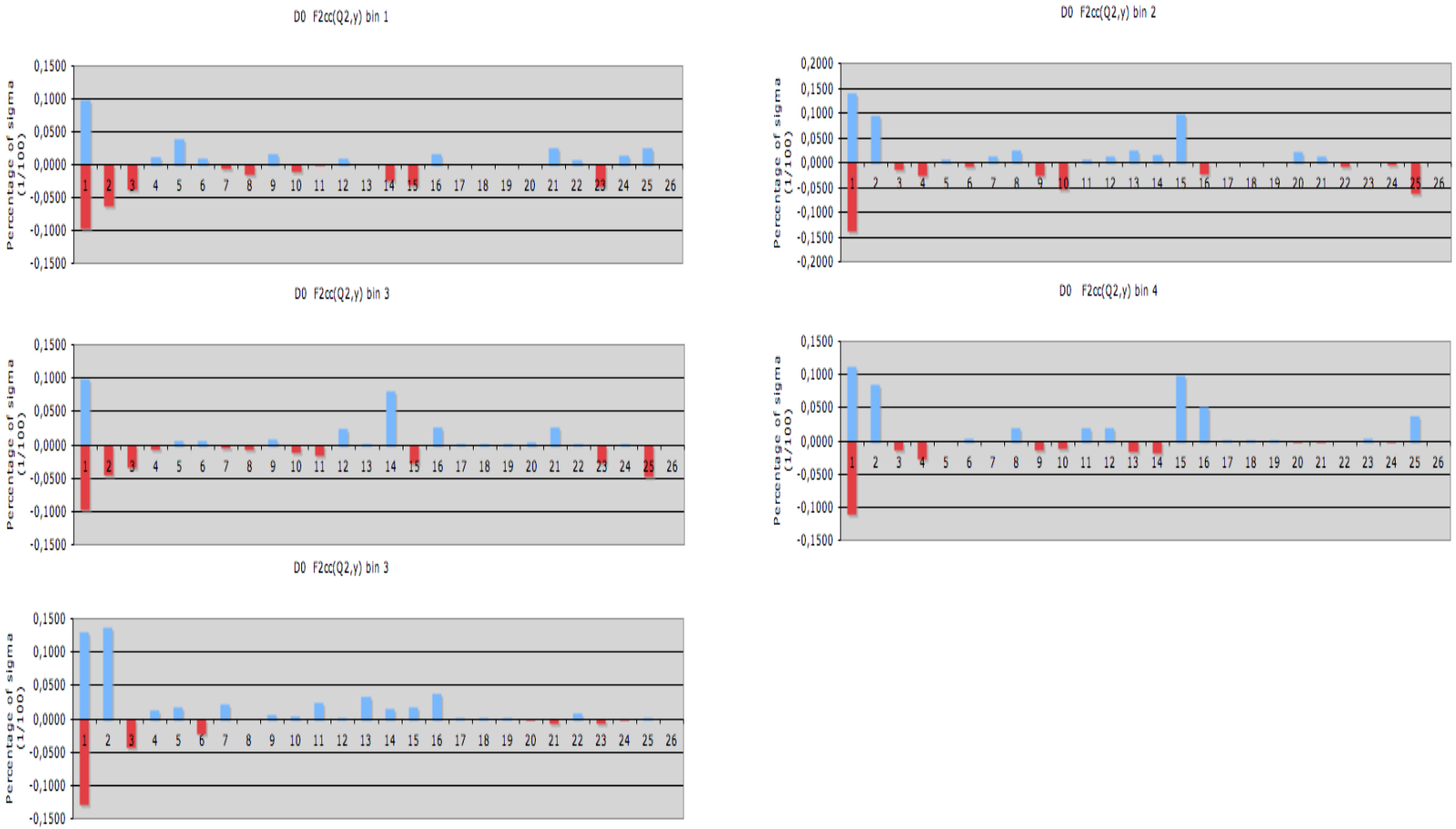

Figure 9.1: Systematic uncertainties for $F_2^{c\bar{c}}$ measured in bins of (Q^2, y) using untagged D^0. In each case, the first bin represents the statistical error whereas the rest of the bins represent the effect of each systematic check.

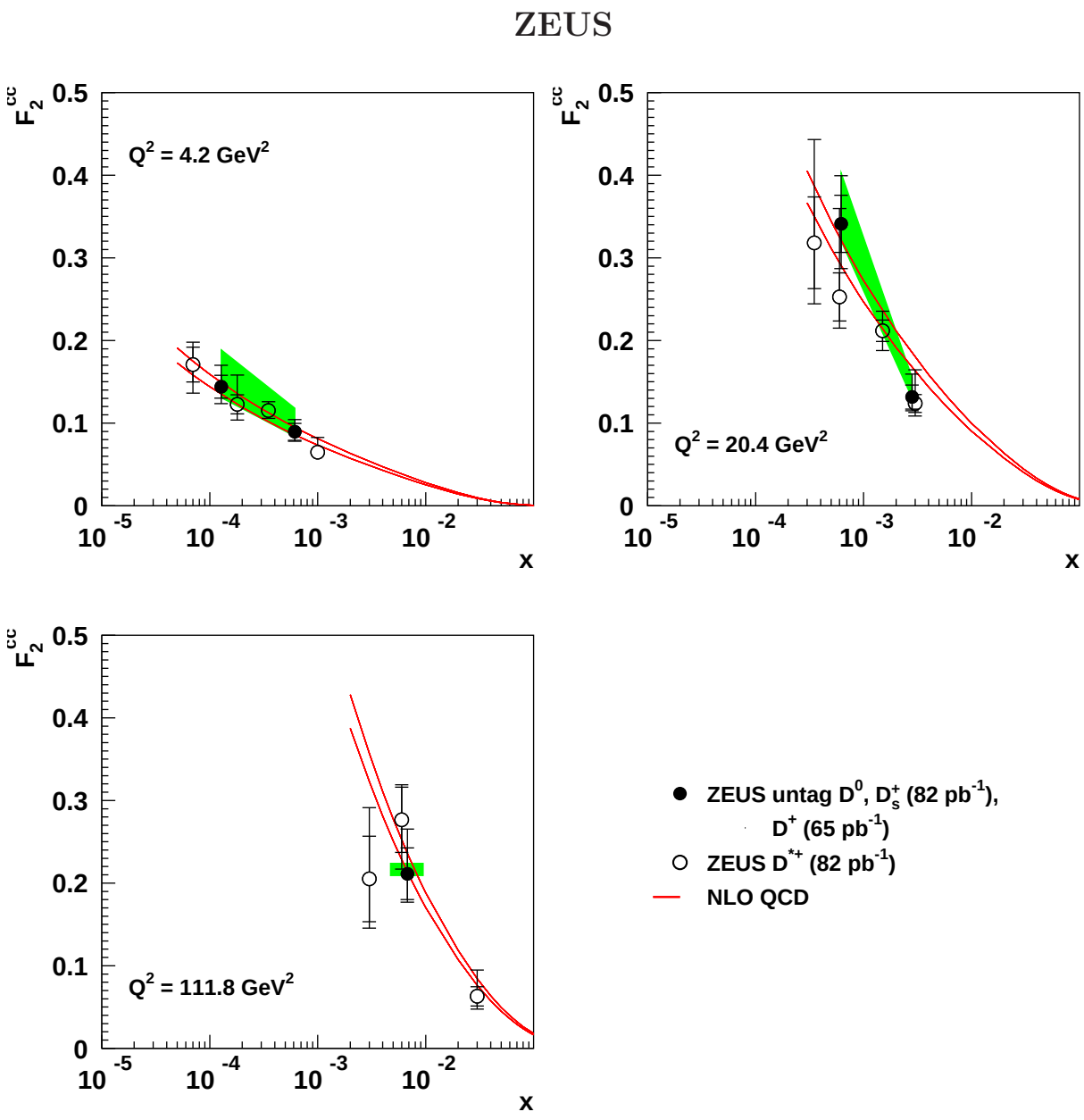

Figure 9.2: The measured $F_2^{c\bar{c}}$ as a function of x for three Q^2 bins. The current data are compared with the previous ZEUS measurement [3]. The data are shown with statistical uncertainties (inner bars) and statistical and systematic uncertainties added in quadrature (outer bars). All measured $F_2^{c\bar{c}}$ values have a further +2.7% -4.1% uncertainty coming from the current experimental uncertainty from the $D^0 \to K^-\pi^+$, $D^+ \to K^-\pi^+\pi^+$ and $D_s^+ \to \phi\pi^+ \to K^+K^-\pi^+$ branching ratios and the $f(c \to \Lambda_c^+)$ value. The shaded band corresponds to the estimated theoretical uncertainty in the extrapolation. The lower and upper curves show the ZEUS NLO QCD fit [24] uncertainty propagated from the experimental uncertainties of the fitted data.

Chapter 10

Conclusions

The production of the charm mesons D^{*+}, D^0, D^+ and D_s^+ has been measured with the ZEUS detector in the kinematic range $1.5 < Q^2 < 1000\,\mathrm{GeV}^2$, $0.02 < y < 0.7$, $p_T(D^*+, D^0, D^+) > 3\,\mathrm{GeV}$, $p_T(D_s^+) > 2\,\mathrm{GeV}$ and $|\eta(D)| < 1.6$.

The cross sections have been used to determine the charm fragmentation ratios and fractions. The ratio of neutral to charged D-meson production, $R_{u/d}$, is compatible with unity, i.e. it is consistent with isospin invariance, which implies that u and d quarks are produced equally in charm fragmentation. The strangeness-suppression factor in charm fragmentation, γ_s, was measured to be about 20%. The fraction of charged D mesons produced in a vector state, P_{v}^d, was found to be smaller than the naive spin-counting prediction of 0.75. The fraction of c quarks hadronising as D^{*+}, D^0, D^+ and D_s^+ mesons have been calculated. The measured $R_{u/d}$, γ_s, P_{v}^d and open charm fragmentation fractions are consistent with those obtained in charm photoproduction and in e^+e^- annihilation. These measurements generally support the hypothesis that fragmentation proceeds independently of the hard sub-process.

The measured D^0, D^+ and D_s^+ differential cross sections were compared to the predictions of NLO QCD with the proton PDFs extracted from inclusive DIS data. A good description was found.

The double-differential cross section in y and Q^2 has been used to extract the open charm contribution to F_2, by using the NLO QCD calculation to extrapolate outside the measured $p_T(D)$ and $\eta(D)$ regions. The $F_2^{c\bar{c}}$ values obtained from the different D mesons agree with previous results where a D^{*+} meson was tagged.

Chapter 11

Conclusiones

La producción de mesones encantados D^{*+}, D^0, D^+ y D_s^+ ha sido medida con el detector ZEUS en el rango cinemático $1.5 < Q^2 < 1000\,\mathrm{GeV}^2$, $0.02 < y < 0.7$, $p_T(D^*+, D^0, D^+) > 3\,\mathrm{GeV}$, $p_T(D_s^+) > 2\,\mathrm{GeV}$ y $|\eta(D)| < 1.6$.

Las secciones eficaces han sido usadas para determinar las razones y fracciones de fragmentacion del quark charm. La razón de producción de mesones cargados respecto de mesones neutros, $R_{u/d}$, es compatible con la unidad, esto es, es compatible con la invariancia de isospín, que implica igualdad en la producción de quarks u y d en la fragmentación de charm. Para el factor de supresión de extrañeza en fragmentación de charm, γ_s, el valor medido se situó en torno al 20%. Para la fracción de mesones cargados producidos en estado vectorial, P_{v}^d, el valor medido fue menor que el proporcionado por la predicción naive basada en contaje de espines, 0.75. La fracciones de fragmentación de quarks c que se hadronizan en los mesones D^{*+}, D^0, D^+ y D_s^+ fueron medidas. Los valores medidos de $R_{u/d}$, γ_s, P_{v}^d y fracciones de fragmentación de charm son consistentes con los valores medidos en fotoproducción y en aniquilaciones e^+e^-. Estas medidas sostienen en general la hipótesis de que el proceso de fragmentación es independiende del sub-proceso duro.

Las secciones eficaces diferenciales medidas para la producción de D^0, D^+ and D_s^+ fueron comparadas con las predicciones de NLO QCD con la PDFs de protón extraida de datos inclusivos DIS. Se observó un buena descripción.

Las secciones eficaces diferenciales dobles en y y Q^2 han sido usadas para extraer la contribución de charm a F_2, usando los calculos NLO QCD para extrapolar mas allá de la región cinematica medida en $p_T(D)$ y $\eta(D)$. Los valores obtenidos de $F_2^{c\bar{c}}$ usando los diferentes mesones D están en acuerdo con los resultados previos que usan el meson D^{*+} para identificar charm.

Appendix A

Boosting

In this appendix we give details about how to boost to the rest frame of a real (mass positive definite) particle.

Notation and conventions

- For the four-momentun of a particle we write $p = (p^0, p^1, p^2, p^3) = (p^0, \boldsymbol{p})$. In the components p^a of a four-vector, the index a can take any of the values $a = 0, 1, 2, 3$, unless it is explicitly said.

- We use the standard metric in Minkowski space with diagonal elements

$$g = \text{diag}(+1, -1, -1, -1) \ ,$$

  and zero for the rest of the elements.

  With this choice, the square of the four momentum takes the form

$$p^2 = p^T \ g \ p = (p^0)^2 - (\boldsymbol{p})^2 \ .$$

- The Lorentz group is defined as the set of real linear transformations over the Minkowski space that leave invariant the square of the four-momentum.

$$L = \{\Lambda \in GL(4, \mathbb{R}) \mid p' = \Lambda p \text{ with } p'^2 = p^2\} \ .$$

  Therefore they satisfy the equation

$$\Lambda^T \ g \ \Lambda = g \ .$$

  From this relation the inverse of any Lorenzt transformation can be computed in a strightforward way :

$$\Lambda^{-1} = g^{-1} \ \Lambda^T \ g \ . \tag{A.1}$$

The problem

Let us consider the four-momentum p of a massive particle $\mathbb{Q}$ in the lab frame:

$$p = (p^0, p^1, p^2, p^3) \ .$$

We will write k for the four-momentum of the same particle in its rest frame

$$k = (m, 0, 0, 0) \ ,$$

where m is the mass of the particle.

Our task consists of finding a Lorentz transformation $L(p)$ which maps k onto p.

$$p = L(p) \ k \ . \tag{A.2}$$

Computation of the matrix $L(p)$

The solutions $L(p)$ to Eq. A.2 are not unique. If $L(p)$ is a solution, then

$$\bar{L}(p) = R(\hat{\mathbf{p}}, \phi) \ L(p)$$

is also a solution. Here $R(\hat{\mathbf{p}}, \phi)$ is any 3-dimensional rotation of axe defined by the unitary vector $\hat{\mathbf{p}} = \mathbf{p}/\|\mathbf{p}\|$ and arbitrary angle ϕ. Due to this freedom, we have to do a specific choice for $L(p)$. This will be set to

$$L(p) = \begin{pmatrix} L^0{}_0 & L^0{}_1 & L^0{}_2 & L^0{}_3 \\ L^1{}_0 & L^1{}_1 & L^1{}_2 & L^1{}_3 \\ L^2{}_0 & L^2{}_1 & L^2{}_2 & L^2{}_3 \\ L^3{}_0 & L^3{}_1 & L^3{}_2 & L^3{}_3 \end{pmatrix}$$

with its elements given by [84]

$$\begin{aligned} L^i{}_k &= \delta_{ik} + (\gamma - 1)\hat{p}_i\hat{p}_k \qquad i,k = 1,2,3 \\ L^i{}_0 &= L^0{}_i = \hat{p}_i\sqrt{\gamma^2 - 1} \qquad i = 1,2,3 \\ L^0{}_0 &= \gamma \end{aligned}$$

Here $\hat{p}_i$ with $i = 1, 2, 3$ are the components of the unitary vector along the $\boldsymbol{p}$ direction, and the factor γ is defined by

$$\gamma = \frac{p^0}{m} = \frac{\sqrt{\mathbf{p}^2 + m^2}}{m} \ .$$

The matrix previously defined belongs to the Lorentz group. The proof is stright-forward just by taking matrix elements in the equation $L(p)^T \ g \ L(p) = g$, so it is ommited here.

We can easily check that $L(p)$ defined in this way actually maps the rest four-momentum k onto the lab four-momentum p. PROOF :

$$(L(p)\ k)^a = L(p)^a{}_b\ k^b = L(p)^a{}_0\ k^0 = L(p)^a{}_0\ m$$

- For $a = 0$ we have

$$(L(p)\ k)^0 = L(p)^0{}_0\ m = \gamma m = \frac{p^0}{m} m = p^0$$

- For $a = i = 1, 2, 3$ we have

$$(L(p)\ k)^i = L(p)^i{}_0\ m = (\hat{p}_i \sqrt{\gamma^2 - 1}) m = \hat{p}_i \frac{\|\boldsymbol{p}\|}{m} m = p_i$$

Q.E.D.

According to what Eq. A.1, the inverse of $L(p)$ can be computed in a straightforward way

$$L^{-1}(p) = g^{-1}\ L^T(p)\ g = \begin{pmatrix} L^0{}_0 & -L^1{}_0 & -L^2{}_0 & -L^3{}_0 \\ -L^0{}_1 & L^1{}_1 & L^2{}_1 & L^3{}_1 \\ -L^0{}_2 & L^1{}_2 & L^2{}_2 & L^2{}_2 \\ -L^0{}_3 & L^1{}_3 & L^2{}_3 & L^3{}_3 \end{pmatrix} \tag{A.3}$$

Boosting

Let $p_1, \ldots p_n$ be the four-momenta of a system of particles in the lab frame. Then, their four-momenta $p'_1, \ldots p'_n$ in rest frame of the the particle $\mathbb{Q}$ are given by:

$$\begin{aligned} p_1 \to p'_1 &= L^{-1}(p)\ p_1 \\ &\ldots \\ p_n \to p'_n &= L^{-1}(p)\ p_n\ , \end{aligned}$$

where the matrix $L^{-1}(p)$ is given by Eq. A.3.

Appendix B

Modified Gaussian

In this appendix we detail how the number of reconstructed D-mesons was extracted by fitting their mass distributions to a modified gaussian function.

B.1 Fit with a function

Let h_i be the number of entries in the i-bin of the mass distribution histogram corresponding to the production of the particle D in some kinematic region. In each bin, we have

$$h_i = s_i + b_i \ ,$$

where s_i and b_i are the number of signal and background combinations in the i-bin, respectively. The quantities s_i and b_i are not known independendently, but only their sum h_i. The number of D mesons, i.e. the total number of signal combinations in the mass distribution, is the quantity we want to estimate:

$$N = \sum_i s_i \ ,$$

where the sum is extended to all bins in the mass distribution histogram. One way to give and estimation of N is by means of a fit.

Let us assume that we have found a function $h(x)$ which "describes well" the shape of the mass distribution. To simplify the notation, we do not write the dependence with respect to the free parameters $(p_1, p_2, p_3, \ldots p_n)$, whose values are determined by minimising $\chi^2(p_1, p_2, p_3, \ldots p_n)$ with a fit.

The function $h(x)$ splits in two pieces

$$h(x) = s(x) + b(x) \ ,$$

with $s(x)$ and $b(x)$ modelling signal and background shapes, respectively. Then, the

number of D-mesons is estimated according to

$$N = \sum_i s_i = \frac{1}{d} \sum_i d\ s_i \sim \frac{1}{d} \int_{-\infty}^{\infty} dx\ s(x)\ , \tag{B.1}$$

where d is the bin width in the mass distribution histogram.

B.2 Fit with a modified gaussian

Usually, the function describing the signal $s(x)$ is expected to exhibit gaussian behaviour

$$s(x) \to g(x; d, p_1, p_2, p_3) = \frac{d\ p_1}{\sqrt{2\pi}\ p_3} \exp\left\{ -\frac{1}{2} \left(\frac{x - p_2}{p_3} \right)^2 \right\}\ ,$$

where the bin width d has been explicitly extracted and (p_1, p_2, p_3) are free parameters.

However, due to differences in the reconstruction of positive and negative tracks at low momentum, deviations from gaussian behaviour are observed. A "modified" gaussian function is then proposed

$$s(x) \to g_m(x; d, p_1, p_2, p_3) = \frac{d\ p_1}{\sqrt{2\pi}\ p_3} \exp\left\{ -\frac{1}{2} x_s^{1+\frac{1}{1+0.5x_s}} \right\}\ , \tag{B.2}$$

with

$$x_s = |\frac{x - p_2}{p_3}|\ .$$

Then, according to Eq. B.1, the estimation of the number D-mesons would be

$$N = \frac{1}{d} A\ , \qquad A \equiv \int_{-\infty}^{\infty} dx\ g_m(x; d, p_1, p_2, p_3)\ .$$

Performing the change of variables in the integral

$$x \to x' = \frac{x - p_2}{p_3}$$

we see that

$$A = d\ p_1\ A_0\ , \qquad A_0 \equiv \int_{-\infty}^{\infty} dx\ g_m(x; 1, 1, 0, 1)\ ,$$

and therefore

$$N = p_1\ A_0\ . \tag{B.3}$$

The integral A_0 needs to be evaluated. However, the function $g_m(x)$ can not be analytically integrated. Therefore, we must perform an aproximate numerical integration in a finite interval $(-M, M)$, with $M > 1$, and give an upper bound to the error due to truncating

$$A_0 = A_0^{approx} + R,$$

with

$$A_0^{approx} = \int_{-M}^{+M} dx\ g_m(x;1,1,0,1) \qquad R = 2\int_{M}^{\infty} dx\ g_m(x;1,1,0,1)\ .$$

The calculation of A_0^{approx} can be done using a suitable numerical method (i.e, montecarlo integration), with arbitrary precision. To give an upper bound to R we note that

$$\exp\left\{-\frac{1}{2}x^{1+\frac{1}{1+0.5x}}\right\} < \exp\left\{-\frac{1}{2}x\right\} \qquad x > 1\ ,$$

so

$$R < \frac{2}{\sqrt{2\pi}}\int_{M}^{\infty} dx\ \exp\left\{-\frac{1}{2}x\right\} = \frac{4}{\sqrt{2\pi}}e^{-M/2} \qquad M > 1\ .$$

Notice that having found an upper bound to R, we have proved that the modified gaussian function represents a true probability distribution, i.e. it can be normalised. Therefore, calculating A_0^{approx} with enough precision and taking M sufficiently large, we can cansider A_0 as a constant and neglect $\Delta A_0/A_0$ against $\Delta p_1/p_1$ in Eq. B.3. Our computation gives

$$A_0 = 1.217719399\ . \tag{B.4}$$

In summary, the number of reconstructed D-mesons and its error are given by

$$\boxed{N = A_0\ p_1 \qquad \Delta N = A_0\ \Delta p_1}$$

where the normalisation factor A_0 is given by Eq. B.4 and the values of the parameter p_1 and its error Δp_1 are extracted from a fit to the mass distribution using the modified gaussian funcion parametrised as in Eq. B.2 to model the signal shape.

Appendix C

Wrong Charge Background Estimator

In this appendix we describe an alternative method to the fit which is currently used to estimate the background in D^{*+} production.

C.1 Wrong charge subtraction

The reconstruction of D^{*+} mesons was presented in Section 4.2. The ΔM mass distribution is filled with those triplets of tracks in the charge combination (K^-, π^+, π_s^+). The set of these triplets is call the set of "right charge" combinations. Their elements can be either signal or background. On the other hand, triplets of tracks in the charge combination (K^+, π^+, π_s^-) can only be background. The set of these triplets is called the set of "wrong charge" combinations.

The wrong charge subtraction method assumes that right charge background candidates distribute in the phase space in the same way that wrong charge events, up to normalisation. An estimation to the number of D^{*+} mesons in the signal region is then given by

$$\boxed{N = N_A - N_B \cdot f \qquad f = \frac{N_C}{N_D}}$$

with N_A and N_B right and wrong charge events in the signal region, whereas N_C and N_D are the analogous quantities in a normalization region away from the signal. Standard error propagation gives, for the statistical error associated to N:

$$\boxed{\Delta N = \sqrt{N_A + \frac{1}{(N_D)^2}\left\{N_B N_C \left(N_B + N_C + \frac{N_B N_C}{N_D}\right)\right\}}\ .}$$

Appendix D

Jetset Fragmentation

D.1 Models for fragmentation

Peterson model for the fragmentation $c \to D$ gives no transverse momentum to the produced D meson relative to the direction of the momentum carried by the parent c quark. In Monte Carlo models (RAPGAP) fragmentation is treated in a more complicated way. In addition to the Peterson model, the Lund model based on colour strings is used to model the fragmentation. In these treatments, the produced D meson has a transverse momentum relative to the direction of the parent c quark due to the large colour flow from the c quark to the proton remnant. As a consecuence, the D meson are produced more forward than the parent c quark [38].

Therefore, as an alternative, a Monte Carlo based bin-by-bin correction procedure was employed to treat fragmentation. Explicitly, the theoretical predictions for the D mesons cross sections were obtained as follows:

$$\left(\frac{d\sigma(D)}{dX}\right)_{NLO+MC} = \left(\frac{d\sigma(c\bar{c})}{dX}\right)_{NLO} \cdot f(c \to D) \cdot \frac{N(D)_{MC}}{N(c)_{MC}}$$

where

- X is a generic variable under study,
- $f(c \to D)$ is the corresponding measured fragmentation fraction,
- $N(D)_{MC}$ is the number of D mesons found in the MC sample which lie in the kinematic region of the measurement [1] and in the bin dX,
- $N(c)_{MC}$ is the number of c quark decaying to a D meson found in the MC sample which lie in the kinematic region of the measurement and in the bin dX.

[1] $1.5 < Q^2 < 1000\,\mathrm{GeV}^2$, $0.02 < y < 0.7$, $p_T > 3.0\,\mathrm{GeV}$ (also $p_T > 2.0\,\mathrm{GeV}$ for D_s^+) and $|\eta| < 1.6$.

The factor $\frac{N(D)_{MC}}{N(c)_{MC}}$ accounts for the migrations occured in the bin dX.

References

[1] For a review see J.C. Collins, D.E. Soper and G. Sterman, *Factorization of Hard Process in QCD*, in "Perturbative Quantum Chromodynamics", A.H. Mueller (ed.). World Scientific, Singapore, 1989.

[2] ZEUS Coll., S. Chekanov et al., Eur. Phys. J. **C 44**, 351 (2005).

[3] ZEUS Coll., S. Chekanov et al., Phys. Rev. **D 69**, 012004 (2004).

[4] H1 Coll., A. Aktas et al., Eur. Phys. J. **C 38**, 447 (2005).

[5] ZEUS Coll., J. Breitweg et al., Eur. Phys. J. **C 12**, 35 (2000).

[6] ZEUS Coll., J. Breitweg et al., Phys. Lett. **B 407**, 402 (1997).

[7] H1 Coll., C. Adloff et al., Phys. Lett. **B 528**, 199 (2002).

[8] H1 Coll., C. Adloff et al., Z. Phys. **C 72**, 593 (1996).

[9] H1 Coll., C. Adloff et al., Nucl. Phys. **B 545**, 21 (1999).

[10] H1 Coll., A. Aktas et al., Eur. Phys. J. **C 40**, 349 (2005).

[11] ZEUS Coll., J. Breitweg et al., Phys. Lett. **B 481**, 213 (2000).

[12] ZEUS Coll., J. Breitweg et al., Eur. Phys. J. **C 6**, 67 (1999).

[13] H1 Coll., A. Aktas et al., Phys. Lett. **B 621**, 56 (2005).

[14] H1 Coll., S. Aid et al., Nucl. Phys. **B 472**, 32 (1996).

[15] ZEUS Coll., J. Breitweg et al., Phys. Lett. **B 401**, 192 (1997).

[16] ZEUS Coll., S. Chekanov, et al., JHEP07(2007)074.

[17] ZEUS Coll., *Measurements of Charm Production Cross Sections and Fragmentation Fractions in DIS at HERA*. Contribution to ICHEP06, 2006.

[18] ZEUS Coll., *Measurement of D mesons production in deep inelastic scattering at HERA*. Contribution to EPS07, 2007.

[19] E.D. Bloom et al., Phys. Rev. Lett. **23**, 930 (1969).

[20] H.L. Lai and W.K. Tung, Z. Phys. **C 74**, 463 (1997).

[21] R.G. Roberts, *The Structure of the Proton – Deep Inelastic Scattering.* Cambridge University Press, Cambridge, 1990.

[22] R.P. Feynman, *Photon-Hadron Interactions.* Benjamin, New York, 1972.

[23] R.P. Feynman, Phys. Rev. Lett. **23**, 1415 (1969).

[24] ZEUS Coll., S. Chekanov et al., Phys. Rev. **D 67**, 012007 (2003);
Public access to ZEUS 2002 PDFs, available on
`http://www-pnp.physics.ox.ac.uk/~cooper/zeus2002.html`.

[25] ZEUS Coll., *Measurement of charm production in DIS via semileptonic decays.* Contribution to ICHEP2000, Abstract 853, 2000.

[26] W. Verkerke, *Measurement of Charm Production in Deep Inelastic Scattering.* Ph.D. Thesis, University of Amsterdam, 1998.

[27] S. Schagen, *Charm in the Proton.* Ph.D. Thesis, University of Amsterdam, 2004.

[28] ZEUS Coll., *Study of inclusive D^0 photoproduction at HERA.* Contribution to EPS2001, Abstract 501, 2001.

[29] ZEUS Coll., J. Breitweg et al., Z. Phys. **C 75**, 215 (1997).

[30] ZEUS Coll., J. Breitweg et al., Z. Phys. **C 76**, 599 (1997).

[31] Chekanov, S. et al., Eur. Phys. J. **C44**, 13 (2005).

[32] B.W. Harris and J. Smith, Nucl. Phys. **B 452**, 109 (1995);
B.W. Harris and J. Smith, Phys. Lett. **B 353**, 535 (1995). Erratum-ibid **B 359** (1995) 423.

[33] B.W. Harris and J. Smith, Phys. Rev. **D 57**, 2806 (1998).

[34] E. Laenen et al., Nucl. Phys. **B 392**, 162 (1993);
E. Laenen et al., Nucl. Phys. **B 392**, 229 (1993).

[35] Chubakin, A. et al., Eur. Phys. J. **C18**, 547 (2001).

[36] R. Hall-Wilton, *Diffractive and non-Difractive Charm Production in Deep Inelastic Scattering at HERA.* Ph.D. Thesis, University of Bristol, 1999.

[37] J.P. Fernández, *Estudio de la producción de mesones con extrañeza y encanto en colisiones ep en HERA con el detector ZEUS*. Ph.D. Thesis, Universidad Autónoma de Madrid, 1998.

[38] I. Redondo, *Charm Electroproduction at HERA*. Ph.D. Thesis, Universidad Autónoma de Madrid, 2001.

[39] C. Peterson et al., Phys. Rev. **D 27**, 105 (1983).

[40] HERMES Coll., *Technical Design Report*, 1993.

[41] HERA-B Coll., *Technical Design Report*. DESY-PRC 95/01.

[42] DESY, *Annual Report*, 1994.

[43] ZEUS Coll., *The ZEUS Detector*. Status Report (unpublished), DESY, 1993.

[44] B. Foster et al., Nucl. Inst. Meth. **A 338**, 254 (1994).

[45] M. Derrick et al., Nucl. Instr. and Meth. **A 309**, 77 (1991).

[46] A. Andersen et al., Nucl. Instr. and Meth. **A 309**, 101 (1991).

[47] B. Bernstein et al., Nucl. Instr. and Meth. **A 336**, 23 (1993).

[48] H. Bethe and W. Heitler, Proc. Roy. Soc. Lond. **A146**, 83 (1934).

[49] J. Andruskow et al.. DESY 92-066, 1992.

[50] K. Piotrkowski et al.. DESY F35D-93-06, 1993.

[51] C. Youngman, *The ZEUS Data Acquisition System*. DESY 92-150A.

[52] W.H. Smith et al., *The ZEUS Trigger System*. ZEUS-note 89-084.

[53] H. Uigterwall, *The Global Second Level Trigger for ZEUS*. Ph.D. Thesis, University of Amsterdam, 1992.

[54] S.M Fisher et al., *ADAMO: User's guide*. CERN, 1993.

[55] R. Brun et al., GEANT3, Technical Report CERN-DD/EE/84-1, CERN, 1987.

[56] L.A.T. Brauerdick et al.. DESY-95-236, 1995.

[57] H. Abramowicz, A. Caldwell and R. Sinkus, Nucl. Inst. Meth. **A 365**, 508 (1995).

[58] N. Tuning, *ZUFOs : Hadronic Final State Reconstruction with Calorimeter, Tracking and Backsplash Correction*. ZEUS-Note-01-021, 2001.

[59] F. Jacquet and A. Blondel, *Proceedings of the Study for an ep Facility for Europe*, U. Amaldi (ed.), p. 391. Hamburg, Germany (1979). Also in preprint DESY 79/48.

[60] S. Bentvelsen, J. Engelen and P. Kooijman, *Proc. Workshop on Physics at HERA*, W. Buchmüller and G. Ingelman (eds.), Vol. 1, p. 23. Hamburg, Germany, DESY (1992);
K.C. Höger, ibid., p. 43.

[61] U. Bassler and G. Bernardi, Nucl. Inst. Meth. **A 361**, 197 (1995).

[62] ZEUS Coll., U. Holm (ed.), *The ZEUS Detector*. Status Report (unpublished), DESY (1993), available on `http://www-zeus.desy.de/bluebook/bluebook.html`.

[63] W.H. Smith, K. Tokushuku and L.W. Wiggers, *Proc. Computing in High-Energy Physics (CHEP), Annecy, France, Sept. 1992*, C. Verkerk and W. Wojcik (eds.), p. 222. CERN, Geneva, Switzerland (1992). Also in preprint DESY 92-150B.

[64] D. Bailey and R. Hall-Wilton, Nucl. Inst. Meth. **A 515**, 37 (2003).

[65] Particle Data Group, W.-M. Yao et al., J. Phys. **G 33**, 1 (2006).

[66] H. Jung, Comp. Phys. Comm. **86**, 147 (1995).

[67] G. Marchesini et al., Preprint Cavendish-HEP-99/17 (hep-ph/9912396), 1999; G. Marchesini et al., Comp. Phys. Comm. **67**, 465 (1992).

[68] A. Kwiatkowski, H. Spiesberger and H.-J. Möhring, Comp. Phys. Comm. **69**, 155 (1992). Also in *Proc. Workshop Physics at HERA*, 1991, DESY, Hamburg.

[69] CTEQ Coll., H.L. Lai et al., Eur. Phys. J. **C 12**, 375 (2000).

[70] M. Glück, E. Reya and A. Vogt, Phys. Rev. **D 46**, 1973 (1992).

[71] B. Andersson et al., Phys. Rep. **97**, 31 (1983).

[72] T. Sjöstrand, Comp. Phys. Comm. **82**, 74 (1994).

[73] B.R. Webber, Nucl. Phys. **B 238**, 492 (1984).

[74] ALEPH Coll., D. Buskulic et al., Phys. Lett. **B 388**, 648 (1996).

[75] OPAL Coll., K. Ackerstaff et al., Eur. Phys. J. **C 1**, 439 (1998).

[76] L. Gladilin, Preprint hep-ex/9912064, 1999.

[77] F. Cornet and C.A. García Canal, *Spin Dependence of Heavy Quark Fragmentation*. Preprint hep-ph/0702290, 2007.

[78] OPAL Coll., G. Alexander et al., Z. Phys. **C 72**, 1 (1996).

[79] Particle Data Group, S. Eidelman et al., Phys. Lett. **B 592**, 1 (2004).

[80] V.N. Gribov and L.N. Lipatov, Sov. J. Nucl. Phys. **15**, 438 (1972);
L.N. Lipatov, Sov. J. Nucl. Phys. **20**, 94 (1975);
G. Altarelli and G. Parisi, Nucl. Phys. **B 126**, 298 (1977);
Yu.L. Dokshitzer, Sov. Phys. JETP **46**, 641 (1977).

[81] P. Nason and C. Oleari, Nucl. Phys. **B 565**, 245 (2000).

[82] H1 Coll., C. Adloff et al., Eur. Phys. J. **C 25**, 41 (2002).

[83] ZEUS Coll., J. Breitweg et al., Eur. Phys. J. **C 6**, 603 (1999).

[84] S. Weinberg, *The Quantum Theory of Fields, vol. 1.* CUP, 1995.

Acknowledgements

I would like to thank the HEP group of the Universidad Autónoma de Madrid to give me the opportunity to join the ZEUS experiment. I am very grateful to Prof. Fernando Barreiro, Juan Terrón, José del Peso, Claudia Glasman, Enrico Tassi and Mara Soares for their continuous help and support. I sincerely thank to Prof. Luis Labarga, my supervisor, for his guidance, valuable advice, effort and dedication during all these years.

This work would not have been possible without the efforts of many people who were involved in the analysis. Many thanks to Roberval Walsh, Massimo Corradi, Leonid Gladilin, Matthew Wing, Richard Hall-Wilton, Achim Geiser, the coordinators of the Heavy Flavour group and members of the Editorial Board. Thanks to Prof. Fernando Cornet for useful discussions.

I want to express my gratitude to all my friends who made great these years in Hamburg. Thanks to Mónica Vazquez, Oscar González, Marcos Jiménez, Elías Ron, Ingo Bloch, Benjamin Kahle, Raquel Santamarta, Ana Yagües, Amita Raval, Didar Dobur, Damir Lelas, John Loizides and James Ferrando. Last, but not least, nothing of this would have been the same without Maria.